

**Numerical Analysis of the Heat Transfer  
Characteristics within an Evaporating Meniscus**

by

**Gregory Ball**

A thesis submitted to the Faculty of Graduate Studies and Research  
in partial fulfilment of the degree requirements of

**Master of Applied Science**

in

**Aerospace Engineering**

**Ottawa-Carleton Institute for Mechanical and Aerospace Engineering**

**Department of Mechanical and Aerospace Engineering**

**Carleton University**

**Ottawa, Ontario, Canada**

Copyright © 2012

**Gregory Ball**



Library and Archives  
Canada

Published Heritage  
Branch

395 Wellington Street  
Ottawa ON K1A 0N4  
Canada

Bibliothèque et  
Archives Canada

Direction du  
Patrimoine de l'édition

395, rue Wellington  
Ottawa ON K1A 0N4  
Canada

*Your file Votre référence*

*ISBN: 978-0-494-91578-3*

*Our file Notre référence*

*ISBN: 978-0-494-91578-3*

#### NOTICE:

The author has granted a non-exclusive license allowing Library and Archives Canada to reproduce, publish, archive, preserve, conserve, communicate to the public by telecommunication or on the Internet, loan, distribute and sell theses worldwide, for commercial or non-commercial purposes, in microform, paper, electronic and/or any other formats.

The author retains copyright ownership and moral rights in this thesis. Neither the thesis nor substantial extracts from it may be printed or otherwise reproduced without the author's permission.

#### AVIS:

L'auteur a accordé une licence non exclusive permettant à la Bibliothèque et Archives Canada de reproduire, publier, archiver, sauvegarder, conserver, transmettre au public par télécommunication ou par l'Internet, prêter, distribuer et vendre des thèses partout dans le monde, à des fins commerciales ou autres, sur support microforme, papier, électronique et/ou autres formats.

L'auteur conserve la propriété du droit d'auteur et des droits moraux qui protègent cette thèse. Ni la thèse ni des extraits substantiels de celle-ci ne doivent être imprimés ou autrement reproduits sans son autorisation.

---

In compliance with the Canadian Privacy Act some supporting forms may have been removed from this thesis.

While these forms may be included in the document page count, their removal does not represent any loss of content from the thesis.

Conformément à la loi canadienne sur la protection de la vie privée, quelques formulaires secondaires ont été enlevés de cette thèse.

Bien que ces formulaires aient inclus dans la pagination, il n'y aura aucun contenu manquant.

Canada

## **Abstract**

A numerical analysis was performed as to investigate the heat transfer characteristics of an evaporating thin-film meniscus. A mathematical model was used in the formulation of a third order ordinary differential equation. This equation governs the evaporating thin-film through use of continuity, momentum, energy equations and the Kelvin-Clapeyron model. This governing equation was treated as an initial value problem and was solved numerically using a Runge-Kutta technique.

The numerical model uses varying thermophysical properties and boundary conditions such as channel width, applied superheat, accommodation coefficient and working fluid which can be tailored by the user. This work focused mainly on the effects of altering accommodation coefficient and applied superheat. A unified solution is also presented which models the meniscus to half channel width.

The model was validated through comparison to literature values. In varying input values the following was determined; increasing superheat was found to shorten the film thickness and greatly increase the interfacial curvature overshoot values. The effect of decreasing accommodation coefficient lengthened the thin-film and retarded the evaporative effects.

*“Scientific knowledge is a body of statements of varying degrees of certainty --  
some most unsure, some nearly sure, none absolutely certain.”*

**-Richard Feynman**

## **Acknowledgements**

I would like to acknowledge my thesis supervisor, Dr. Tarik Kaya whose advice and encouragement was largely responsible for this research being undertaken and accomplished.

I would also like to thank John Polansky for his continued time and advice throughout the course of this research.

Finally, I would like to thank my family and fiancée for their continued support and patience throughout my educational journey.

# Table of Contents

List of Tables .....	ix
List of Figures .....	x
Nomenclature .....	xii
List of Appendices .....	xvi
Chapter 1 - Introduction.....	1
1.1 Research Motivation .....	1
1.2 Research Objectives .....	2
Chapter 2 – Conceptual and Literature Review .....	4
2.1 Conceptual Review .....	4
2.1.1 The Meniscus .....	4
2.1.2 The Bulk Region .....	5
2.1.3 The Thin-film Region .....	5
2.1.4 Adsorbed Region .....	6
2.2 Literature Review.....	7
2.2.1 Model Development.....	7
2.2.2 Young-Laplace Equation .....	8
2.2.3 Disjoining Pressure .....	9

2.2.4	Augmented Young-Laplace Equation.....	10
2.2.5	Evaporation Model and Accommodation Coefficient .....	10
2.2.6	Solution Methodologies .....	19
2.2.7	Equation Behaviour .....	21
2.2.8	Parameters Investigated and Observed Trends .....	22
Chapter 3 – Mathematical Model .....		25
3.1	Assumptions .....	26
3.2	Force Balance .....	27
3.3	Momentum (Navier-Stokes) Equations.....	28
3.3.1	Boundary Conditions .....	29
3.4	Continuity Equation .....	30
3.5	Energy Equation .....	30
3.5.1	Boundary Conditions .....	31
3.6	Liquid Pressure Gradient.....	32
3.7	Kelvin-Clapeyron Model.....	33
3.8	Interfacial Temperature Gradient .....	33
3.9	Complete Model.....	34
3.10	Initial Conditions .....	34
3.10.1	Adsorbed Thickness.....	34
3.10.2	Initial Condition Limits.....	35

3.10.3	Initial Condition Maximum .....	35
3.10.4	Initial Condition Minimum .....	36
Chapter 4 –	Numerical Model.....	37
4.1	Reduction of Order .....	38
4.2	Algorithm Outline .....	39
4.3	Required Inputs .....	43
4.4	Initial Conditions and Applied Perturbations.....	43
4.5	Model Evaluation of Various Terms.....	45
4.5.1	Adsorbed Thickness.....	45
4.5.2	Integral Term .....	46
4.6	Runge-Kutta Technique .....	47
4.6.1	Interfacial Temperature.....	49
4.6.2	Film Thickness.....	49
4.7	Constant Curvature.....	50
4.8	Far Field Curvature .....	51
4.9	Sources of Error .....	52
Chapter 5 –	Numerical Results .....	53
5.1	General Results .....	54
5.2	Effect of Accommodation Coefficient .....	72
5.3	Effect of Varying Applied Superheat.....	84

5.4 Unified Solution ..... 90

Chapter 6 - Conclusion and Recommendations ..... 96

6.1 Conclusions ..... 96

6.2 Recommendations ..... 98

References ..... 100

## List of Tables

Table 1: Comparison of studies on modelling an evaporating thin-film meniscus .....	22
Table 2: Coefficients for RK5 (4) 7M .....	48
Table 3: Numerical model input values – Wee comparison [8] .....	54
Table 4: Numerical model input values – Wang comparison [5] .....	67
Table 5: Numerical model input values – varying accommodation coefficient ( $\gamma$ ).....	73
Table 6: Numerical model input values – different superheats .....	84
Table 7: Numerical model input values – unified solution.....	92
Table 8: Variables used in ODE simplification .....	104

# List of Figures

Figure 1: Meniscus as it contacts a rigid & planar immiscible substrate.....	4
Figure 2: Nomenclature and geometry used in molecular flux derivation [adapted from 19].....	12
Figure 3: Modelling $S^*$ with regards to thin-film setup [adapted from 19].....	13
Figure 4: Molecular mechanisms of evaporation at a liquid-vapour interface [adapted from 26].....	17
Figure 5: Molecular mechanisms of condensation at a liquid-vapour interface [adapted from 26].....	18
Figure 6: Thin-film geometry used in mathematical model development.....	25
Figure 7: High level algorithm flow chart (adapted from [4]).....	40
Figure 8: Runge-Kutta algorithm flow chart (adopted from [4]).....	41
Figure 9: Maple algorithm flow chart.....	42
Figure 10: Thin-film thickness.....	55
Figure 11: Evaporative mass flux .....	57
Figure 12: Liquid pressure profile .....	59
Figure 13: Liquid pressure gradient.....	59
Figure 14: Disjoining pressure profile .....	61
Figure 15: Capillary pressure profile .....	62
Figure 16: Composite pressure profiles .....	63
Figure 17: Curvature profile .....	64
Figure 18: Interface temperature profile.....	65
Figure 19: Surface tension profile.....	66

Figure 20: Thin-film profiles at various superheats.....	68
Figure 21: Evaporative mass flux profile.....	69
Figure 22: Local composite pressure profiles.....	70
Figure 23: Thin-film thickness profiles.....	74
Figure 24: Evaporative mass flux profiles.....	75
Figure 25: Disjoining pressure profiles.....	76
Figure 26: Liquid pressure profiles.....	77
Figure 27: Capillary pressure profiles.....	78
Figure 28: Curvature profiles.....	79
Figure 29: Curvature gradients.....	80
Figure 30: Interfacial temperature profiles.....	81
Figure 31: Accommodation coefficient and the effect of the slope perturbation.....	82
Figure 32: Thin-film thickness profiles.....	85
Figure 33: Enlarged view of thin-film thickness profiles.....	86
Figure 34: Curvature profiles.....	87
Figure 35: Evaporative mass flux profiles.....	88
Figure 36: Schematic geometry of boundary conditions [adapted from 20].....	91
Figure 37: Unified thin-film thickness profile.....	93
Figure 38: Enlarged thin-film thickness profile.....	94
Figure 39: Thin-film thickness to channel radius - augmented Y-L solution vs Y-L solution.....	95

# Nomenclature

Symbol	Description	Units
$\bar{A}$	Area	[m <sup>2</sup> ]
$Bo$	Bond number	[-]
$C_{1-5}$	Integration constant (see Table 8)	[-]
$d$	Change of variable	[-]
$H$	Channel height	[m]
$h_v^{cl}$	Clapeyron evaporative mass flux coefficient	[kg/m <sup>2</sup> sK]
$i$	Step counter along thin-film	[nm]
$j_{nv+}$	Molecular flux in direction of bulk motion	[1/m <sup>2</sup> s]
$k_B$	Boltzmann constant	[J/m <sup>2</sup> sK]

$L$	Characteristic length	[m]
$m$	Mass of one molecule	[kg]
$m''$	Net mass flux	[kg/m <sup>2</sup> s]
$n$	Number of molecules	[-]
$\dot{q}$	Heat generation	[W/m <sup>3</sup> ]
$r$	Channel radius	[m]
$T$	Temperature	[K]
$u_s$	Thin-film slip (wall) velocity	[m/s]
$w_o$	Bulk velocity of vapour phase	[m/s]
$y$	Thin-film height (y-coordinate)	[m]

## Greek Characters

Symbol	Description	Units
$\beta$	Wall slip length	[m]
$\delta_o$	Adsorbed layer thickness	[m]
$\varepsilon_2$	Perturbation to $\delta'$	[-]
$\varepsilon_4$	Perturbation to $T_{lv_o}$	[K]
$\theta$	ODE simplification term (see Table 8)	[-]
$\lambda$	ODE simplification term (see Table 8)	[-]
$\nu$	Kinematic viscosity	[m <sup>2</sup> /s]
$\sigma$	Interfacial (surface) tension	[N/m]
$\chi$	ODE simplification term (see Table 8)	[-]
$\omega$	ODE simplification term (see Table 8)	[-]

## Subscripts

Symbol	Description	Units
<i>d</i>	Disjoining	[-]
<i>le</i>	Liquid-Evaporating	[-]
<i>o</i>	Initial	[-]
<i>vc</i>	Vapour-Condensing	[-]
<i>guess</i>	Guess value used in Runge-Kutta solver	[-]

## Superscripts

Symbol	Description	Units

## List of Appendices

Appendix A – Thin-film Model.....	104
Appendix B – Adsorbed Film Thickness.....	116
Appendix C – Bond Number Calculation.....	117

# **Chapter 1**

## **Introduction**

Thin-film heat transfer research is a continuously evolving field within the engineering and science communities. Considering the size scale of the analysis, it ventures into the cross-over between continuum mechanics and molecular dynamics. As such, various solution methodologies exist. This research is intended to further extend upon existing mathematical models and provide further insight into the heat transfer characteristics within an evaporating thin-film meniscus.

### **1.1 Research Motivation**

High performance phase-change heat transfer devices such as heat pipes, grooved evaporators and vapour chambers are essential in many industrial and research initiatives [1,2]. From spacecraft thermal management to the cooling of a personal computer, these heat transfer devices play a significant role and a better understanding of their intricacies is needed to accommodate the presence of very high heat fluxes.

Wayner [1] has studied the mechanism whereby the leading edge of an evaporating thin-film meniscus can stay in contact with the substrate (see Figure 1). This phenomenon is of interest to many high performance heat transfer processes such as the ones mentioned above, as these devices use wicking structures to supply an evaporator with fluid, which allows for the existence of evaporating thin-film regions [1,3]. His works have laid the

foundation for the current solutions being developed in numerically modelling this interfacial phenomenon. Several numerical solutions have been proposed, most of which follow the same qualitative trends [4].

A numerical analysis is used to solve a 3<sup>rd</sup> order Ordinary Differential Equation (ODE) which governs the thin-film region. Results are compiled and compared using various input parameters, such as altering the applied super heat values, varying the channel width and altering the accommodation coefficient.

The alteration and corresponding effect of accommodation coefficient is something that has yet to be published in the literature and is given special attention; it directly pertains to the Kelvin - Clapeyron model, an essential component in developing the differential equation.

## **1.2 Research Objectives**

The objective of this research is to improve upon the already existing numerical solution provided by Polansky [4] in a previous M.A.Sc thesis by the following measures:

- Providing more robust solutions for various input parameters, including a greater range of applied superheat and larger channel widths indicative of current experimental works.
- Quantitatively verifying trends published in literature, namely confirming that the numerical model can reproduce results given appropriate boundary and initial conditions for both 3<sup>rd</sup> and 4<sup>th</sup> order models found in literature.

- Bridging gaps found in literature, mainly providing an in depth analysis of the effect of accommodation coefficient on the thin-film model and providing transparency of perturbations used in solutions.
- Modelling a unified solution to half channel width, combining the augmented Young-Laplace model appropriately with the Young-Laplace model.

In accurately modelling a thin-film meniscus, values such as characteristic length and height can also be extracted. This is in an effort to provide further insight into instability theory of a thin-film meniscus, which is currently being analysed at Carleton. The model developed in this study is being incorporated into a thin-film instability model by another graduate student.

# Chapter 2

## Conceptual and Literature Review

### 2.1 Conceptual Review

A few key concepts must first be touched upon before the literature review can be performed. The following touches on basic concepts of the meniscus characteristics to be studied.

#### 2.1.1 The Meniscus

Figure 1 provides the general set-up of the thin-film problem, while also introducing the three portions of a meniscus.

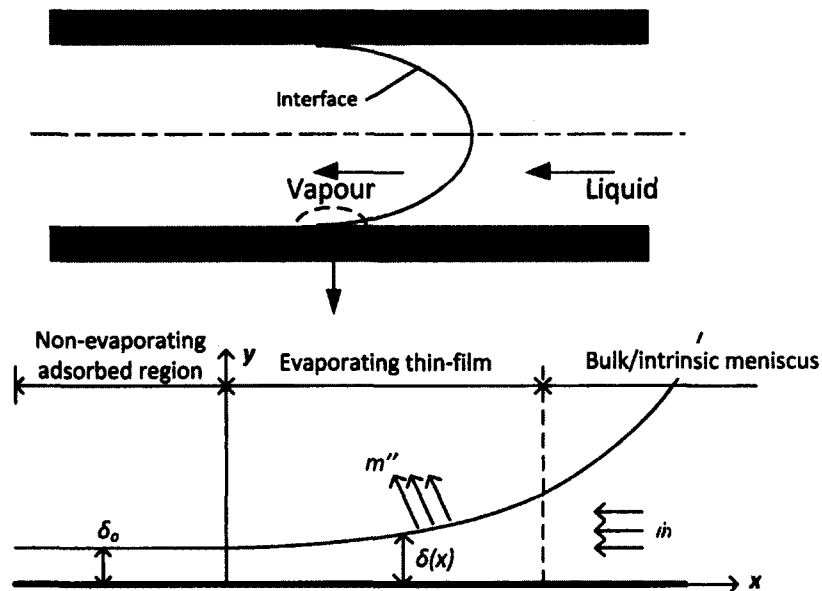


Figure 1: Meniscus as it contacts a rigid & planar immiscible substrate

The three portions of the meniscus are the bulk (sometimes referred to as intrinsic) meniscus, the evaporating thin-film and the adsorbed region. For the purpose of this research, we will consider the meniscus to be formed between the close proximity of two walls, as seen in Figure 1.

### **2.1.2 The Bulk Region**

The bulk region is the most familiar part of the meniscus, and can be seen with the naked eye, whether it is observed in a graduated cylinder or a bucket of water. In the aforementioned examples, it is likely a concave meniscus is pictured. The concavity of a meniscus is determined by the cohesive interaction of the liquid with the substrate [4]. In a concave meniscus, the liquid molecules have a greater affinity for the solid substrate than the bulk liquid. This phenomenon is known as wetting. For the purpose of this research, the analyses of only concave menisci are performed.

Characteristics of the bulk region are generally well understood. The evaporative mass flux contribution is small when compared to that of the thin-film region. This has been noted in several works [5-7]. The capillary pressure is dominant, with a negligible contribution of disjoining pressure [5,8,9]. It is for this reason that the bulk region is governed by the Young-Laplace equation and has a constant curvature of  $1/r$  [10]. This constant curvature is often used as a far-field boundary condition when determining the transition from the thin-film region to the bulk meniscus [10].

### **2.1.3 The Thin-film Region**

The evaporating thin-film region is of primary concern as it is the focus of this research. Within the thin-film region the effect of capillarity and disjoining pressure are equally

important [8]. Numerous investigations [5,11-13] indicate that it is within this region that high heat transfer rates occur as a result of small conductive resistance and fluid flow driven by the capillary and disjoining pressure gradients.

The boundaries of the thin-film region are also of particular interest. As mentioned in the bulk meniscus section, a condition of constant curvature is imposed when identifying the termination of the thin-film region. Defining the beginning of the thin-film region can also be done with confidence, as it transitions to the adsorbed region when curvature is zero [5,8].

Near the adsorbed region, the disjoining pressure is dominant. Transitioning towards the bulk region, there is a changeover of dominance as disjoining pressure diminishes and capillary pressure is more prominent [9,14]. This transition is attributed to an increasing thin-film thickness  $\delta(x)$  (See Figure 1). It is this increasing film thickness that allows sufficient evaporation, resulting from the decay of disjoining pressure [4], and solving the resulting interface profile is a primary goal of this research.

#### **2.1.4 Adsorbed Region**

The adsorbed region is on the nanometer scale, and is governed by several key attributes. Considering the size scale of this region, it is mainly characterized by the dominance of van der Waals forces between the liquid and rigid & planar substrate [8]. Derjaguin et al. [15] was one of the first to recognize this phenomenon and his works led to the characterization and application of disjoining pressure. This leads to the inability of the superheated liquid molecules to evaporate within the adsorbed region, as they are restrained by these overwhelming adhesive forces [8,10]. It is these adhesive forces that

prevent evaporation that allow the region to be considered uniform thickness  $\delta_0$  (see Figure 1) and of unspecified length [1,2,10,14,16]. This thickness however, as mentioned below is temperature dependent. It is thus inferred that the imposed curvature value within the adsorbed region is zero.

The thickness of the adsorbed region is sometimes given a constant value estimated from the size scale of the problem. Park et al. [9,17] implemented this technique. However, it is now known that minor changes to the adsorbed film thickness can result in large changes in thin-film flow and evaporation rate [18]. Wayner [6] demonstrates that the adsorbed film thickness changes with respect to temperature and concludes that using a constant value will greatly underestimate the total heat transport through the thin-film.

A final assumption is applicable within the adsorbed layer. Given the size scale of this region, it is assumed the fluid temperature is equal to that of the substrate [5,8,16].

## **2.2 Literature Review**

Published works today generally follow the same model development when creating a numerical solution. The key concepts are discussed below, including an in-depth analysis on accommodation coefficient, a coefficient in which particular interest is given to in this work.

### **2.2.1 Model Development**

Within thin-film theory, the literature has more or less converged to an overall model used in analysing an evaporating thin-film. The main goal of modelling an evaporating thin-film meniscus is to quantify characteristics of the film such as size and heat transport ability. Slight deviations are made to include and capture increasing detail in attempts

to refine current models. The models can vary from 3<sup>rd</sup> to 4<sup>th</sup> order ODEs, however numerical analysis is nearly identical for both. Regardless of order, several key concepts are utilized in building the model and will be discussed below.

## 2.2.2 Young-Laplace Equation

The Young-Laplace equation comes about when performing a thermodynamic analysis of interfacial tension effects. The equation can be derived from the consideration of two fluids (I and II) in equilibrium separated by a planar (fixed shape) interface region.

If this fixed shape restriction is relaxed and deformation of the interface is allowed, both the area and curvature of the interface can change. The pressure difference across the interface can be represented most generally as:

$$P_I - P_{II} = \sigma \frac{dA_I}{dV_I} \quad (1)$$

Equation 1 can further simplify for a curved interface as:

$$P_I - P_{II} = \sigma \left( \frac{1}{r_1} + \frac{1}{r_2} \right) \quad (2)$$

Equation 2 is referred to as the Young-Laplace equation and relates the pressure difference across the interface to the interfacial tension and the geometry of the interface at equilibrium [19]. It is noted that this above equation is applicable for the interface between two fluid phases of a pure substance, such is analysed in this research.

Now considering Equation 2 for the geometry of a channel used in this research, the second of the principal radii tends to infinity thus only leaving the first principal radius,

which is in essence the curvature of the bulk meniscus ( $\frac{1}{r_1}$ ). This leaves the following term, which is ultimately used to represent capillary pressure:

$$P_l - P_{II} = \Delta P = P_c = \sigma\kappa \quad (3)$$

### 2.2.3 Disjoining Pressure

Disjoining pressure which was mentioned and briefly discussed in the adsorbed region section above, plays an integral role in the development of the augmented Young-Laplace equation used in thin-film analysis.

Derjaguin [15] first conceptualized disjoining pressure as a means of explaining solid-liquid thin-film interactions. For non-polar liquids (such is the case of analysis in this research), the primary cause of disjoining pressure is London dispersion forces resulting from the interaction of the positive nucleus of one molecule with the electrons of another molecule [8]. This is the weakest of the van der Waals forces but nevertheless given the size scale of our analysis play a significant role in modelling an evaporating thin-film.

Disjoining pressure for non-polar liquids is described using the following relationship:

$$P_d = \frac{A}{\delta^3} \quad (4)$$

Where  $A$  is the dispersion constant and  $6\pi A$  is the Hamaker constant [20]. Often in literature a distinguishable difference is failed to be made between dispersion and Hamaker constant. It is integral to use the correct value as the governing equation is so highly non-linear a factor of  $6\pi$  can make a significant difference. The  $\delta$  represents film

thickness. From this it is clear to see that as film thickness increases, the disjoining pressure declines as it is third power dependent on film thickness.

#### **2.2.4 Augmented Young-Laplace Equation**

The augmented Young-Laplace equation, much like the Young-Laplace equation is used to analyse the thermodynamic effects of the interfacial tension across the thin-film interface. In performing this analysis, disjoining pressure, capillary pressure, liquid pressure and vapour pressure must all be accounted for. It is the augmented Young-Laplace equation that provides the means for a continuum analysis of an evaporating thin-film meniscus. Wayner et al. [21] first used the augmented Young-Laplace equation in analysis. The equation is presented below:

$$P_v - P_l = P_c + P_d \quad (5)$$

Equation 5 is representative of the force balance present in the system. Using Equation 5 and the evaporation model which is discussed in the proceeding section, one can determine the thin-film profile and heat transfer characteristics.

#### **2.2.5 Evaporation Model and Accommodation Coefficient**

The motivation behind an evaporation model is to accurately determine the local evaporative mass flux associated with interfacial temperature and pressure jump that occurs across a liquid-vapour interface. Built into this model is an accommodation coefficient, which attempts to quantify the molecular behaviour at an interface. The effects of altering the value for accommodation coefficient are not fully understood.

In order to first appreciate how the accommodation coefficient has an effect on the characteristics of an evaporating thin-film, it is important to recognize where the variable first appears. Accommodation coefficient appears when analysing the molecular transport at the liquid-vapour interface.

The analysis begins by observing the liquid-vapour interface at the molecular level. Because the motion of molecules at the liquid-vapour interface plays an essential role in determining heat and mass flux during vaporization, relevant aspects of kinetic theory of gases must first be analysed [19].

Beginning with Maxwell's velocity distribution from kinetic theory of gases:

$$\frac{dn_{uvw}}{n} = \left( \frac{m}{2\pi k_B T} \right)^{3/2} \exp \left( - \left( \frac{m}{2k_B T} \right) (u^2 + v^2 + w^2) \right) dudvdw \quad (6)$$

Now, obtaining a relationship for the fraction of the molecules with speeds in a specified range, regardless of direction we have [19]:

$$\frac{dn_c}{n} = 4\pi \left( \frac{m}{2\pi k_B T} \right)^{3/2} c^2 \exp \left( \frac{-mc^2}{2k_B T} \right) dc \quad (7)$$

From Equation 7 and using the following geometry:

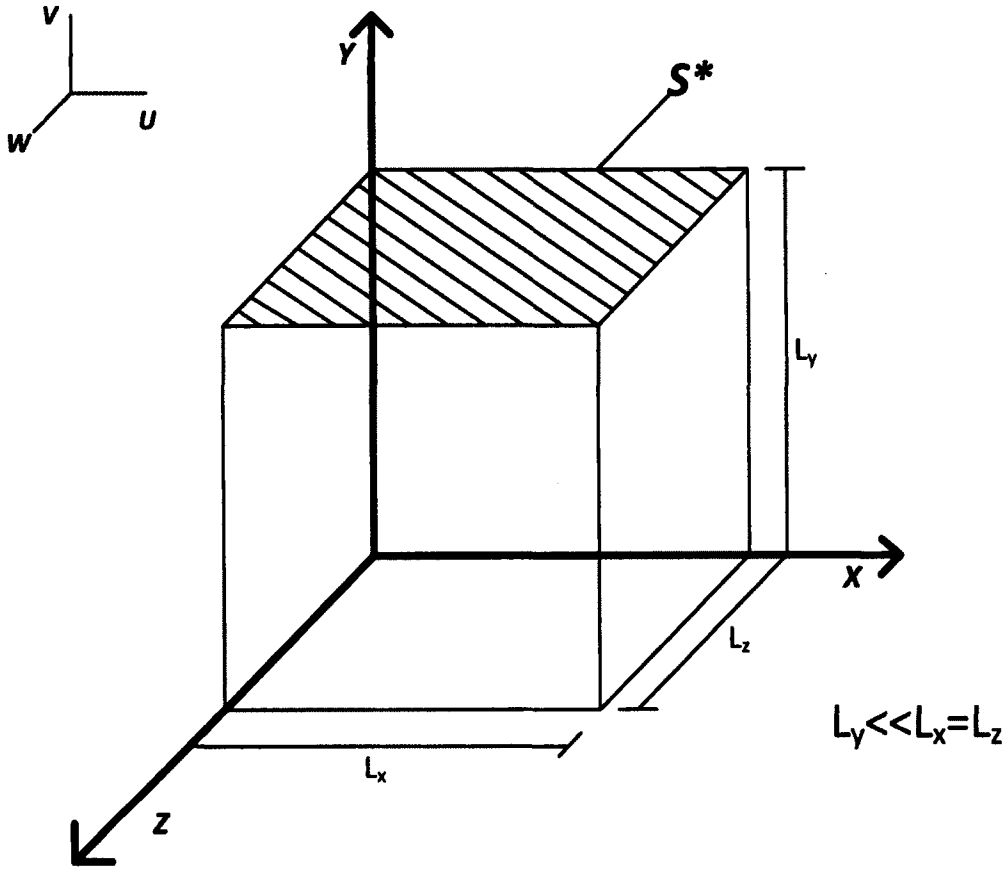


Figure 2: Nomenclature and geometry used in molecular flux derivation [adapted from 19]

The flux of molecules passing through  $S^*$  can be determined. Considering all molecules with a  $y$ -component velocity ( $v$ ) and any  $u$  and  $w$ , integrating over all possible values of  $u$  and  $w$  obtains the following relation:

$$\frac{dn_v}{n} = \int \int \frac{dn_{uvw}}{n} \quad (8)$$

$$\frac{dn_v}{n} = \left( \frac{m}{2\pi k_B T} \right)^{1/2} \exp\left( \frac{-mv^2}{2k_B T} \right) dv \quad (9)$$

With Equation 9, a molecule with a  $v$  direction velocity and any  $w$  and/or  $u$  component must lie within a distance  $v\Delta t$  from  $S^*$ . Allowing the total number of molecules within

the control volume to be represented by  $n$ , the flux of molecules with velocity  $v$  in the  $y$  direction that will pass through  $S^*$  is equal to:

$$dj_v = \left( \frac{v\Delta t}{L_y} \right) dn_v \left( \frac{1}{L_x L_z} \right) \left( \frac{1}{\Delta t} \right) \quad (10)$$

Now, substituting Equation 9 into Equation 10 and integrating over all  $v$  we obtain:

$$j_n = \left( \frac{1}{4} \right) \left( \frac{n}{v} \right) \left( \frac{8k_B T}{\pi m} \right) = \left( \frac{M}{2\pi R} \right)^{1/2} \frac{P}{mT^{1/2}} \quad (11)$$

Now Equation 11 can be applied across the liquid-vapour interface of the thin-film meniscus giving further insight into the molecular motion.

Considering the case of evaporation, and placing  $S^*$  at an infinitesimal distance outside of the liquid interface (in the vapour phase) such as modelled in Figure 3.

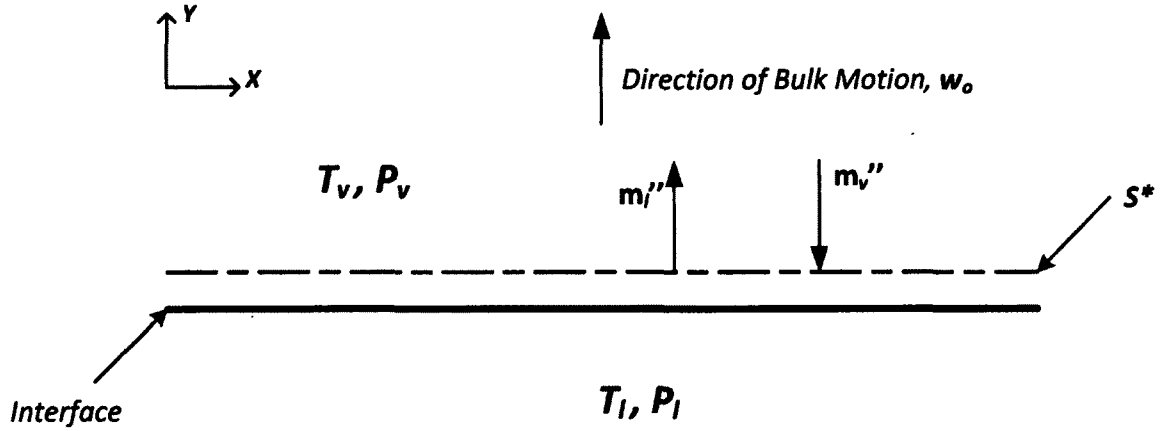


Figure 3: Modelling  $S^*$  with regards to thin-film setup [adapted from 19]

From Figure 3, an equation representing the net mass flux can be generated:

$$m_{net}'' = m_l'' - m_v'' \quad (12)$$

Now for the case of evaporation, the vapour must have a bulk velocity  $w_o$ . Schrage [22] developed a relationship in which he defines the molecular flux for the vapour field whilst incorporating the effect of the bulk velocity:

$$j_{nv+} = \Gamma(s) \left( \frac{M}{2\pi RT} \right)^{1/2} \frac{P}{m} \quad (13)$$

$$j_{nv-} = \Gamma(-s) \left( \frac{M}{2\pi RT} \right)^{1/2} \frac{P}{m} \quad (14)$$

Where  $s$  is a dimensionless parameter and is represented as:

$$s = \frac{w_o}{(2RT/M)^{1/2}} \quad (15)$$

And the function  $\Gamma(s)$  represented as:

$$\Gamma(s) = \exp(s^2) + s\pi^{1/2} (1 + \text{erf}(s)) \quad (16)$$

$$\Gamma(-s) = \exp(s^2) - s\pi^{1/2} (1 - \text{erf}(s)) \quad (17)$$

Equations 16 and 17 represent the molecular flux with a bulk velocity in the positive and negative  $y$  direction respectively. As seen below in Equation 18, in the case of vapourization, Equation 13 is utilized. It is in this context where accommodation coefficient ( $\gamma$ ) is first introduced, and will be discussed shortly.

$$m_{vc}^* = \begin{cases} m\gamma_c j_{nv+} & \rightarrow \text{vapourization} \\ m\gamma_c j_{nv-} & \rightarrow \text{condensation} \end{cases} \quad (18)$$

Equation 13 represents the evaporative mass flux in the vapour field. In essence, considering the vaporization case, the equation represents the fraction of molecules with a positive y-component velocity that are indeed evaporating.

Similarly, within the liquid phase, an equation representing the fraction of molecules that successfully leave the liquid phase and are released into the vapour phase is generated:

$$m_{ie}'' = m\gamma_e j_n \quad (19)$$

Now, the new net mass flux equation across the interface is written as:

$$m_i'' = m_{ie}'' - m_{vc}'' \quad (20)$$

Substituting Equations 18 and 19 into 20, the following equation is obtained:

$$m_i'' = \left( \frac{M}{2\pi R} \right)^{1/2} \left( \frac{\gamma_e P_l}{T_l^{1/2}} - \frac{\Gamma(s)\gamma_c P_v}{T_v^{1/2}} \right) \quad (21)$$

Equation 21 provides the foundation for the Kelvin-Clapeyron model used in the solution of the thin-film meniscus, and provides a reasonable means of quantifying the pressure and temperature jump at the liquid-vapour interface. The Kelvin-Clapeyron model, developed by Wayner [6] is a linearized version of Equation 21 and appears as follows:

$$\dot{m}_{evap}'' = \frac{1}{h_{fg}} \left( h_{lv}^{cl} (T_{lv} - T_v) - h_{lv}^{kl} (P_d + P_c) \right) \quad (22)$$

Given,

$$h_{lv}^{cl} = \eta \left( \frac{1}{T_{lv}} \right)^{3/2} \left( \frac{M h_{fg}}{T_v} \right) \quad (23)$$

$$h_{iv}^{kl} = \eta \left( \frac{1}{T_{iv}} \right)^{3/2} V_i \quad (24)$$

and

$$\eta = \left( \frac{\left( \frac{2\gamma}{2-\gamma} \right)^2 M}{2\pi R} \right)^{1/2} \left( \frac{P_v h_{fg}}{R} \right) \quad (25)$$

This interfacial evaporative mass flux model has been used extensively in predicting the evaporation and condensation profiles along an interface [1,5,6,8,9,11,14,16,20,21,23-25].

Continuing now with the discussion of accommodation coefficient ( $\gamma$ ), in Equation 21 there exists both  $\gamma_e$  and  $\gamma_c$  which represent evaporation and condensation coefficient respectively. Both of these coefficients will be individually defined:

Marek and Straub [26] state the evaporation coefficient as originally defined by Knudsen as:

$$\gamma_e = \frac{\text{\# of molecules transferred to the vapour phase}}{\text{\# of molecules emitted from the liquid phase}} \quad (26)$$

This can be visualized as follows:

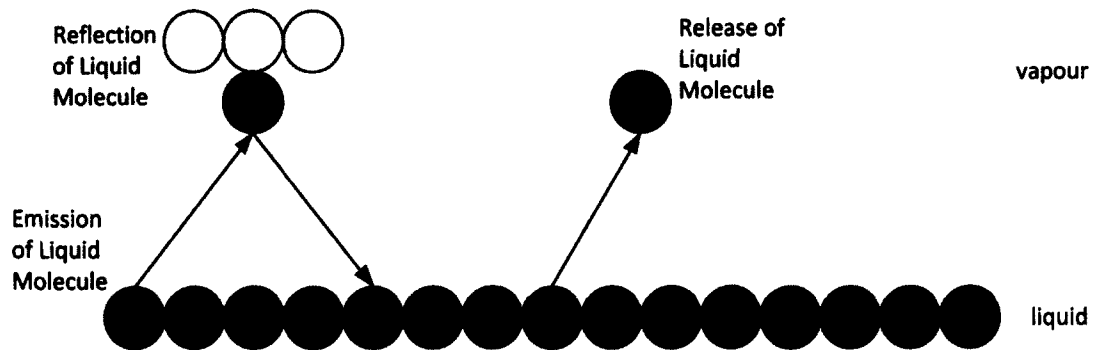


**Figure 4: Molecular mechanisms of evaporation at a liquid-vapour interface [adapted from 26]**

Considering Figure 4 it is clear that an evaporation coefficient less than unity implies incomplete evaporation as not all of the molecules emitted from the liquid phase are released. A value of unity would imply perfect evaporation [26].

Marek and Straub [26] state condensation coefficient as defined by Prüger as:

$$\gamma_c = \frac{\text{\# of molecules absorbed by the liquid phase}}{\text{\# of molecules impinging on the liquid phase}} \quad (27)$$

This is best visualized as:

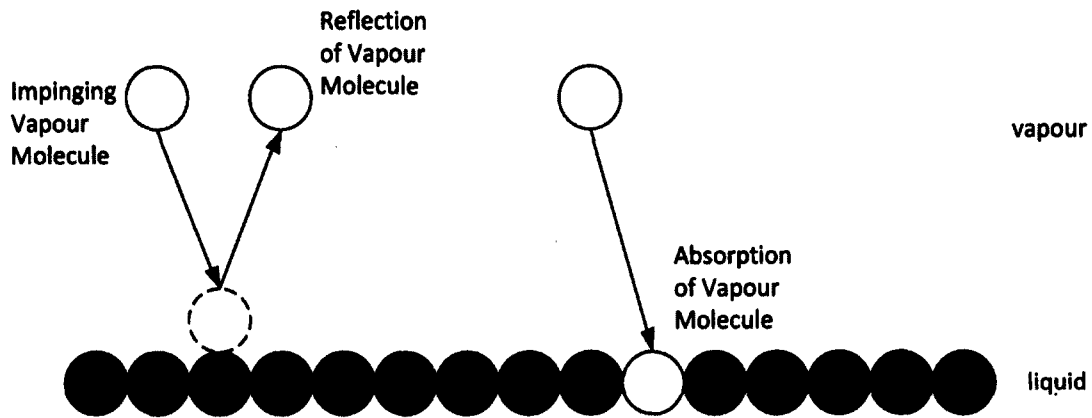


**Figure 5: Molecular mechanisms of condensation at a liquid-vapour interface [adapted from 26]**

Much like the case of evaporation, a condensation coefficient less than one represents incomplete condensation, with a value of one representing full condensation [26].

With an understanding of both these coefficients one can see their importance within Equations 18-21. Now, such is common practice within thin-film research to equate  $\gamma_e = \gamma_c = \gamma$ . It is important to realise that this does not imply no net mass flux and thus equilibrium. The only case where equating these coefficients implies equilibrium is when the denominator of Equations 26 and 27 are equal, which also suggests that there would be no bulk velocity in the vapour field ( $w_o=0$ ). If this is the case, Schrage [19,22] shows that the function  $I(s)$  tends to unity, the pressure and temperature jump across the interface would not exist and as a result Equation 21 would yield a result of zero evaporative mass flux.

In the case where  $\gamma_e = \gamma_c = \gamma$  and the denominators of the respective terms do not equate, there would still be a net mass flux at the interface, and this is the case which is discussed in the results section. This assumption is generally accepted in the absence of the knowledge of the individual accommodation coefficients, however as Carey [22] states, this assumption is suspect.

Furthermore, little experimental work has been done in quantifying accommodation coefficients given the molecular nature of the problem. Mills [27] notes that in cases of extreme fluid purity, accommodation coefficient should tend to unity.

### **2.2.6 Solution Methodologies**

Several publications have provided solutions in modelling an evaporating thin-film meniscus. Within these solutions, many commonalities exist and refinements are consistently being made in eliminating assumptions and creating more robust models. In general there are three methods of solution. They are as follows:

- Continuum mechanics – employ use of continuity, momentum, energy and an evaporation model. This allows for an ODE to be solved numerically, most frequently using Runge-Kutta.
- Molecular dynamics simulation
- Computational Fluid Dynamics (CFD)
- Finite Element Method – Iterative solution coupled with experimental data.

Of the above methods, the continuum mechanics/Runge-Kutta approach is mostly seen in literature as can be observed in [2,5,8-10,14,17,20,21]. This method of solution generates a 3<sup>rd</sup> or 4<sup>th</sup> order ODE, which is solved as an initial value problem. This requires initial value inputs for all derivatives. As mentioned when describing the adsorbed region, the thickness is constant and thus has a slope and higher order derivatives of zero. These cannot be used as initial conditions as it produces a trivial solution. As a result, perturbations are applied to the initial conditions.

Maroo et al. [28] provides a nanoscale model of an evaporating thin-film, which is solved with a molecular dynamics simulation. Maroo studies with this simulation the heat and mass transfer characteristics in the thin-film region by modelling the atomic interaction between the liquid and vapour phase.

Ranjan et al. [29,30] provides a transient, three-dimensional model for the thermal transport in heat pipes, in particular the effect of different wick structures. Considering the three-dimensional nature of this analysis, more detail is observed and insight into Marangoni vortices, convection effects and temperature distribution is discussed.

Panchangam et al. [23] uses a finite element method coupled with high resolution experimental liquid profile data to obtain a two-dimensional heat conduction profile in the solid substrate wall and the solid-liquid interfacial temperature profile in the evaporating thin-film region. A continuum model as discussed above is then joined with this data for developing a complete evaporating thin-film profile.

### 2.2.7 Equation Behaviour

As mentioned, numerical solutions to the 3<sup>rd</sup> or 4<sup>th</sup> order ODE used in modelling an evaporating thin-film require a set of perturbed initial conditions. The ODE however is highly non-linear, making it difficult to pinpoint a set of perturbations that allow for a meaningful solution. Most published works will not include their applied perturbations. Du et al. [20] states that the thickness perturbation  $\epsilon_1$  should be set sufficiently close to zero. Du goes on to state the slope perturbation  $\epsilon_2$  should be set slightly larger than zero. It is these types of ambiguities that make it difficult to find a set of applied perturbations that work. Furthermore, altering any parameters that in turn alter boundary conditions can have a profound effect on the perturbations. Dasgupta et al. [11] notes that the governing equation is extremely sensitive to boundary conditions.

Of note is the lack of relationship between the derivative perturbations and the level of applied superheat or varying channel width [4,5,14,17]. These are not the only parameters that have an effect on applied perturbation. This research looks at the effect altering the accommodation coefficient has on the slope perturbation  $\epsilon_2$ .

As mentioned above, the governing equation is found to be either a 3<sup>rd</sup> or 4<sup>th</sup> order ODE. This discrepancy is well described in literature, and is at the discretion of the author in determining which model they feel is appropriate. The 4<sup>th</sup> order equations are built off of the 3<sup>rd</sup> order equations, with the application of one more differentiation with regards to the length of the thin-film. This additional differentiation is done as to remove the integration term associated with the liquid pressure gradient and evaporative mass flux [5,8,14]. However, with the ability to solve this integral numerically, the need for the 4<sup>th</sup> order is unnecessary.

When a 3<sup>rd</sup> order equation is used, Wee et al. [8] notes the solution is very sensitive to the specification of the initial condition for the first derivative of thickness, especially with increasing superheat. When dealing with the 4<sup>th</sup> order equation, Wang et al. [5,14] notes this sensitivity dependence is mainly dealing with the second derivative perturbation.

### 2.2.8 Parameters Investigated and Observed Trends

As alluded to above, many parameters can be altered within the model, and an investigation as to the effect on thin-film characteristics can be done. Table 1 provides a summary of common variations undertaken by various authors.

**Table 1: Comparison of studies on modelling an evaporating thin-film meniscus**

Authors	Non-isothermal Interfacial Condition	Varying Thermophysical Properties	Slip Boundary Condition	Polarity Effect	Superheat Effect (at least 5K range)
Wayner et al. [21]	✓	-	-	-	-
Hallinan et al.[41]	✓	-	-	-	-
Qu and Ma. [16]	✓	-	-	✓	-
Wee et al. [8]	✓	✓	✓	✓	-
Ball, Present Study	✓	✓	✓*	-	✓

\*Not included in current thesis, but studied previously by Polansky [4]

Of these above listed parameters the following general trends were observed:

Potash and Wayner [31] were the first to show that both pressure gradient and evaporative mass flux reach a maximum within the thin-film region. It was Moosman and Homsy [32] that implemented a mathematical model to describe the thin-film characteristics using perturbation analysis. The effect of including an interfacial temperature gradient term, as well as varying thermophysical properties allows for much more pronounced effects to be seen when superheat is varied [2]. An increased superheat lessens the adsorbed film thickness, and creates a much more aggressive curvature increase as the film transitions from adsorbed region to the thin-film region. In general, the length is decreased, but the height is increased at higher superheats, creating a much 'steeper' thin-film profile [2]. When polar effects are considered on the disjoining pressure model, the thin-film length is extended, all the while reducing the evaporative heat transfer fluxes [8]. The slip boundary condition elongates the thin-film while yielding a lower pressure gradient [4,8].

In addition to the above trends, variance in channel width has also been observed, such as in [16]. The effect of an increasing channel width was an increased thin-film length [16]. Du et al. [33] attempts to quantify the effects of using altered evaporation models. He concludes that neglecting disjoining terms have less of an effect than neglecting capillary terms. It is also concluded that the substrate thickness does have a minor effect on the total heat transfer.

Additional effects are also starting to be considered in recent works. Kou and Bai [34] relate wall slip to a temperature jump at the solid liquid interface. They conclude that the

presence of a temperature jump at the interface can reduce heat and mass transport characteristics.

# Chapter 3

## Mathematical Model

The following will detail the development of the 3<sup>rd</sup> order ODE used in this research. Figure 6 provides the mathematical setup used in analysis of the evaporating thin-film meniscus. The origin of the Cartesian coordinate system used is placed at the boundary point signifying the end of the adsorbed region and beginning of the evaporating thin-film. The y-coordinate describes film thickness, x-coordinate film length and z-coordinate film depth.

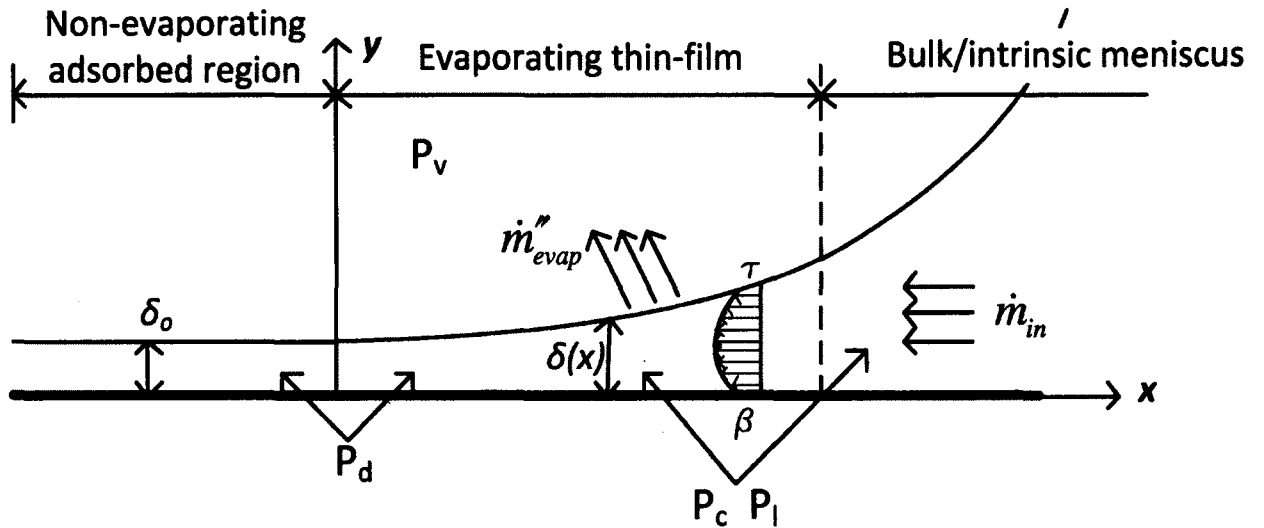


Figure 6: Thin-film geometry used in mathematical model development

### **3.1 Assumptions**

In modelling the evaporating thin-film the following simplifying assumptions are made:

- 1) Both fluid phases (liquid and vapour) are of the same pure substance that is immiscible with the rigid & planar substrate.
- 2) Fluid flow is x-directional, with no flow in the y or z directions.
- 3) The evaporative flow from the thin-film is sustained by constant liquid inflow from the bulk meniscus controlled by gradients in capillary and disjoining pressure.
- 4) The liquid temperature at the interface,  $T_{lv}$ , is non-uniform and not equal to the bulk vapour temperature.
- 5) Gravitational forces are neglected (As Bond number is sufficiently small – See Appendix C for details).
- 6) The rigid & planar substrate is smooth and the liquid wets the substrate completely.
- 7) The vapour pressure is uniform and constant.
- 8) The vapour field is of constant temperature.
- 9) During evaporation the system is operating at steady-state.
- 10) Meniscus depth is assumed to be unity.
- 11) Convection effects are negligible in both liquid and vapour fields.
- 12) Radiative terms are negligible.
- 13) No evaporation within the adsorbed region.

## 3.2 Force Balance

Utilizing the augmented Young-Laplace equation developed by Wayner et al.[21] we have:

$$P_v - P_l = P_c + P_d \quad (28)$$

Where,

$$P_d = \frac{A}{\delta^3} \quad (29)$$

$$P_c = \sigma \kappa \quad (30)$$

$$P_v = \text{constant} \quad (31)$$

With the local curvature is defined as:

$$\kappa = \frac{\delta''}{(1 + (\delta')^2)^{3/2}} \quad (32)$$

And local interfacial tension as:

$$\sigma = a + bT_v \quad (33)$$

Substituting Equations 29-33 into Equation 28, and differentiating w.r.t. film length such

as to create an equation for  $\frac{dP_l}{dx}$ , one can arrive at Equation 34:

$$\frac{dP_l}{dx} = - \left( \sigma' \left( \frac{\delta''}{\alpha^{3/2}} \right) + \sigma \left( \frac{\delta'''}{\alpha^{3/2}} - \frac{3(\delta'')^2 \delta'}{\alpha^{5/2}} \right) - \frac{3A}{\delta^4} \delta' \right) \quad (34)$$

Where  $\alpha$  is:

$$\alpha = (1 + (\delta')^2) \quad (35)$$

Now, isolating Equation 34 for  $\delta'''$  we have:

$$\delta''' = \frac{\alpha^{3/2}}{\sigma} \left( -\frac{dP_l}{dx} + \frac{3A}{\delta^4} \delta' \right) - \frac{b}{\sigma} \left( \frac{dT_{lv}}{dx} \right) \delta' + \frac{3(\delta'')^2 \delta'}{\alpha} \quad (36)$$

Equation 36 provides the foundation for the analysis of an evaporating thin-film meniscus. From continuity, momentum, energy and the Kelvin-Clapeyron model further relationships can be developed for the liquid pressure gradient and interfacial temperature gradient  $\frac{dP_l}{dx}$  and  $\frac{dT_{lv}}{dx}$  respectively.

### 3.3 Momentum (Navier-Stokes) Equations

From the use of Navier-Stokes equations, and applying appropriate simplifying assumptions, a relationship for the liquid pressure gradient can be developed.

Considering assumption two, the flow is restricted to the x-direction. This simplifies the three principal equations of Navier-Stokes to only the x-direction momentum equation:

$$\rho \left( \frac{du}{dt} + u \frac{du}{dx} + v \frac{du}{dy} + w \frac{du}{dz} \right) = -\frac{dP_l}{dx} + \mu \left( \frac{d^2u}{dx^2} + \frac{d^2u}{dy^2} + \frac{d^2u}{dz^2} \right) + \rho g_x \quad (37)$$

Considering the geometry of the problem, that is the thin-film height is much less than the length, it is appropriate to apply lubrication approximation [8,35] to Equation 37, allowing the equation to reduce to:

$$\frac{dP_l}{dx} = \mu \frac{d^2u}{dy^2} \quad (38)$$

### 3.3.1 Boundary Conditions

Using Equation 38 with appropriate boundary conditions, an equation for the velocity profile can be generated.

These boundary conditions are as follows:

At the solid-liquid interface ( $y=0$ ) slip is permitted. This is represented as:

$$u = u_s = -\beta \frac{du}{dy} \quad (39)$$

At the liquid-vapour interface ( $y=\delta$ ) a shear stress condition is imposed. This shear stress condition equates the interfacial shear stress to the change in surface tension (caused by temperature gradients at the interface) [8]:

$$\tau = \sigma' = \mu \frac{du}{dy} \quad (40)$$

Implementing these boundary conditions and integrating from 0 to  $\delta$  we have:

$$u = \frac{1}{\mu} \frac{dP_l}{dx} \left( \frac{y^2}{2} - \delta(y-\beta) \right) + \frac{b}{\mu} \frac{dT_{lv}}{dx} (y-\beta) \quad (41)$$

### 3.4 Continuity Equation

Considering continuity within the thin-film region provides a means of representing the mass flow rate in terms of liquid pressure gradient and interfacial temperature gradient.

The mass flow rate is represented as:

$$\dot{m} = \rho \bar{A} u \quad (42)$$

Where the cross-sectional area of the thin-film is represented as  $\bar{A} = dz dy$ , where  $dz$  is assumed as unity.

Substituting Equation 41 into Equation 42 and integrating from 0 to  $\delta$ , mass flow rate is now represented in terms of liquid pressure gradient and interfacial temperature gradient.

$$\dot{m} = \frac{1}{\nu} \frac{dP_l}{dx} \left( -\frac{\delta^3}{3} + \delta^2 \beta \right) + \frac{b}{\nu} \frac{dT_w}{dx} \left( \frac{\delta^2}{2} - \beta \delta \right) \quad (43)$$

### 3.5 Energy Equation

The energy equation can now be incorporated into the mathematical model. As heat is applied through the channel wall, it is conducted through the thin-film. As such, the energy equation is represented as:

$$\frac{\partial}{\partial x} \left( k_l \frac{\partial T}{\partial x} \right) + \frac{\partial}{\partial y} \left( k_l \frac{\partial T}{\partial y} \right) + \frac{\partial}{\partial z} \left( k_l \frac{\partial T}{\partial z} \right) + \dot{q} = \rho c_p \frac{\partial T}{\partial t} \quad (44)$$

Considering the thickness of the liquid film is very small, it can be assumed that the conduction heat transfer through the liquid is assumed to be present only in the direction

perpendicular to the substrate (y-direction). In fact, Stephan and Busse [36] calculated normal temperature gradients to be several orders of magnitudes larger than the gradients parallel to the surface. Also, considering that the thin-film receives heat from the substrate and does not generate its own heat. Equation 44 thus reduces to:

$$\frac{\partial}{\partial y} \left( k_l \frac{\partial T}{\partial y} \right) = 0 \quad (45)$$

### 3.5.1 Boundary Conditions

Two boundary conditions are applied when using the energy equation.

The rigid & planar substrate has a specified temperature, thus at  $y = 0$

$$T = T_w \quad (46)$$

At the liquid-vapour interface ( $y = \delta$ ) the conduction heat transfer rate is set equal to the evaporative heat flux.

$$-k_l \frac{\partial T}{\partial y} = \dot{m}_{evap}'' h_{fg} \quad (47)$$

Now applying boundary conditions 46 and 47 and integrating Equation 45, the following relation is determined:

$$\dot{m}_{evap}'' = \frac{k_l (T_w - T_{lv})}{\delta h_{fg}} \quad (48)$$

Considering there is a mass flow into the thin-film region (from the bulk region) and there is no mass flow out of the thin-film region (into the adsorbed region) one can create

a mass flow balance relating mass flow into the integral of the evaporative mass flux, thus generating this relationship:

$$\dot{m} = - \int_0^x \frac{k_l (T_w - T_{lv})}{\delta h_{fg}} dx \quad (49)$$

### 3.6 Liquid Pressure Gradient

There are the appropriate equations available to now determine a relationship for the liquid pressure gradient in terms of the interfacial temperature gradient.

Equating the equations developed for mass flow rate (Equations 43 and 49) and isolating for liquid pressure gradient, the following relation is obtained:

$$\frac{dP_l}{dx} = -b \frac{C_5}{C_4} \frac{dT_{lv}}{dx} - \frac{\nu}{C_4} \int_0^x \frac{k_l (T_w - T_{lv})}{\delta h_{fg}} dx \quad (50)$$

In Equation 50, variables  $C_4$  and  $C_5$  are integration constants and are defined in Table 8 found within Appendix A.

In further assembling the mathematical model, a further relationship for interfacial temperature gradient is developed through use of the Kelvin-Clapeyron model.

### 3.7 Kelvin-Clapeyron Model

As mentioned earlier, the Kelvin-Clapeyron model developed by Wayner [6] is used as a means of quantifying the local evaporative mass flux at the liquid-vapour interface associated with the interfacial temperature and pressure jump.

$$\dot{m}_{evap}'' = \frac{1}{h_{fg}} \left( h_{lv}^{cl} (T_{lv} - T_v) - h_{lv}^{kl} (P_d + P_c) \right) \quad (51)$$

Equating the two relations that describe the evaporative mass flux (Equations 48 and 51), a relation for the interfacial temperature can be developed which has no dependency on liquid pressure.

$$\frac{k_l}{\delta\eta} T_{lv}^{5/2} - \frac{k_l}{\delta\eta} T_w T_{lv}^{3/2} + \frac{Mh_{fg}}{T_v} T_{lv} - V_l b T_{lv} \kappa = Mh_{fg} + V_l \left( \frac{A}{\delta^3} + a\kappa \right) \quad (52)$$

### 3.8 Interfacial Temperature Gradient

From Equation 52, it is possible to develop a relation for interfacial temperature gradient.

This is obtained by differentiating Equation 52 and isolating for  $\frac{dT_{lv}}{dx}$ .

$$\frac{dT_{lv}}{dx} = \left( \frac{2T_v}{\delta^3} \right) \left( \frac{\chi + V_l \eta \sigma \delta^4 \kappa'}{\omega} \right) \quad (53)$$

Due to the nature of this problem, and the inherent size scale of Equation 53, placeholder variables  $\chi$  and  $\omega$  which are a collection of terms from the ODE to compact the equation.

They are described in full in Table 8 found within Appendix A.

### 3.9 Complete Model

With representations for both liquid pressure gradient and interfacial temperature gradient, the complete model can be assembled. This is done through substitution of Equations 50 and 53 into Equation 36. This yields the following:

$$\delta'' = \frac{3\delta'\delta''^2}{\alpha} - \frac{2T_{iv}\psi\chi}{\omega\delta^3\lambda} + \frac{\theta}{\lambda} \quad (54)$$

As above, in the interest of representing this equation in a reasonable manner, placeholder variables  $\chi$ ,  $\omega$ ,  $\psi$ ,  $\lambda$  and  $\theta$  are used which are collections of terms from the ODE. Further details can be found in Appendix A, as well as Table 8.

### 3.10 Initial Conditions

The inputs required to generate a solution for the mathematical model include values for  $\delta$ ,  $\delta'$ ,  $\delta''$  and  $T_{iv}$ . As such, through the equations generated thus far, system constraints can be generated as to ensure the input is within range and will provide as physical solution with a monotonically increasing thin-film.

#### 3.10.1 Adsorbed Thickness

The ability to calculate the adsorbed thickness provides a means of identifying an order of magnitude of the initial conditions. As previously mentioned, the adsorbed layer does not undergo evaporation as the intermolecular forces restrain the molecules. Using Equation 51 and setting the evaporative mass flux to zero provides a means in identifying

this adsorbed thickness. Also considering curvature is zero in the adsorbed region, the capillary pressure term is no longer considered. Now considering the thickness of the adsorbed layer it can be assumed conductive losses are negligible thus the interface temperature is taken as that of the channel wall [5,8]. Applying these simplifications the adsorbed thickness is calculated as:

$$\delta_o = \left( \frac{AV_l}{Mh_{fg}} \left( \frac{T_w}{T_w - T_v} \right) \right)^{1/3} \quad (55)$$

The complete derivation can be found in Appendix B.

### 3.10.2 Initial Condition Limits

Polansky [4] demonstrated initial condition maximum and minimum values imposed on the model in order to generate a physical solution.

The minimum and maximum initial conditions are derived from a mass flux balance of equating Equations 48 and 51.

### 3.10.3 Initial Condition Maximum

This condition is observed when the maximum interfacial temperature is applied, that is

$$T_{lv} = T_w.$$

$$\delta_{\max}^* = \frac{\alpha^{3/2}}{\sigma} \left( \frac{Mh_{fg}}{T_v V_l} (T_w - T_v) - P_d \right) \quad (56)$$

Now to ensure the thin-film falls within the physical solution we desire (that is monotonically increasing) the following inequality must be satisfied.

$$\frac{Mh_{f\beta}}{T_v V_i} (T_w - T_v) \geq \frac{A}{\delta^3} \quad (57)$$

### 3.10.4 Initial Condition Minimum

This condition is observed when the minimum interfacial temperature is applied, that is

$$T_{lv} = T_v.$$

$$\delta''_{\min} = -\alpha^{3/2} \left( \frac{k_l (T_w - T_v)}{V_i \sigma \delta \eta} T_v^{3/2} + \frac{P_d}{\sigma} \right) \quad (58)$$

Given Equation 58, it is seen that the limit imposed corresponds to a negative value for  $\delta''$ . Considering this, and knowing a monotonically increasing film is required, the lower limit for  $\delta''$  is set as  $\delta'' > 0$ .

# Chapter 4

## Numerical Model

With the development of a third order non-linear ODE, the profile and characteristics of the evaporating thin-film can be resolved. This formulation is similar to that of previous works [2,5,8,20] and thus, the nature of the governing equation is highly non-linear. This non-linear behaviour is especially sensitive to values of film thickness and its first derivative [2,5,8,20]. As a result, it cannot be simply integrated to obtain an analytical result. As such, numerical methods are employed in solving the profile of an evaporating thin-film.

Equation 54 can be treated as an initial value problem by specifying the conditions at the beginning of the thin-film region ( $x=0$ ). Treating Equation 54 as in initial value problem allows the use of a Runge-Kutta technique in solving the ODE. It is widely accepted that Runge-Kutta techniques are an efficient method of solving initial value problems [37]. This technique is implemented through MATLAB, and when the program is initiated several output plots are obtained portraying the heat transfer characteristics.

Considering this work is an extension of the work previously done by Polansky [4], the numerical method of solution has not changed significantly. The step-size has remained constant and is set to a value of one nanometer. This is done as to improve the stability of the code as it was determined with variable step size the code was more sensitive to applied perturbations. In an attempt to allow the code to generate solutions for an evaporating thin-film over a broader range of boundary conditions, Maple was used in the

generation of the governing equation. Currently the governing equation is coded into several individual calculations. It is anticipated by implementing the governing equation in one calculation (given the extreme sensitivity of equation) round-off error would be minimized and this would aid in generating more accurate and robust solutions.

## 4.1 Reduction of Order

As suggested above, numerical methods, in particular a Runge-Kutta technique would be used in the solution methodology. In order to effectively use numerical solving techniques, it is required that Equation 54 be subjected to a change of variables and thus a reduction of order.

Using the following change of variables

$$d_0 = \delta \tag{59}$$

$$d_1 = \delta' \tag{60}$$

$$d_2 = \delta'' \tag{61}$$

$$d_2' = \delta''' \tag{62}$$

We can now represent Equation 54 as a first order ODE.

$$d_0' = d_1 \tag{63}$$

$$d_1' = d_2 \tag{64}$$

$$d_2' = \frac{3d_1 d_2^2}{\alpha} - \frac{2T_v \psi \chi}{\omega \lambda d_0^3} + \frac{\theta}{\lambda} \quad (65)$$

## 4.2 Algorithm Outline

An overview of the algorithm is best seen through the block diagram found in Figure 7. Figure 8 and Figure 9 provide details of the Runge-Kutta and Maple portions of Figure 7 respectively. The combination of Figures 7-9 provides insight into the numerical methodology of solving Equation 65.

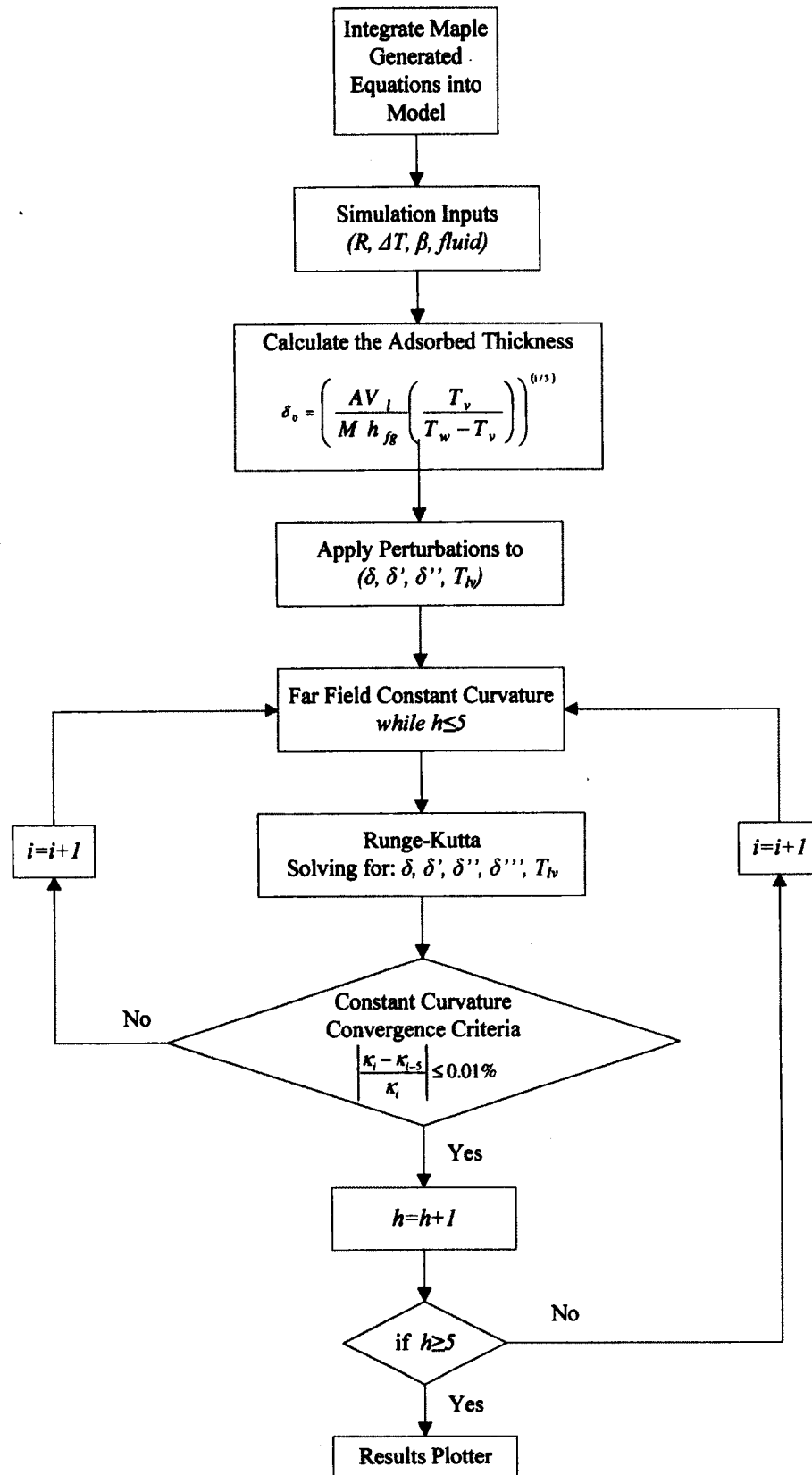


Figure 7: High level algorithm flow chart (adapted from [4])

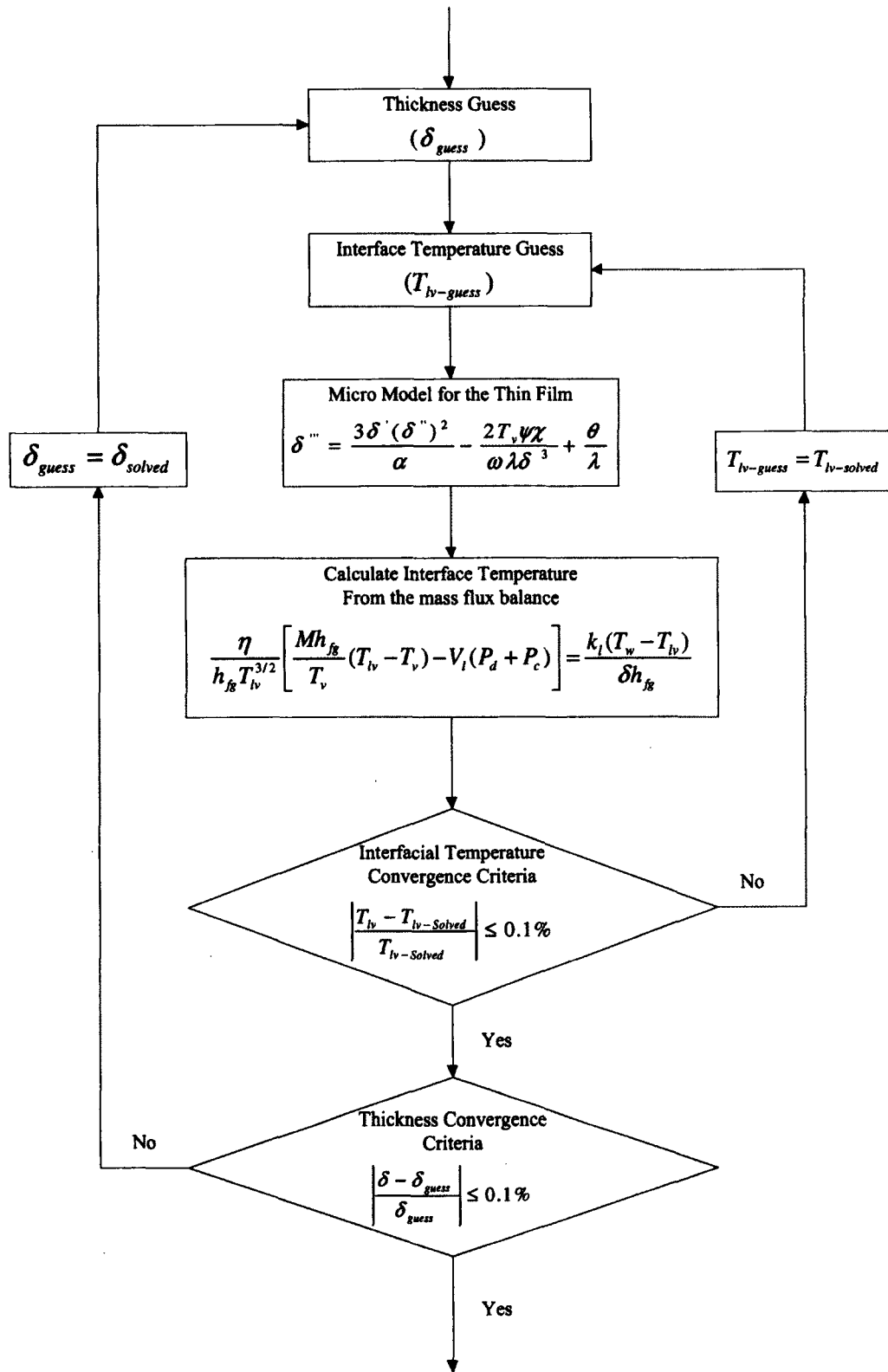
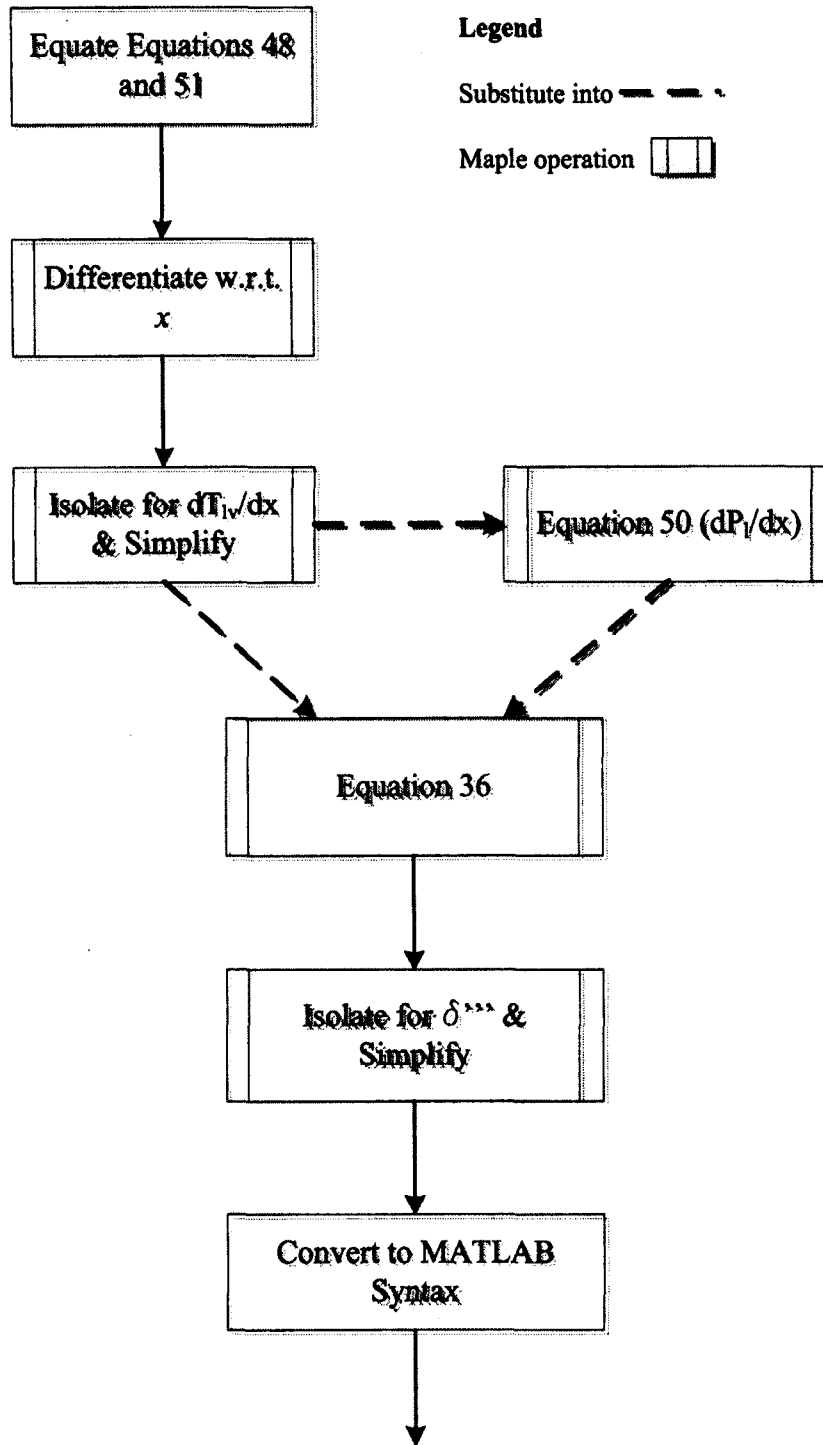


Figure 8: Runge-Kutta algorithm flow chart (adopted from [4])



**Figure 9: Maple algorithm flow chart**

### **4.3 Required Inputs**

The numerical method of solution generated requires user input to initiate the solving process. These input variables are designed to allow for variation within the model. The variables that can be altered include working fluid, channel width, applied superheat, wall slip length and accommodation coefficient. By altering these variables, the model boundary conditions are formed, and a set of initial conditions can be sought for a numerical solution.

### **4.4 Initial Conditions and Applied Perturbations**

As previously mentioned, in generating a solution to Equation 65, the problem is treated as an initial-value problem. From a purely mathematical standpoint, the following initial conditions would be used;  $\delta = \delta_0$ ,  $\delta' = 0$ ,  $\delta'' = 0$ ,  $T_{lv} = T_w$ . These initial conditions, although mathematically sound result in a trivial solution, which is not to be the physical solution of an evaporating thin-film (as it provides a solution of an adsorbed layer of infinite length).

In addressing this problem, many works [5,8,9,20,21] apply perturbations to the film thickness ( $\delta$ ), the first derivative ( $\delta'$ ) and the second derivative ( $\delta''$ ).

One can physically visualise these perturbations as a shift of the coordinate system in the positive  $x$  direction, such that the origin is now in the evaporating thin-film portion of the meniscus and no longer at the transition point (from adsorbed to thin-film). Considering this, the smallest perturbations are desirable as more of the thin-film can be captured;

especially the details nearest to the adsorbed region where several key attributes are most prominent.

Discussing these perturbations in further detail, each individual perturbation has a unique effect on the numerical model. The main perturbations being deal with the thin-film thickness and its corresponding derivatives. As such the perturbations are represented as follows.

- Perturbation 1 ( $\varepsilon_1$ ) – Applied to film-thickness ( $\delta$ )
- Perturbation 2 ( $\varepsilon_2$ ) – Applied to first derivative ( $\delta'$ )
- Perturbation 3 ( $\varepsilon_3$ ) – Applied to second derivative ( $\delta''$ )
- Perturbation 4 ( $\varepsilon_4$ ) – Applied to the interface temperature and is represented as

$$T_{lv} - T_w.$$

Beginning with  $\varepsilon_1$  it is important to not provide too large of a perturbation. Different techniques have been used in providing values for this perturbation. Wang et al. [5] calculates the initial adsorbed thickness using Equation 55. Wang continues with applying  $\varepsilon_1$  as 3.4 nm. This perturbation is rather large especially at lower superheats as discussed below in the results section. As a result, for this numerical solution,  $\varepsilon_1$  is set as 0.01% - 1% of the calculated adsorbed film thickness (it increases with increasing superheat). This provides a sensible means of consistently applying a value for  $\varepsilon_1$ , and from here seeking out an appropriate value for  $\varepsilon_2$ .

In the third order models such as [2,8],  $\varepsilon_2$  is the value most sensitive when generating a solution. Considering the extreme sensitivity, it is the value that is searched out in finding a solution for the desired far field curvature. This value is shown to be sensitive

to several decimal places. Whether this is an artifact of the model or the mathematical nature of the equation is unknown, however extreme sensitivity to this value is reported in other works as mentioned above.

The third perturbation,  $\varepsilon_3$  is not nearly as sensitive to the model. This perturbation was shown to have very little effect on third order models, however as Wang [5] suggests, in a fourth order model the primary sensitivity falls on  $\varepsilon_3$ . Considering this is a third order model, a value of  $1 \times 10^{-3}$  is selected in all simulation cases.

As mentioned above  $\varepsilon_4$  is the perturbation applied to the interface temperature. Considering the size scale of the previous perturbations, the coordinate system is not moved enough to see a change in the interface temperature from that of the wall. As a result, the solution is not sensitive to  $\varepsilon_4$  and it is set at a value of zero for all simulations.

## **4.5 Model Evaluation of Various Terms**

The numerical model has various terms which are dealt with on an individual basis which requires some additional explanation. The adsorbed thickness and the integral term are of particular interest and will be discussed in more detail.

### **4.5.1 Adsorbed Thickness**

As mentioned previously, the adsorbed thickness is calculated using Equation 55. As such it is treated as uniform thickness extending along the channel wall. This is based off of experimental work of Buffone et al. [7] and the theoretical works of Wayner et al.

[1,6,11,21,24,33,38]. This provides a size scale in determining the initial perturbations and seeking an appropriate solution for the desired far-field curvature.

### 4.5.2 Integral Term

In numerically solving Equation 65, the integral term found within  $\theta$  must be appropriately dealt with. This integral term is originally contained within Equation 50 which represents the liquid pressure gradient.

$$\int_0^x \frac{T_w - T_{lv}}{\delta} dx \quad (66)$$

This integral term is the main reason why some authors will use a 4<sup>th</sup> order model. However, considering the thin-film profile is solved numerically, it is logical to evaluate Equation 66 numerically. As such, the integral term can be evaluated at each step  $x_i$ , and a cumulative running total is kept. In doing this, at each step  $x_i$ , the thin-film thickness and interfacial temperature must be first found.

For both thin-film thickness and interfacial temperature values, the same technique is used. This technique uses the adjacent (or previous) value at each step such as to generate a temporary solution. This is demonstrated as letting  $T_{lv(i)} = T_{lv(i-1)}$  and  $\delta_i = \delta_{i-1}$ .

Employing the above technique, a numerical value for Equation 66 is achieved allowing for Equation 65 to be solved. Upon solving, the calculated values in the current step  $i$ , for  $T_{lv}$  and  $\delta$  can be compared to the guessed values. If this difference is greater than the specified tolerance, the guess value is replaced until the desired tolerance is reached.

This is why the adjacent values are used initially such as to provide an accurate value in an attempt to improve computation time.

The integral value will be calculated at each step; however a cumulative sum must be kept. This is done through the following:

$$\int_0^x \frac{T_w - T_{lv}}{\delta} dx = \overbrace{\int_0^{x_{i-1}} \frac{T_w - T_{lv}}{\delta} dx}^{\text{Cumulative-Total}} + \overbrace{\int_{x_{i-1}}^x \frac{T_w - T_{lv}}{\delta} dx}^{\text{Current-Integral}} \quad (67)$$

Now, when dealing with the current integral, a numeric technique must used. In doing this trapezoidal rule was selected as given below [39]:

$$\int_{x_{i-1}}^x \frac{T_w - T_{lv}}{\delta} dx \approx (x_i - x_{i-1}) \left( \frac{\left( \frac{T_w - T_{lv}}{\delta} \right)_i + \left( \frac{T_w - T_{lv}}{\delta} \right)_{i-1}}{2} \right) \quad (68)$$

It is of note to mention that other more accurate methods of numerical integration were tested such as Simpsons 3/8<sup>th</sup> rule. These more intricate methods produced nearly identical results to that of trapezoidal rule as the step size of one nanometer is sufficiently small. As such trapezoidal rule is used as it is the least computationally taxing.

## 4.6 Runge-Kutta Technique

As mentioned above, Runge-Kutta techniques are often used in solving initial-value problems. This method of numerical solution is common in literature and various Runge-Kutta techniques are used [2,5,8,9,17,20,33,36]. In staying consistent with [5] a Runge-

Kutta technique developed by Dormand and Prince [37] is used. This technique is referred to as RK5 (4) 7M and is a modified 5<sup>th</sup> order technique designed to produce small principal truncation terms [37]. The Runge-Kutta coefficients used in this technique are seen in Table 2.

**Table 2: Coefficients for RK5 (4) 7M**

$c_i$	$a_{ij}$						$\hat{b}_i$	$b_i$
0	0	0	0	0	0	0	$\frac{35}{384}$	$\frac{5179}{57600}$
$\frac{1}{5}$	$\frac{1}{5}$	0	0	0	0	0	0	0
$\frac{3}{10}$	$\frac{3}{40}$	$\frac{9}{40}$	0	0	0	0	$\frac{500}{1113}$	$\frac{7571}{16695}$
$\frac{4}{5}$	$\frac{44}{45}$	$-\frac{56}{15}$	$\frac{32}{9}$	0	0	0	$\frac{125}{192}$	$\frac{393}{640}$
$\frac{8}{9}$	$\frac{19372}{6561}$	$-\frac{25360}{2187}$	$\frac{64448}{6561}$	$-\frac{212}{729}$	0	0	$\frac{2187}{6784}$	$-\frac{92097}{339200}$
1	$\frac{9017}{3168}$	$-\frac{355}{33}$	$\frac{46732}{5247}$	$\frac{49}{176}$	$-\frac{5103}{18656}$	0	$\frac{11}{84}$	$\frac{187}{2100}$
1	$\frac{35}{384}$	0	$\frac{500}{1113}$	$\frac{125}{192}$	$-\frac{2187}{6784}$	$\frac{11}{84}$	0	$\frac{1}{40}$

The above coefficients are coded into a MATLAB subroutine. The Runge-Kutta solver was verified to be working after expected results were achieved for a simple test case of a mass spring system. The MATLAB subroutine is set up in such a way that the coefficient matrix is pre-defined, along with the restriction of a user-defined constant step size. The Runge-Kutta solver runs by first calling each of the first order differential equations (Equations 63-65) and solves for the values of  $\delta_i$ ,  $\delta_i'$ ,  $\delta_i''$  and  $\delta_i'''$ .

### 4.6.1 Interfacial Temperature

The interfacial temperature is solved at each step. It is found through the use of the evaporative mass flux balance first introduced as Equation 52. A bisection search algorithm is used in obtaining the correct value. The upper and lower limits are imposed by the wall temperature and the bulk vapour temperature respectively.

This process calculates the interfacial temperature from the intermediate values from the Runge-Kutta solver. From which, the interface temperature value used in the integration term (Equation 66) is solved. For the initial pass through the Runge-Kutta solver, the information returned is based on the estimated values of film thickness and interfacial temperature. The new temperature calculated from this first pass is compared with the guess value of  $T_{iv(i-1)}$ . If the difference between the values is too large the updated interfacial temperature is supplied to the integral term as the new guess value. This process will repeat until the convergence criterion is satisfied. This convergence criterion is set as:

$$\left| \frac{T_{iv_{guess}} - T_{iv_{solved}}}{T_{iv_{solved}}} \right| \leq 0.01\% \quad (69)$$

The criterion is set at this value to ensure solution divergence does not occur.

### 4.6.2 Film Thickness

The film thickness is treated in an identical manner to that of the interfacial temperature, as Equation 66 also contains a  $\delta$  term. The process is initiated once the interfacial temperature value has reached convergence for the current step. Again, the Runge-Kutta produced value of film thickness is compared to the guess value. If convergence is not

met, a new value is generated and the process repeats. As above the convergence criterion is set as:

$$\left| \frac{\delta_{guess} - \delta_{solved}}{\delta_{solved}} \right| \leq 0.1\% \quad (70)$$

## 4.7 Constant Curvature

The final step in generating a thin-film profile is ensuring the profile is terminated at the point of constant curvature. As mentioned above, when constant curvature is reached, the film has now traversed into the bulk region where our model is no longer valid.

In imposing a constant curvature condition, there are two key attributes of the thin-film to keep in mind.

The first of these attributes is especially important at lower superheats. As will be discussed below in the results, at lower superheats, the change from adsorbed region to evaporating thin-film is rather gradual. As a result it is possible for the code to satisfy the convergence criterion during this initial transition. As such, the code does not start to seek constant curvature until 75 steps have been complete. This ensures that this transition region has been surpassed.

The second attribute deals mainly with the nature of the curvature profile. Before constant curvature is reached, there is often an overshoot in the curvature value. This overshoot has an apex value. Considering a step size of one nanometer, surrounding values from the apex can satisfy the curvature criterion. This is undesirable as it provides

an incomplete thin-film profile. In an effort to avoid this, the code only breaks for the constant curvature condition when 5 consecutive points are achieved within tolerance. As a result the applied constant curvature criterion is set as:

$$\left| \frac{\kappa_i - \kappa_{i-5}}{\kappa_i} \right| \leq 0.01\% \quad (71)$$

## 4.8 Far Field Curvature

The final piece of the process in developing a model for an evaporating thin-film meniscus is satisfying the thin-film profile such that the constant curvature is reached for the desired far field value. As mentioned earlier, the desired far-field curvature is governed by the Young-Laplace solution and is represented as  $1/r$  or  $2/H$  where  $r$  and  $H$  are channel radius and height, respectively.

Achieving the desired far field value is based on the applied perturbations. As mentioned earlier, the model is most sensitive to the slope perturbation,  $\varepsilon_2$ . As such, this is the value that is varied in determining different values of far field curvature. Considering the highly non-linear behaviour of the equation, a search algorithm cannot initially be applied to find the value of  $\varepsilon_2$  that matches the desired far field value as the bracketing interval would be too large. As a result the solution will likely be divergent with the broad upper and lower limits. Providing a small enough bracketing interval allows for a bisection search algorithm to be run and search out the value of  $\varepsilon_2$  that matches the desired far field curvature. This smaller bracketing interval is sought out by the user and generally will find values of  $\varepsilon_2$  that are both above and below the desired solution.

## **4.9 Sources of Error**

In utilizing any numerical method, there is always some associated error. The first and perhaps most obvious source of error is the perturbation of the initial conditions. As projected, in minimizing this error, the smallest possible initial conditions were used such as to perturb the coordinate system the least. If too large a perturbation is used, the solution can begin too far into the thin-film region and some of the effects of disjoining pressure go unrealised.

In addition to the perturbations, the solution is very sensitive to input data. When carrying through so many individual calculations the possibility for round-off error affecting results is large. As mentioned earlier, in an attempt to reduce the amount of calculations used, Maple was used to generate the main equation and as such Equation 65 is solved in one calculation.

# Chapter 5

## Numerical Results

The numerical model used to generate the solution of a thin-film meniscus was created in MATLAB. The code was developed by Polansky [4] and altered such that a thin-film solution could be resolved a broader case of boundary/initial conditions. Polansky confirmed that the numerical model matches up with basic assumptions applied in the derivation. Polansky also demonstrated the highly non-linear behaviour of the third-order ODE used in modelling the evaporating thin-film.

The following results provide tangible comparison to published values, verifying the performance of the current numerical model in use. An in-depth analysis on the effect of accommodation coefficient on the thin-film solution is also performed, as this parameter is often overlooked in literature. The effect of varying applied superheat up to values of 5 K is also studied, as many researchers fail to capture behaviour of these higher superheat values. A solution unifying that of the augmented Young-Laplace equation used within the thin-film region with the constant curvature condition of a standard Young-Laplace solution is also presented.

The numerical model is run and compared to published values to confirm both the qualitative and quantitative validity of results. There are two comparisons shown as to confirm that the model can produce the same results as papers which solve the problem using either a 3<sup>rd</sup> or a 4<sup>th</sup> order ODE.

## 5.1 General Results

This is first done in comparison to Wee et al. [8] using the following input parameters. The applied perturbations are not specified within the Wee paper. The perturbations used in the numerical model are also listed below. The numerical model uses variable thermophysical properties in all instances.

**Table 3: Numerical model input values – Wee comparison [8]**

<b>Input</b>	<b>Value</b>
<b>Applied Superheat</b>	0.01K
<b>Vapour Temperature</b>	300 K
<b><math>\varepsilon_1</math> – Thickness Perturbation (<math>\delta_o</math>)</b>	0.01% Adsorbed Thickness [m]
<b><math>\varepsilon_3</math> – Perturbation applied to <math>\delta''</math></b>	1e-003

\*Calculated using Equation 55

The numerical results are compared graphically from Figures 10-19 for the case of the Wee et al [8].

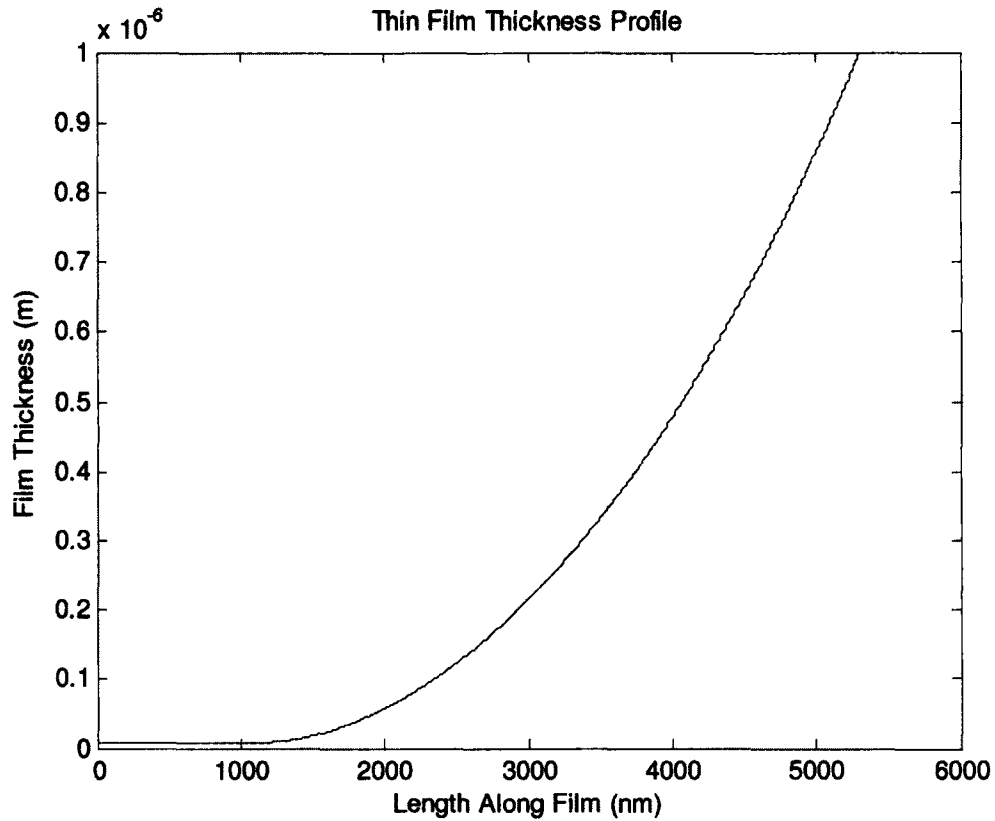


**Figure 10: Thin-film thickness**

Observing Figure 10 the qualitative trend is consistent with Wee et al [8]. The adsorbed region has nearly zero slope. It is in this region van der Waals forces (disjoining pressure) are dominant and there is no evaporation. As the thickness begins to increase, van der Waals forces are less pronounced and the thickness increases with length. It is in this region where the primary evaporative effects are incurred and a rise in liquid pressure is observed such as to satisfy the augmented Young-Laplace equation.

Comparing quantitatively with Wee, the profile matches very nicely however is approximately 1300 nm shorter in overall length at a height of  $1\mu\text{m}$ . This deviation can be attributed to a difference in applied thickness and slope perturbations. Since Wee does not mention the perturbations used (and these perturbations have a significant effect of

thin-film profile), the profile cannot be exactly matched. By publishing the perturbations used, the numerical solution has complete transparency and can be shown to be more robust for a variety of solving situations.

It is of note to mention that Wee's solution does not provide a boundary condition explicitly defining the transition from the thin-film region to the bulk/intrinsic meniscus. In the numerical model used, an applied condition of 5 constant curvature points is used as this transition point. The reasoning for selecting 5 consecutive points is discussed in the numerical model. Implementing this to the thin-film solution above, the length of the thin-film is significantly reduced to 2669 nm. At this point constant curvature has been reached and a standard Young-Laplace model can be used to model the rest of the meniscus.

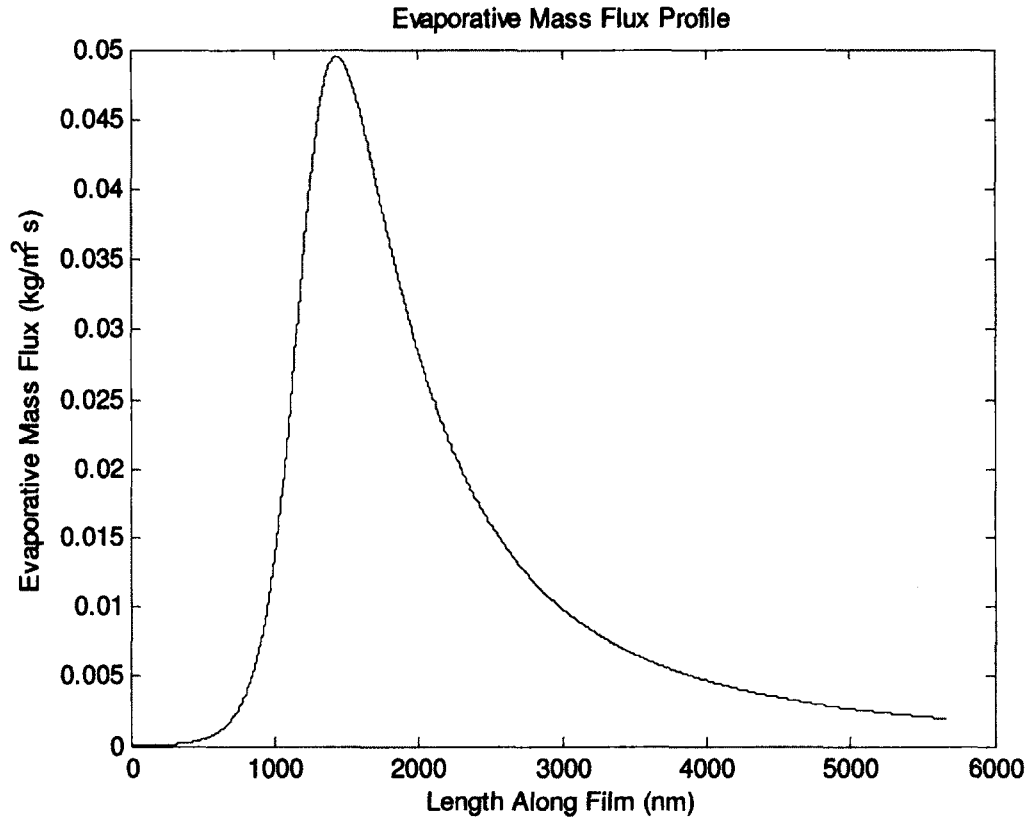


**Figure 11: Evaporative mass flux**

Observing the evaporative mass flux profile above, it is clear that the peak of evaporative mass flux occurs shortly after the adsorbed region terminates. This is consistent with published results [2,5,6,8]. This peak is dependent on the values used for accommodation coefficient, which will be discussed in Section 5.2. The evaporative mass flux profile closely agrees with theory, which suggests that at length zero, there is no evaporative mass flux, as well as entering the intrinsic meniscus evaporative mass flux is also zero. The first of these boundary conditions is satisfied by observing Figure 11, however at the end of the thin-film, a small evaporative mass flux still exists. This can be explained through the use of the mathematical model. While modelling the characteristics of the thin-film, an augmented Young-Laplace equation is used. As the

thin-film region transitions to the intrinsic meniscus, a standard Young-Laplace model should take over, which would provide zero evaporative mass flux. As a result, the residual mass flux can be attributed to the use of the augmented Young-Laplace equation entering in the intrinsic region. This also confirms that the mathematical model is accurate, as the solution tends to that of the Young-Laplace model.

Wee et al. [8] does not accurately satisfy the first of the boundary conditions mentioned above. This suggests that either there are inaccuracies within modelling the adsorbed region, or the thin-film model starts after the transition from adsorbed to the transition region has taken place. Either case would explain the presence of an initial mass flux, as it is well documented in literature that in the adsorbed region, as a result of overwhelming van der Waals interactions between fluid and substrate that evaporation does not take place [8,10].

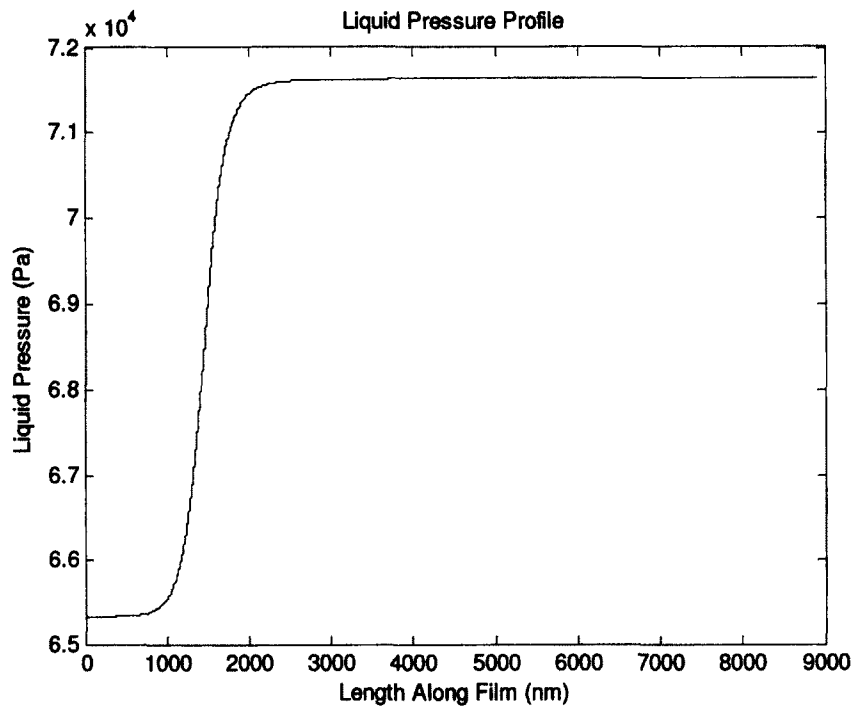


Figure 12: Liquid pressure profile

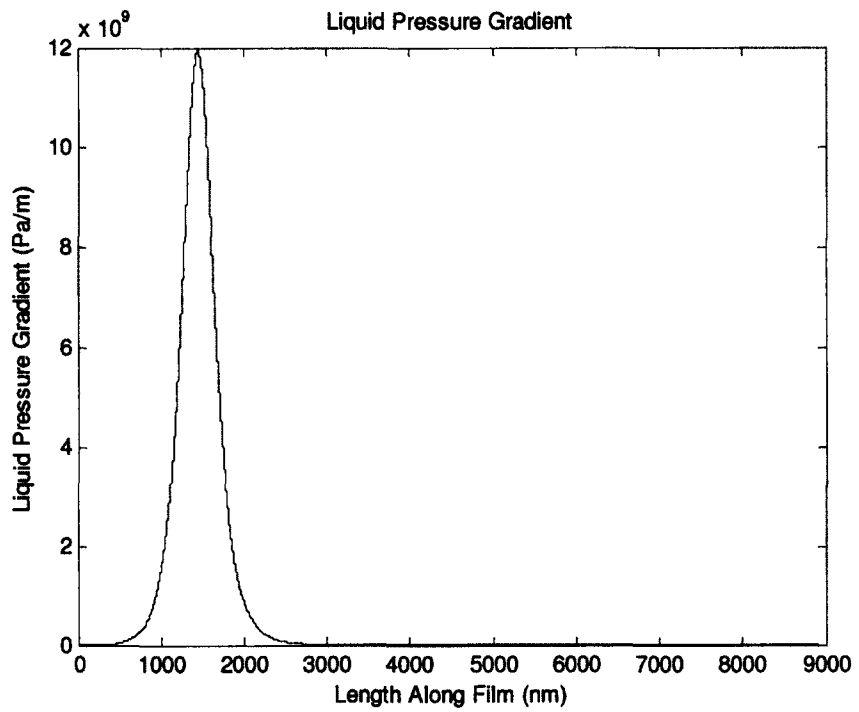


Figure 13: Liquid pressure gradient

Observing Figure 12 and Figure 13 representing liquid pressure profile and the liquid pressure gradient respectively, several trends are observed.

The liquid pressure profile is nearly identical to that produced by Wee et al. [8]. Leaving the adsorbed region and entering the transition region, the liquid pressure increases quickly. This is to balance the effect of a rapidly declining disjoining pressure as the thin-film thickens and van der Waals forces become less dominant. This directly corresponds to the liquid pressure gradient, which peaks during this transition from dominant disjoining pressure to liquid pressure.

When compared to the liquid pressure gradient produced by Wee et al., the magnitude of the peak is approximately four times larger, yet with a length of about one quarter. This suggests that the area under the curve is approximately equal which is confirmed by analysing the integrand term within the mathematical model. This corresponds to the near identical liquid pressure profile.

The discrepancy is due to the slight distortion of the thin-film profile, as the liquid pressure gradient is directly dependent on this profile. Given the lack of initial conditions presented by Wee, it is very difficult to directly match the thin-film profile. Throughout this results section several results will be portrayed which include the initial conditions used to promote transparency in the thin-film solutions.

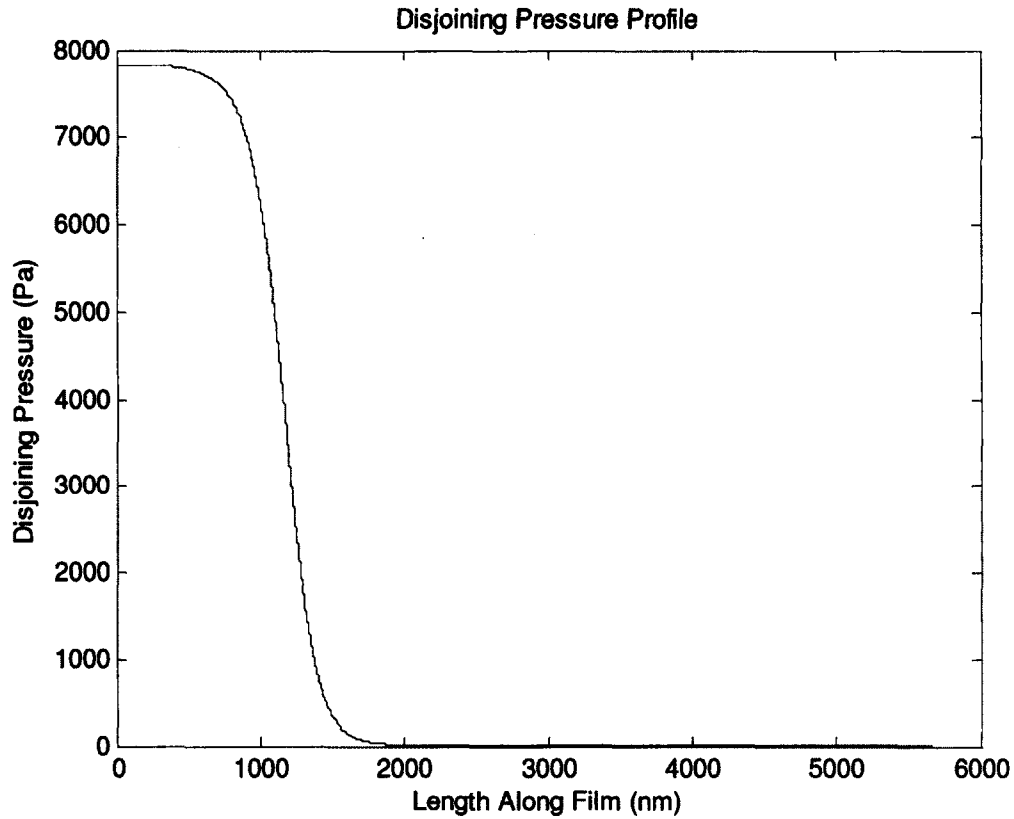


**Figure 14: Disjoining pressure profile**

The above disjoining pressure profile corresponds expectedly with the liquid pressure profile. The anticipated decay in disjoining pressure is observed with an increase in thin-film length. This is counteracted by an increase in liquid pressure as the thin-film length increases. This is attributed to the force balance used in the derivation for the numerical model. As the thin-film length increases, the height of the film also increases. This reduces the effects of the van der Waals forces which create such a pronounced disjoining pressure within the adsorbed region.

It is of note to mention that the drop in disjoining pressure and increase in liquid pressure occurs in the region where evaporative mass flux peaks (seen above in Figure 11). This is consistent with published numerical results [5,9,14].

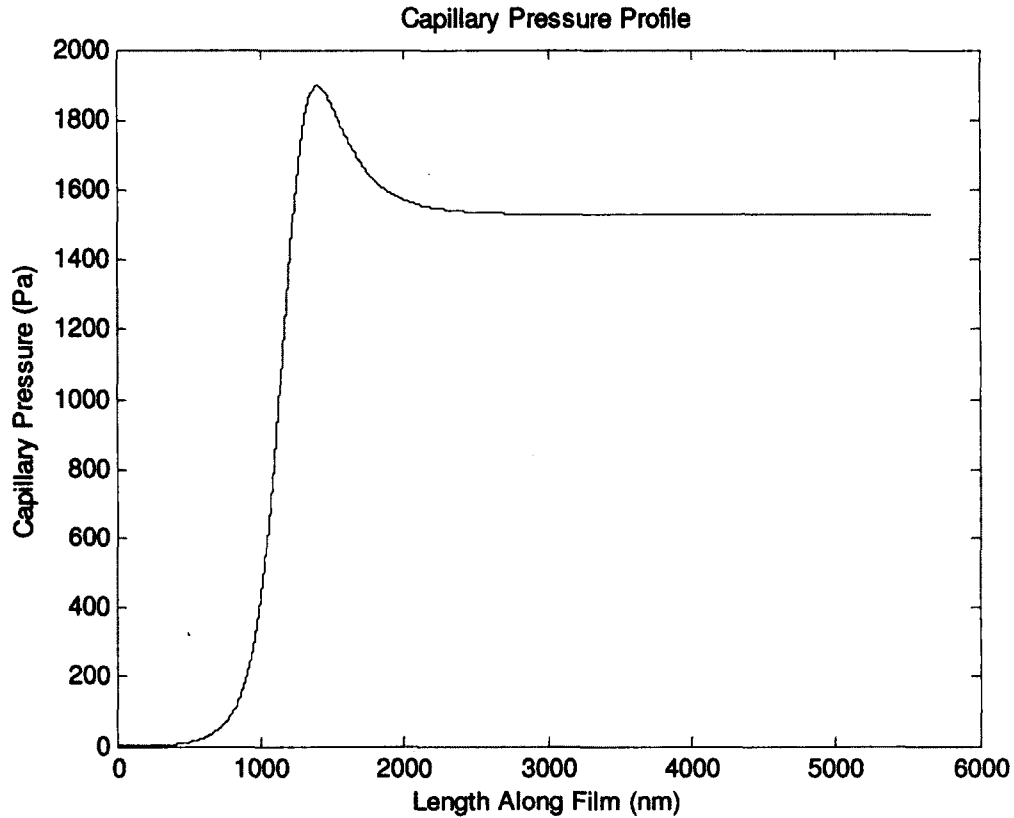


**Figure 15: Capillary pressure profile**

The final pressure profile to consider within the thin-film is the capillary pressure. The profile can be seen in Figure 15. The capillary pressure is related directly to the curvature of the thin-film (as  $P_c$  is a function of curvature, Equation 3). At the start of the thin-film near the adsorbed region, there is very minimal curvature and as a result a very small capillary pressure. This agrees with the initial dominance of disjoining pressure. As the thin-film increases, the curvature also increases resulting in a subsequent increase in capillary pressure. This is consistent with the force balance used in derivation. The composite pressure profile provides a summary of the pressure changes within the thin-film and can be seen below in Figure 16.

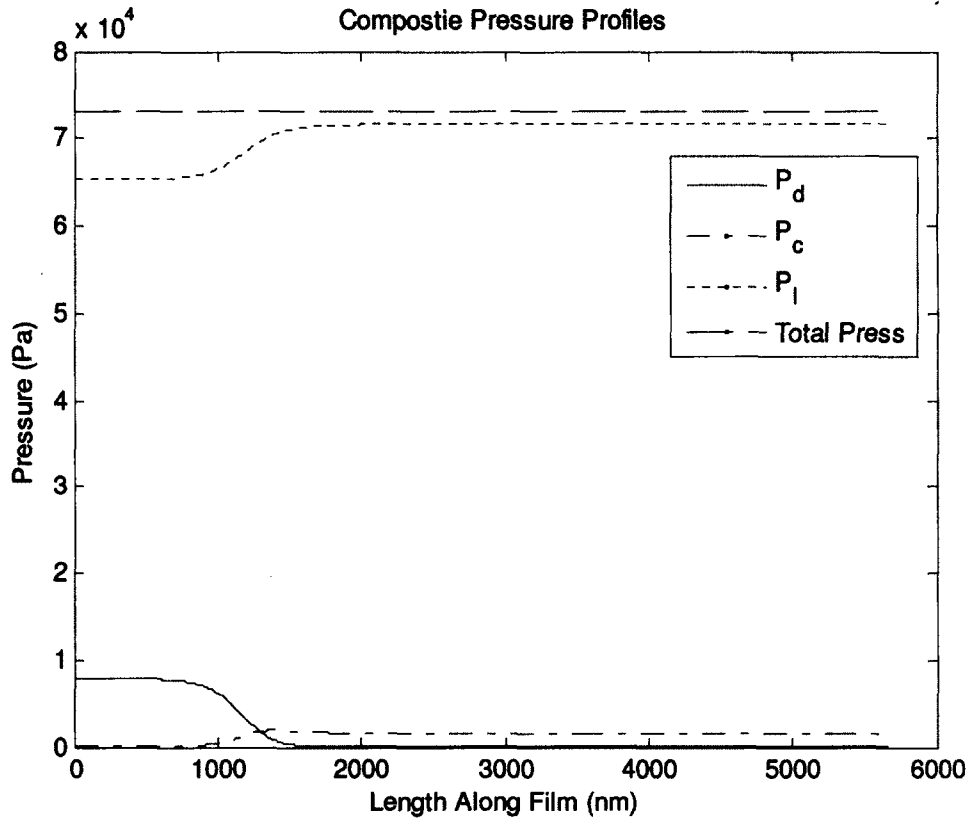


**Figure 16: Composite pressure profiles**

As seen from the composite pressure profile the total pressure is held constant throughout verifying the force balance used in generating the augmented Young-Laplace equation and the assumption of constant vapour pressure.

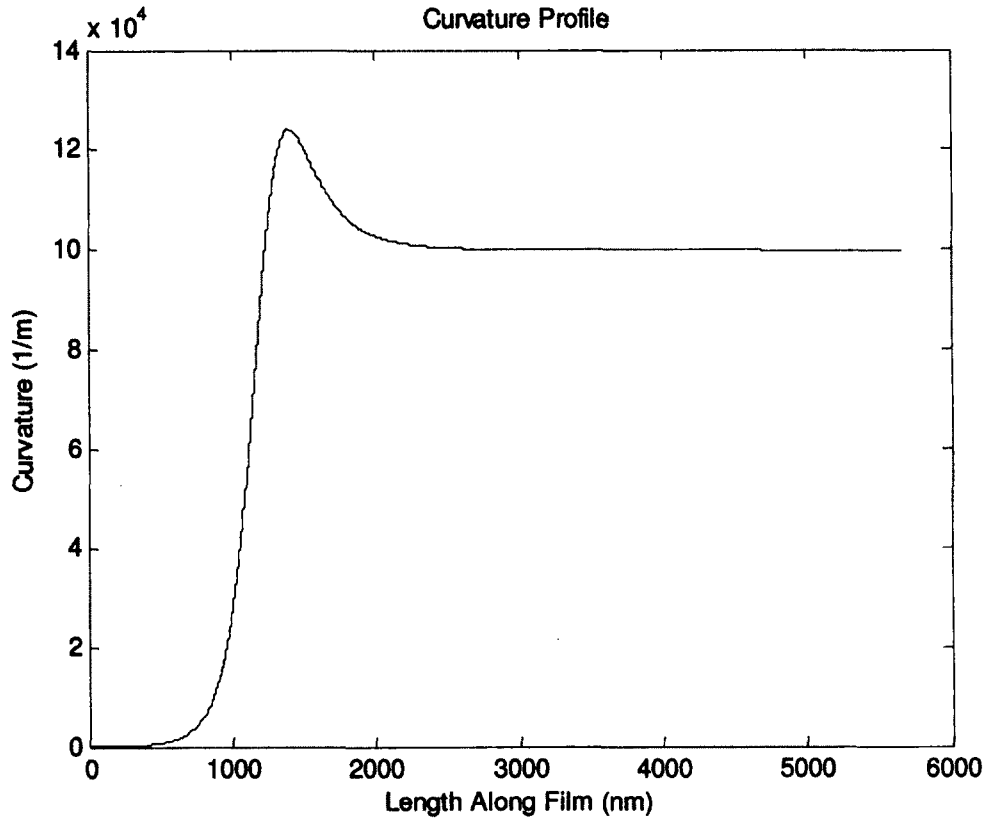


**Figure 17: Curvature profile**

Seen in Figure 17 is the curvature profile. This profile shows the continuous increase in curvature, until it plateaus at the far end of the thin-film. This plateau is indicative of the constant curvature condition mentioned earlier. When curvature is constant, a Young-Laplace solution has been attained, thus suggesting the termination of the thin-film region where the augmented Young-Laplace solution is used. The constant curvature is within 0.01% of the  $1/r$  value input. The overshoot seen in the profile is consistent with that seen in both experiment and literature, particularly in Panchamgam et al. [23,40].

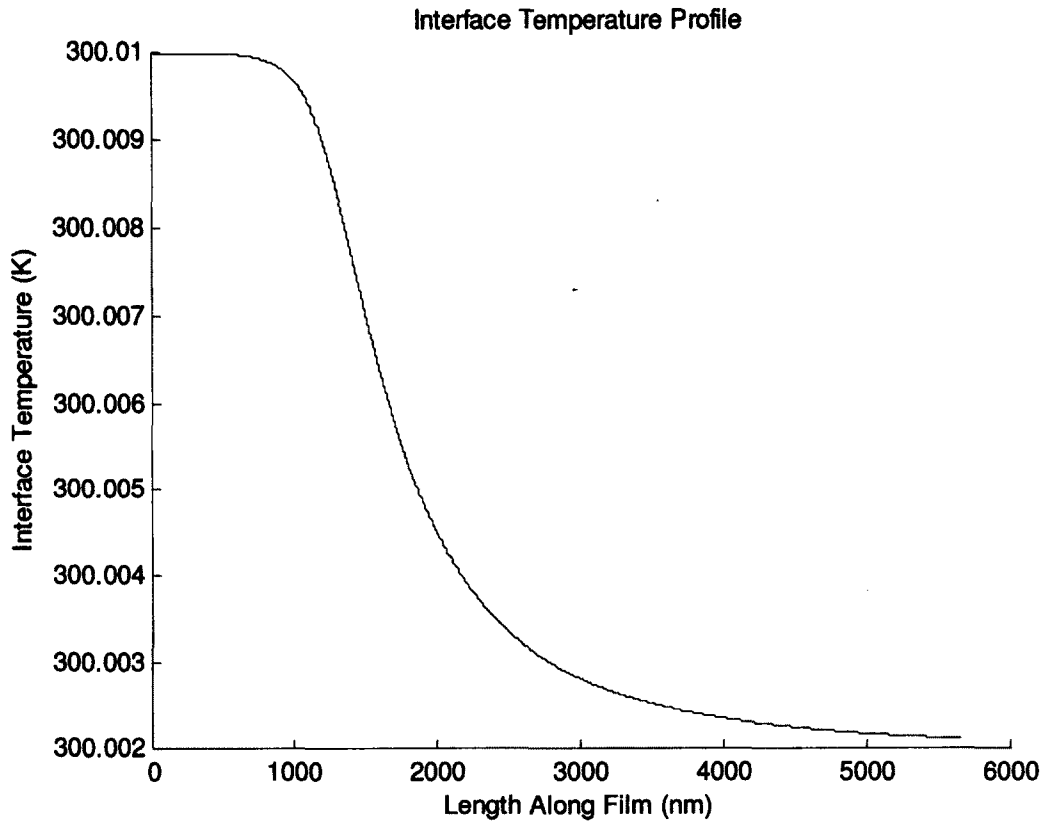


**Figure 18: Interface temperature profile**

Figure 18 represents the interfacial temperature profile for the thin-film solution. As seen from the profile, this model was run with an applied superheat of 0.01 K. This result is consistent with that of literature, where the majority of the temperature drop occurs just outside of the adsorbed region [5]. This trend can be explained through conductive losses and the cooling effect from evaporation [4].

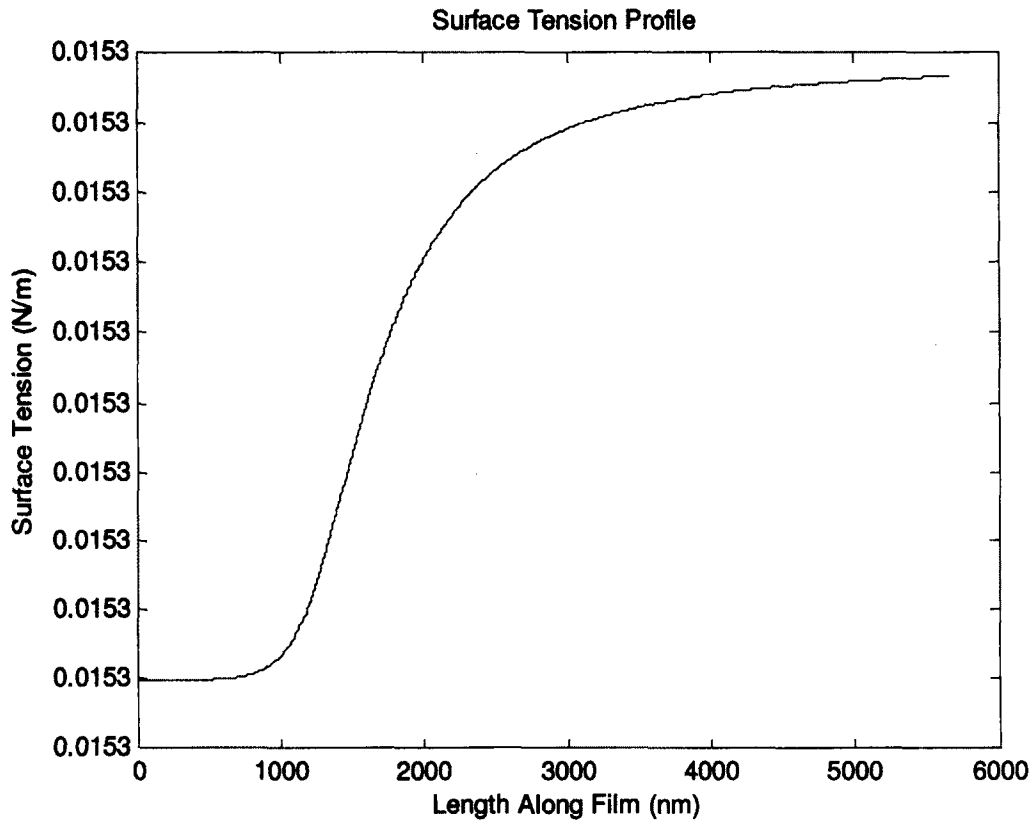


**Figure 19: Surface tension profile**

The surface tension profile has very minimal change along the length of the film. This profile insures that the thermophysical properties of the working fluid are indeed changing along the length of the thin-film. Very little variation is anticipated, as suggested by the interfacial temperature profile. This change in temperature is the sole variable that accounts for change in surface tension, thus verifying the model is working as anticipated. This also demonstrates Marangoni (thermocapilarity) effects are captured in the model.

As a further demonstration of the robustness of the model, a further comparison is made to results produced by Wang et al. [5]. This model uses a slightly different solution methodology, of note, is the use of a fourth order differential equation, as opposed to a third order differential equation. In comparing results, discrepancies can be attributed to this difference in order.

The following input parameters are used in comparison.

**Table 4: Numerical model input values – Wang comparison [5]**

<b>Input</b>	<b>Value</b>
<b>Applied Superheat</b>	1 K, 5 K, 20 K
<b>Vapour Temperature</b>	300 K
$\epsilon_1$	1.69e-009 [m]
$\epsilon_3$	1e-003

It is of note that Wang et al. [5] use calculated values for the adsorbed thickness, and specifies a value for the thickness perturbation ( $\epsilon_1$ ) which is on the same order of magnitude. Using these values, a bisection search is performed determining suitable values for the slope perturbation ( $\epsilon_2$ ) which create a thin-film solution. These slope perturbations are listed in the above table for each superheat.

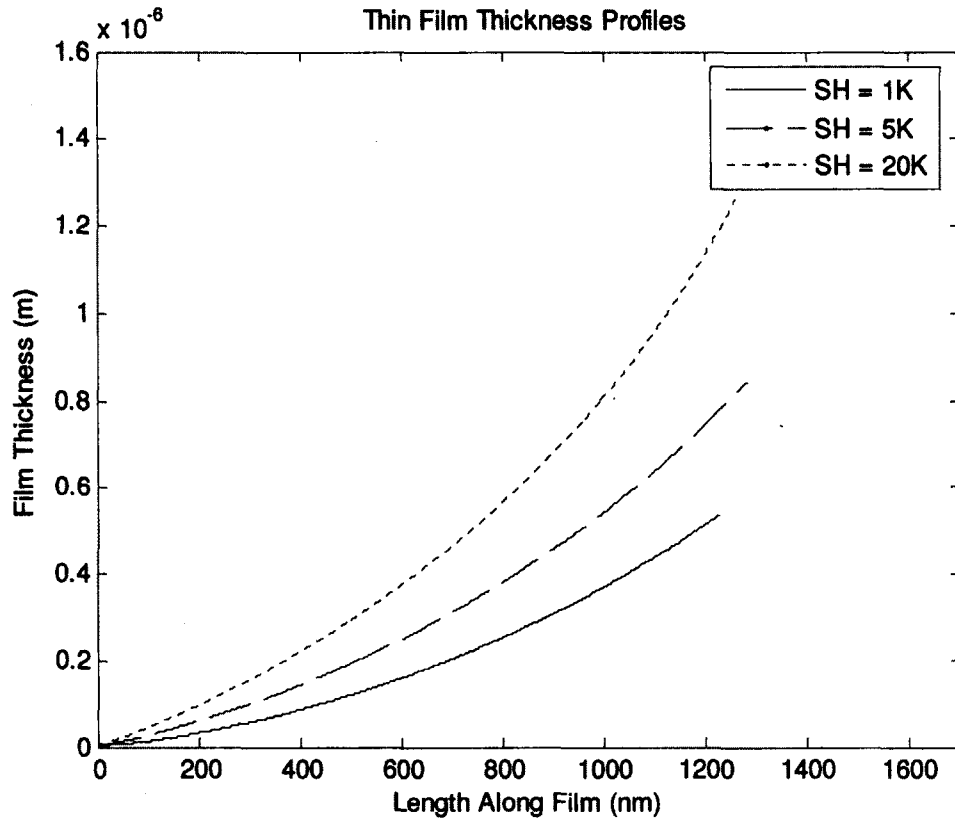


**Figure 20: Thin-film profiles at various superheats**

Figure 20 corresponds nicely with the data presented by Wang et al. [5]. With an increasing applied superheat, the thin-film possesses a much greater thickness for a corresponding length along the film. It is seen from the figure that the adsorbed region appears to be difficult to identify with these profiles. This is a direct result of the initial conditions used by Wang. By applying such a large perturbation to the adsorbed thickness, the numerical model begins at a length in which the adsorbed region has been surpassed.

A more in depth analysis at the effect of varying superheat is performed in Section 5.3.

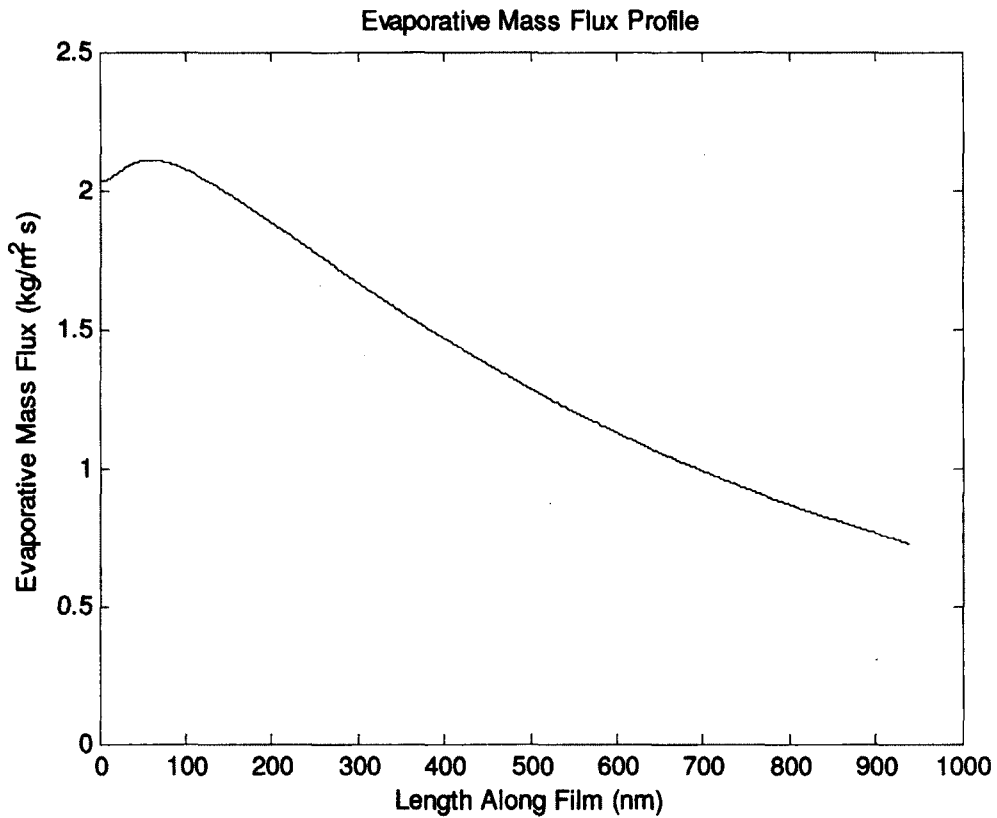


**Figure 21: Evaporative mass flux profile**

The effect of the large thickness perturbation can be seen clearly in Figure 21. This figure represents the evaporative mass flux profile for a 1 K applied superheat. As seen, the evaporative mass flux does not start at zero, implying that evaporation is occurring and as a result of the large initial perturbation. This demonstrates that the adsorbed region is surpassed by the large perturbation.

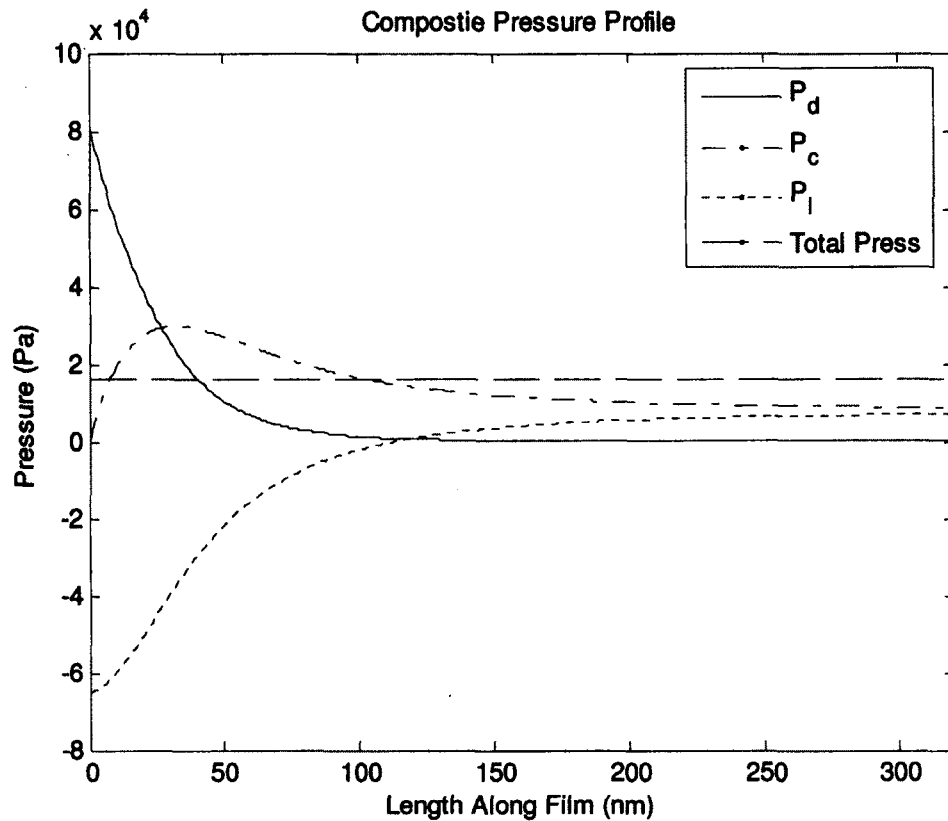


**Figure 22: Local composite pressure profiles**

In Figure 22, the composite pressure profiles also provide a nice comparison to Wang et al. [5]. The above figure represents the pressure profiles for 1 K superheat. At these increased superheat levels, the disjoining pressure is much more pronounced as the adsorbed region decreases in height. This strengthens the effect of the van der Waals forces and thus increases disjoining pressure significantly. As a result, to maintain pressure balance used in the augmented Young-Laplace equation an absolute negative liquid pressure is seen. This, although a rather abstract concept, has been documented in literature [28]. It is speculated that this negative liquid pressure occurs in regions where the liquid film is being pulled by the relatively cooler liquid in the meniscus, and also towards the centre due to high disjoining pressure [28]. In an attempt to omit this, many

authors, such is the case with Wang, use a  $\Delta P_l$  instead. With this difference in mind the above composite pressure profile for a 1 K superheat corresponds nicely with that of Wang et al. [5].

Observing Figure 22, the disjoining pressure and liquid pressure are already decreasing and increasing respectively at a length of zero, as expected with the large initial perturbation.

## **5.2 Effect of Accommodation Coefficient**

As mentioned in the literature review (Section 2.2.5) the accommodation coefficient which is present in the Kelvin-Clapeyron model plays an integral role in analysing the mass transport at the liquid-vapour interface. The effect of the accommodation coefficient is often omitted in thin-film solutions [2,5,8,14,16,20,33,38,41], yet in the case of numerically modelling a thin-film meniscus, alters the results noticeably.

Most solutions use a value of unity for accommodation coefficient. As discussed in the literature review, this would suggest a system completely free of impurities. This would be very difficult to ensure experimentally.

Based on the mathematical model there is evaporative mass flux as the thin-film is traversed from adsorbed region to the bulk/intrinsic meniscus, and also considering the size scale of the problem, the effect of accommodation coefficient is observed over the length of the thin-film.

The ultimate goal of this parametric study is to couple results with experimental data, allowing for further insight into which value of accommodation coefficient is most accurate.

This parametric study is performed using the following input parameters:

**Table 5: Numerical model input values – varying accommodation coefficient ( $\gamma$ )**

<b>Input</b>	<b>Value</b>
<b>Applied Superheat</b>	0.01 K
<b>Vapour Temperature</b>	300 K
$\epsilon_1$	0.01% adsorbed thickness [m]
$\epsilon_3$	1e-003

The accommodation coefficient could not be tested in this case below a value of 0.3 as the applied slope perturbation became too sensitive to results and a solution could not be found within specified tolerances.

It is noted that in Figures 23-30, the direction of the arrow goes from  $\gamma = 1.0$  ending at the arrow head which represents  $\gamma = 0.3$ .

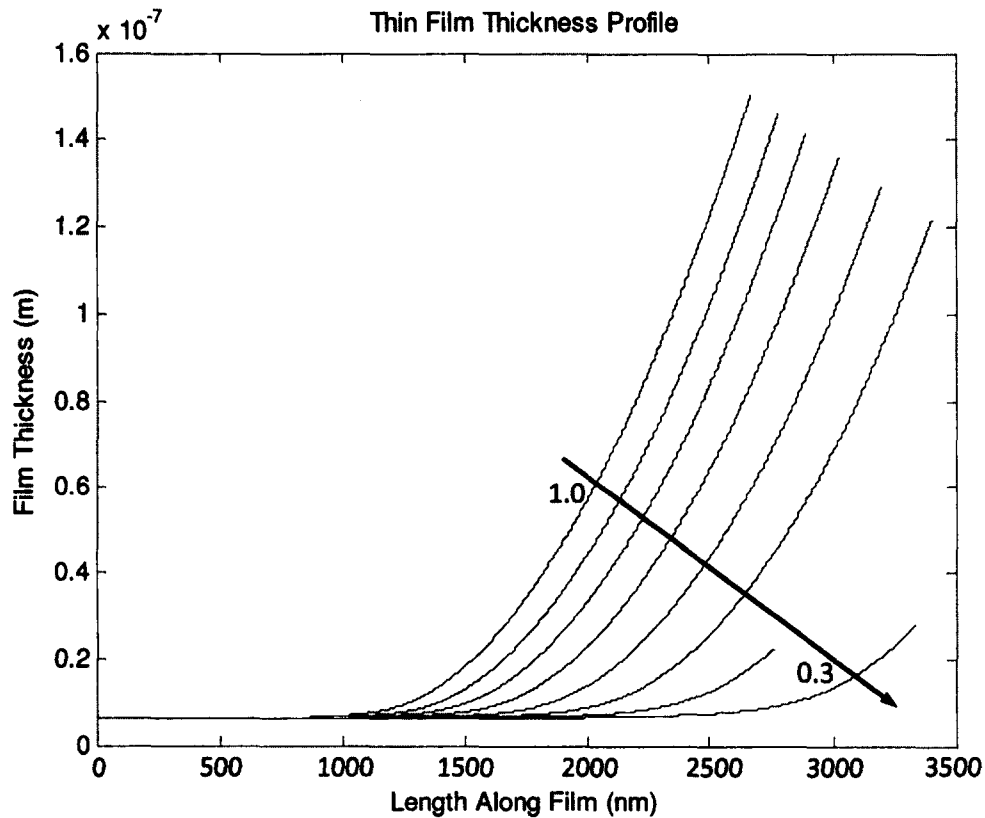


**Figure 23: Thin-film thickness profiles**

Figure 23 represents the film thickness for the various values of accommodation coefficient. It is clear that with a decreasing value of accommodation coefficient, the film thickness also decreases, and the adsorbed region is extended. The result is a modified thin-film interface shape. This result is expected as a smaller accommodation coefficient would suggest less evaporative mass flux, thus extending adsorbed region of the film.

The seemingly abrupt end of the thin-film profiles for  $\gamma=0.4$  and  $0.3$  is attributed to the constant curvature termination condition, in addition to the curvature profile. It will be shown later in Figure 28 at these lower values of accommodation coefficient, the overshoot is lost and thus the constant curvature condition is realised earlier.

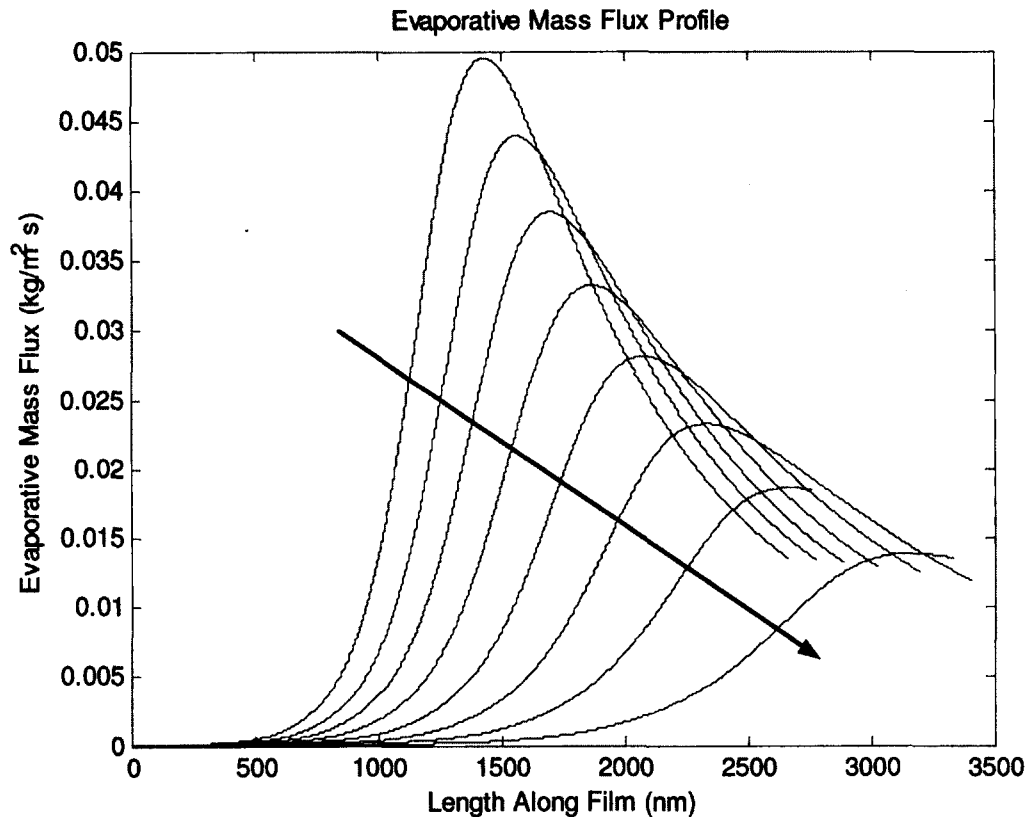


**Figure 24: Evaporative mass flux profiles**

Figure 24 agrees nicely with the effect of thin-film length and height. At the lower values of accommodation coefficient the evaporative mass flux decreases. Not only does the peak magnitude of mass flux decrease, but the location is shifted along the length of the film. This corresponds with the extension of the adsorbed region in the thin-film profiles, thus disjoining pressure decrease is retarded along the length of the film.

Observing the end of the evaporative mass flux profiles, it is clear in all of these cases that evaporative mass flux at the constant curvature condition is not zero. As mentioned earlier this deals with the use of the augmented Young-Laplace equation which entails

some residual mass flux towards the bulk/intrinsic meniscus. In addition, retarding the evaporation by implementing a lower value of accommodation coefficient leaves an increased residual mass flux in order to satisfy the mass flux balance used in derivation.

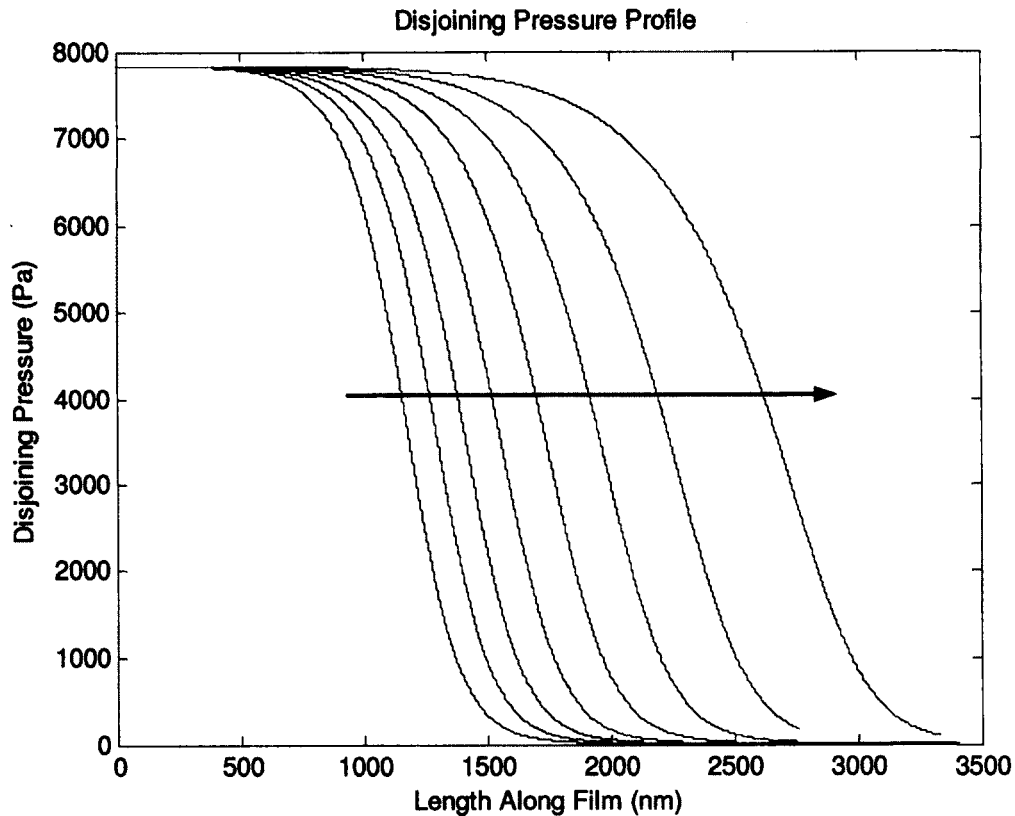


**Figure 25: Disjoining pressure profiles**

The disjoining pressure profiles also agree nicely with the previous two results. A decreasing accommodation coefficient delays the drop in disjoining pressure, thus delaying the peak of evaporative mass flux. The change in accommodation coefficient does not have a significant effect on the actual profile itself; it appears to shift the profile along the length of the thin-film. It does appear that with a decreasing accommodation coefficient that the spacing between profiles increases the lower the value becomes. This

is most likely a result of the way accommodation coefficient is implemented into the mathematical model.

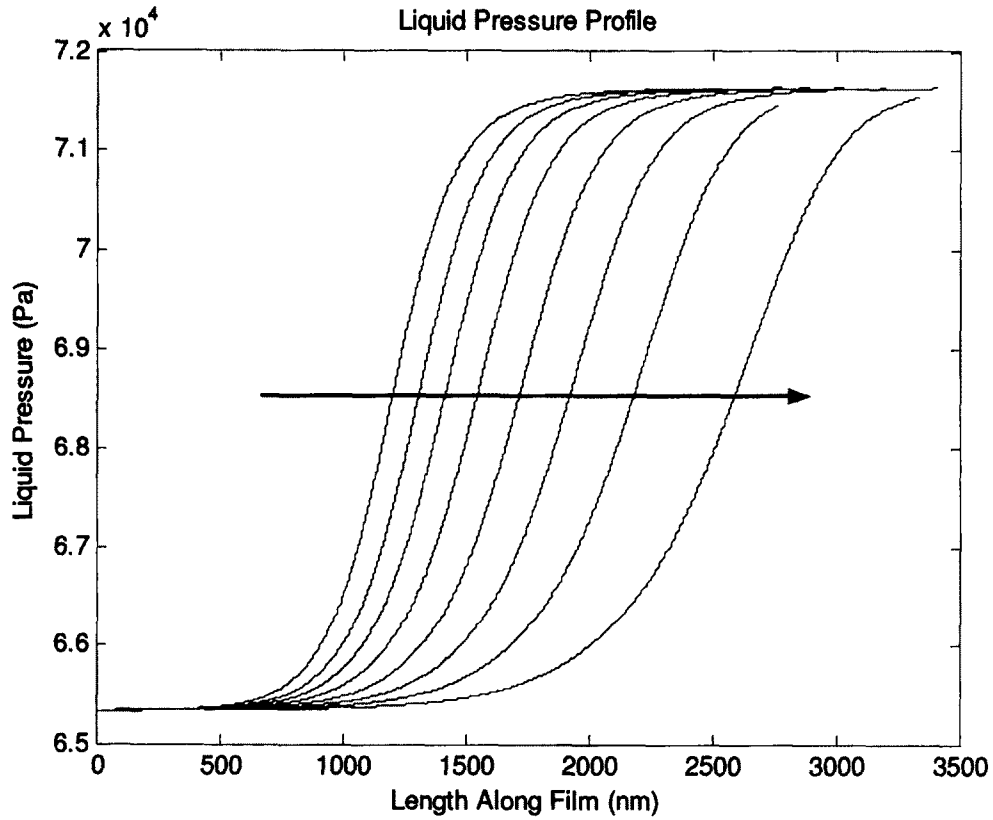


**Figure 26: Liquid pressure profiles**

The liquid pressure profile matches the disjoining pressure profile in an expected manner. The delayed decay of disjoining pressure with a decreasing accommodation coefficient causes a delayed increase of liquid pressure.

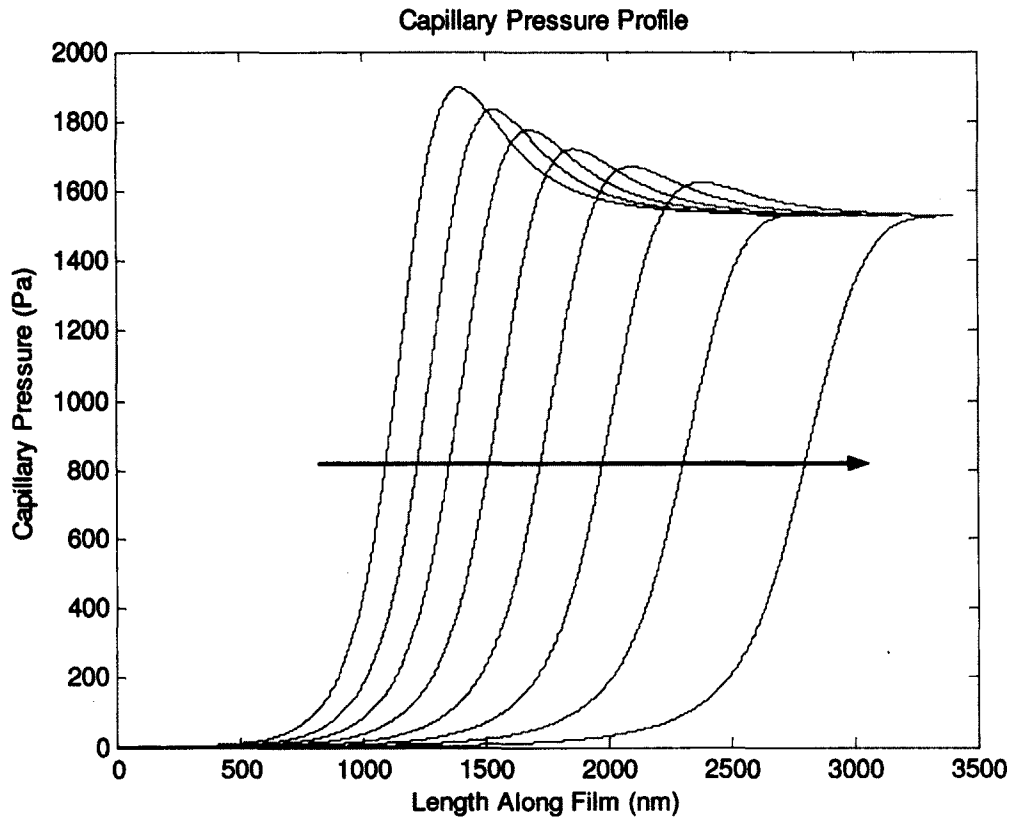


**Figure 27: Capillary pressure profiles**

The capillary pressure profile provides some very interesting characteristics. Along with the expected delay in increase along the film length, it is also noted that with decreasing accommodation coefficient, the overshoot diminishes. This lack of overshoot is directly related to the thin-film profile and the corresponding curvature. As the profile flattens at lower values of accommodation coefficients, the maximum curvature directly after the adsorbed region is not nearly as pronounced thus the overshoot is no longer seen.

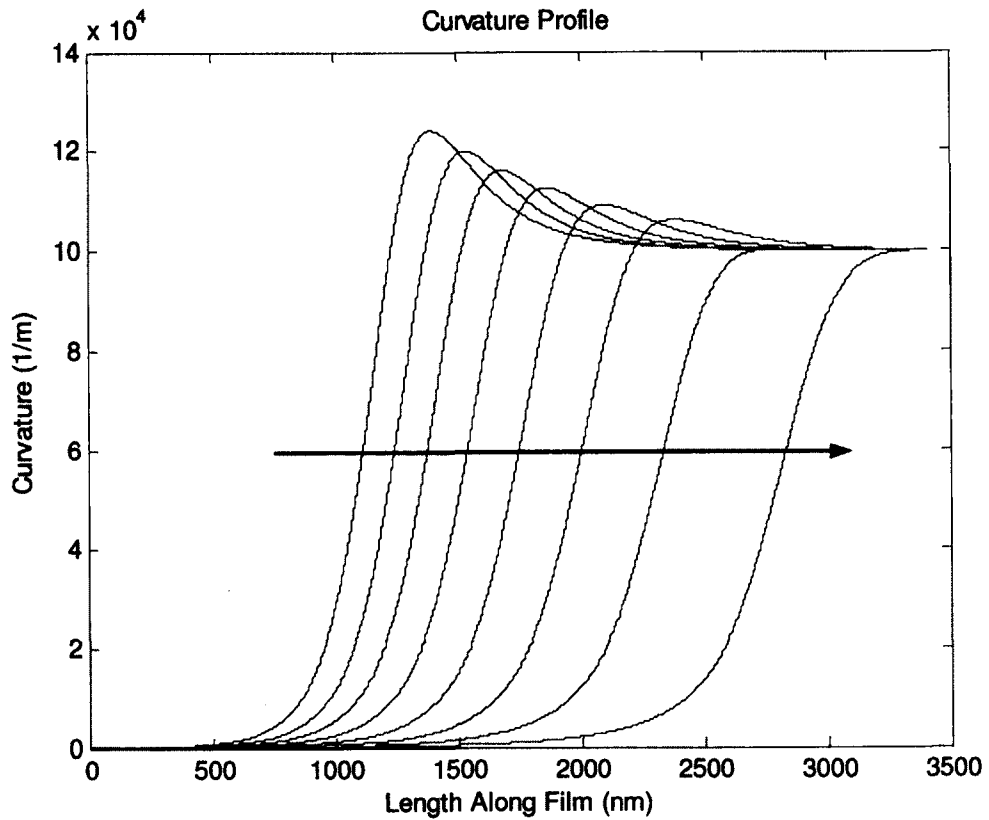


**Figure 28: Curvature profiles**

As mentioned above the curvature profile and the capillary pressure profile are qualitatively identical as capillary pressure is a function of curvature. Considering experimental works have suggested that the overshoot exists, it is likely that values between 0.5 -1.0 are more likely representative of experimental values, as the overshoot is still present [23, 40].

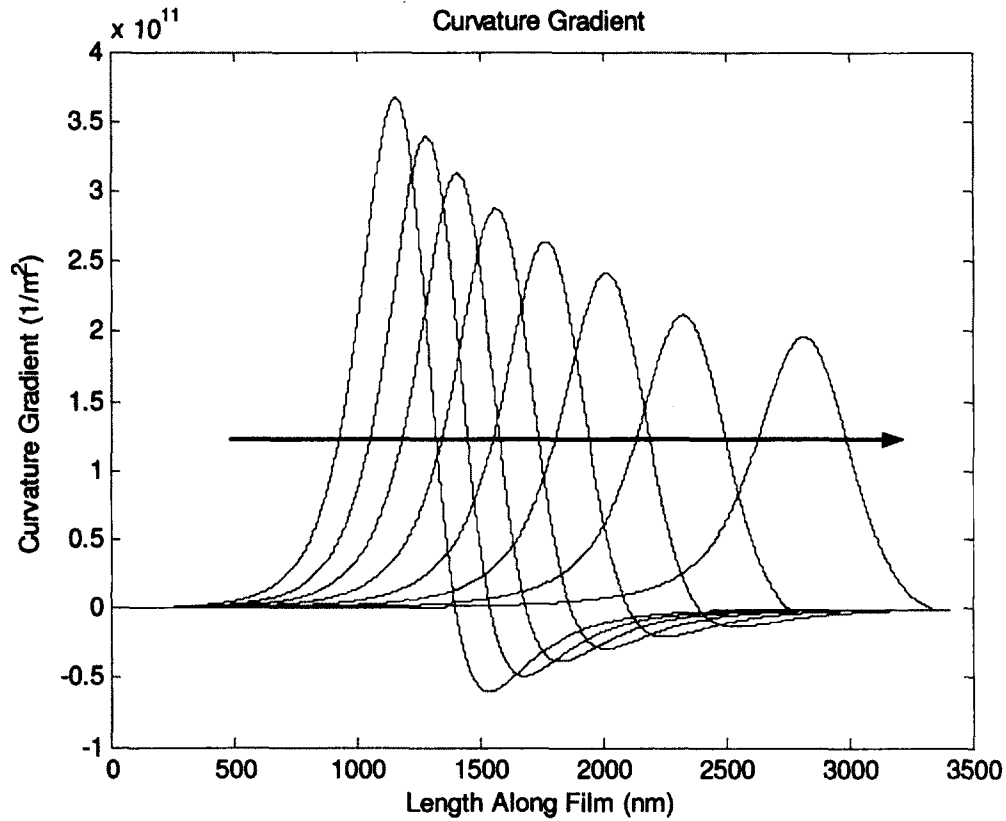


**Figure 29: Curvature gradients**

The curvature gradient provides further insight into the behaviour of capillary pressure and curvature profile mentioned above. With a decreasing accommodation coefficient, the initial transition from the adsorbed region is delayed, and the gradient is smaller in magnitude. At lower values of accommodation coefficient, it is seen that the minima diminishes.

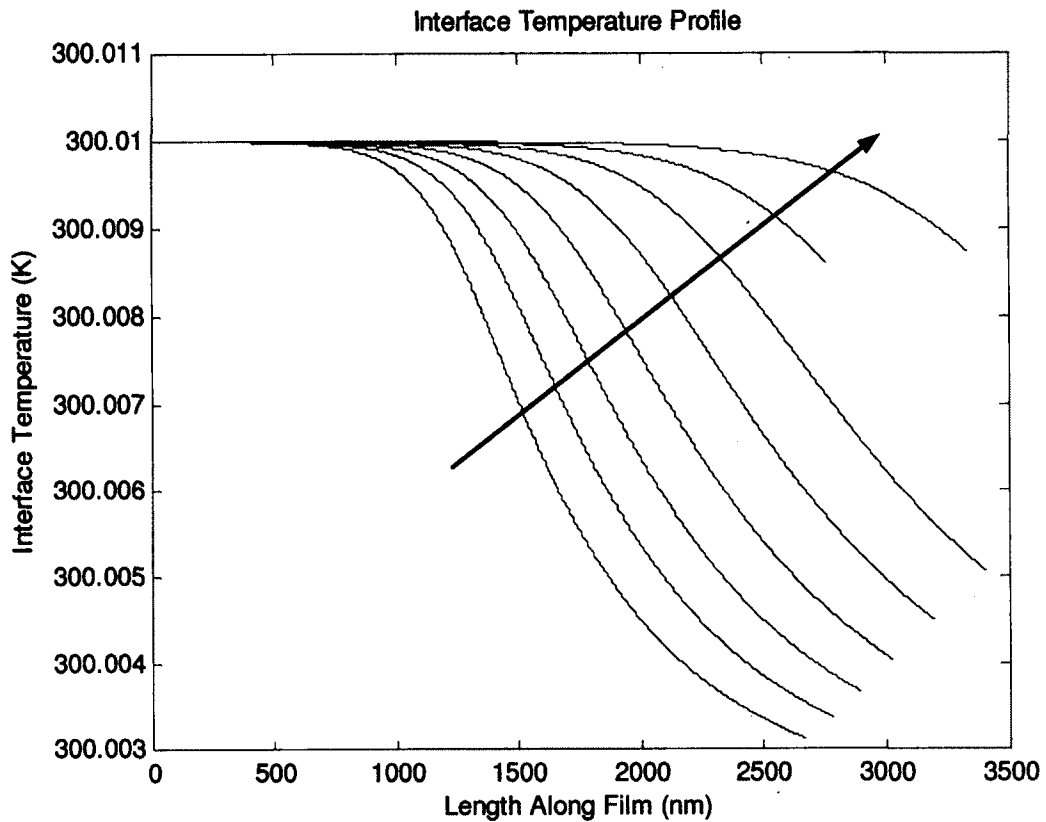


**Figure 30: Interfacial temperature profiles**

The interface temperature profile for varying accommodation coefficients follows a similar trend as would be expected. The majority of the temperature drop occurs just outside of the adsorbed region which is consistent with previous results [5]. It is clear with the extended adsorbed layer at lower accommodation coefficients, this temperature drop is retarded. As accommodation coefficient lowers, there is a much smaller region of film length before constant curvature for conductive losses to take place. This is evidenced by the significant decrease in evaporative mass flux.

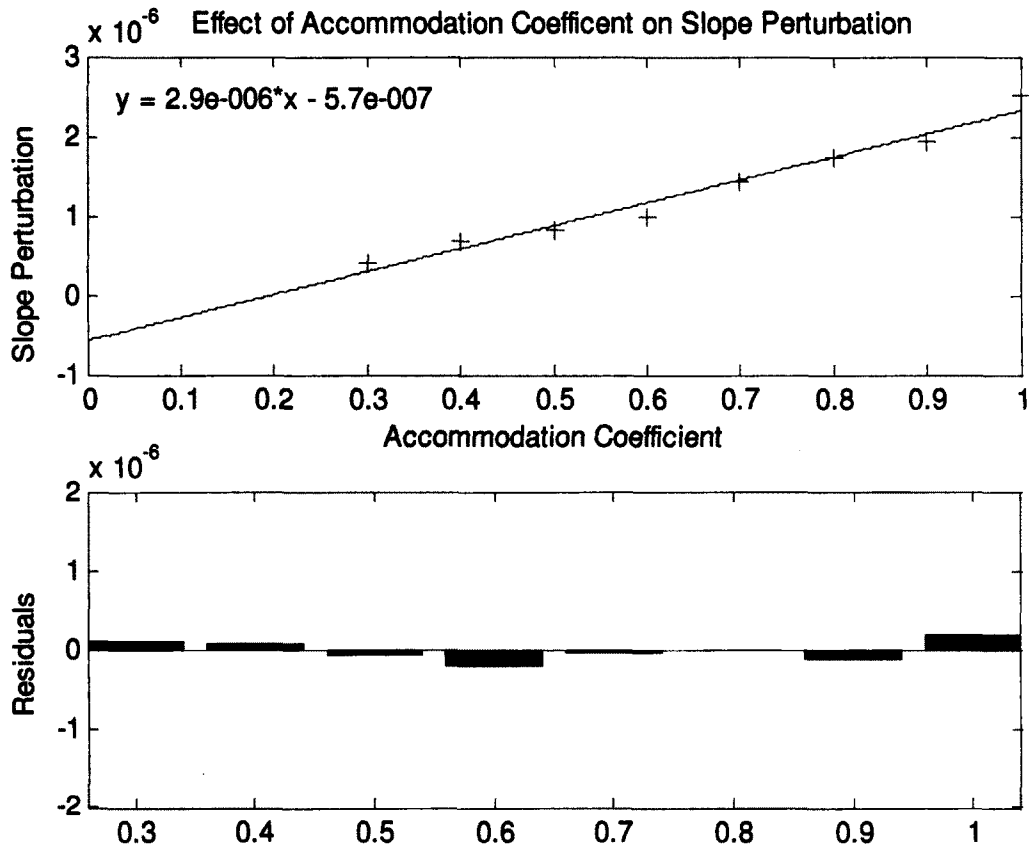


**Figure 31: Accommodation coefficient and the effect of the slope perturbation**

As mentioned earlier the third order ODE used in the thin-film solution exhibits extremely non-linear behaviour. As a result the solution is very sensitive to the applied perturbations. In particular the slope perturbation was found to be the most sensitive, as a result, that is the variable sought out in a far field solution, leaving  $\varepsilon_I$  fixed (at a certain percentage of the calculated adsorbed thickness) and  $\varepsilon_3$  fixed at  $1 \times 10^{-3}$ .

Figure 31 plots the slope perturbation providing a converged far field solution versus that of accommodation coefficient. As seen, the trend is approximately linear. A plot like this is extremely useful, as it allows for a narrow window to be selected as bounds within

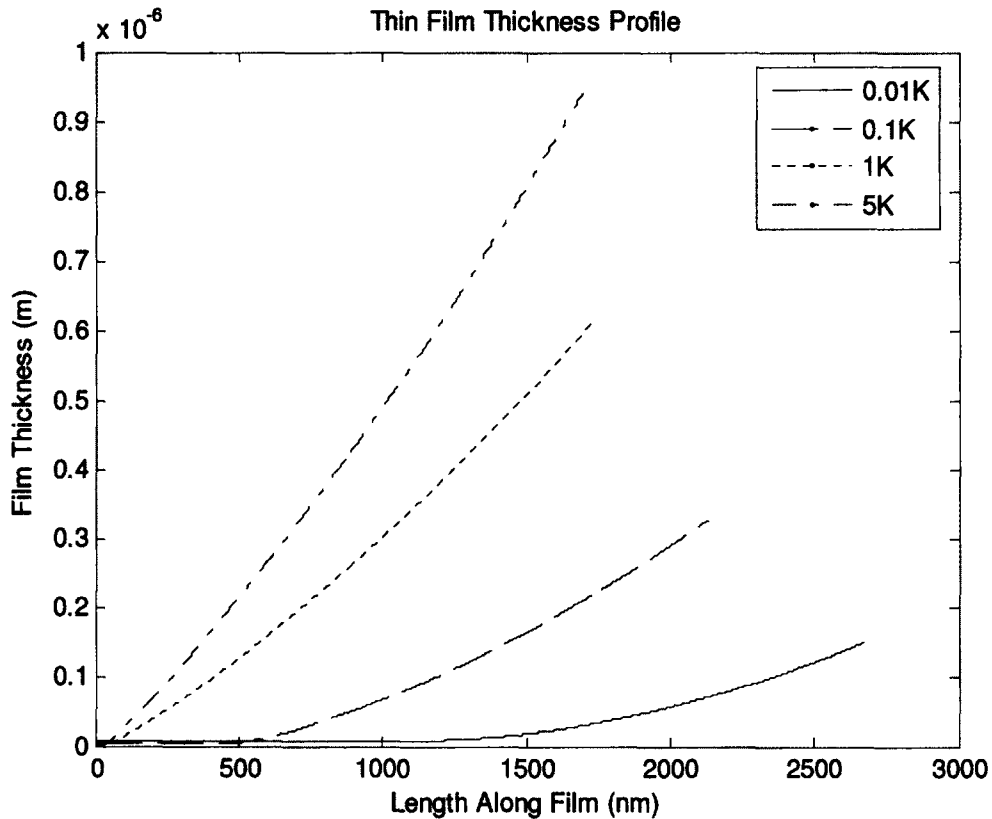
a bisection search. With the highly non-linear behaviour of the governing equation, incorrect selection of the bounds for a bisection search can lead to divergent results.

### 5.3 Effect of Varying Applied Superheat

Building off of the work of Polansky, a broadened view into the effect of applied superheat is observed. This parametric study covers a much wider range of superheat values. The updated numerical model has the ability to generate thin-film solutions at larger applied superheats, in which much less publications have included [2]. The applied superheats applied will be 0.01 K, 0.1 K, 1 K and 5 K. The higher values are more indicative of experimental conditions. As in the above solutions, the slope perturbation is solved for, as to satisfy the far field curvature condition. Details of the initial conditions used are seen below in Table 6.

**Table 6: Numerical model input values – different superheats**

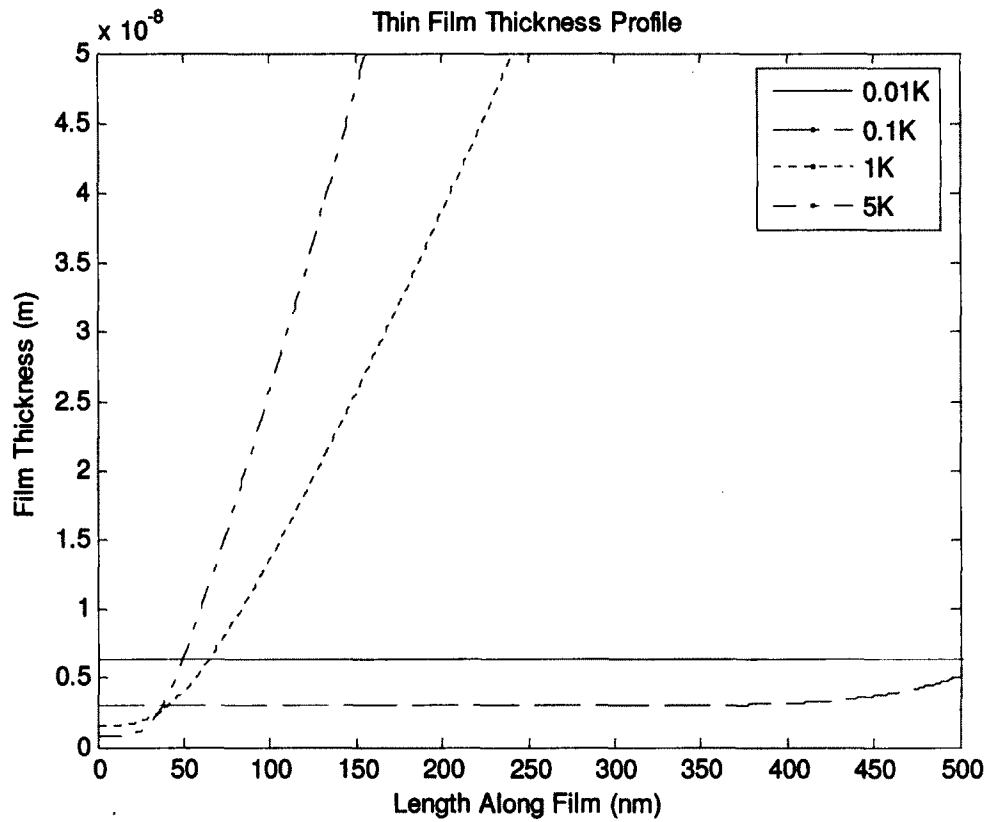
Input	Value
<b>Applied Superheat</b>	0.01 K, 0.1 K, 1 K, 5 K
<b>Vapour Temperature</b>	300 K
$\epsilon_{1@0.01K}$	0.01% Adsorbed Thickness
$\epsilon_{1@0.1K}$	0.01% Adsorbed Thickness
$\epsilon_{1@1K}$	1% Adsorbed Thickness
$\epsilon_{1@5K}$	1% Adsorbed Thickness
$\epsilon_3$	1e-003



**Figure 32: Thin-film thickness profiles**

When comparing thin-film characteristics at such a range of superheats, the wide range in magnitudes can make comparison rather difficult. Figure 32 above shows the thin-film profiles for the range of superheats. From this figure the major trends can be identified. With an increasing superheat, the thin-film length shortens, but as a result of the shortened length the thickness increases significantly. This behaviour is documented in several other works [2,5,8,16,38]. At 5 K a peak thickness of almost 1  $\mu\text{m}$  is observed, where as 0.01 K provides a peak thickness of approximately 0.16  $\mu\text{m}$ . It is also clear from Figure 32 that the transition from the adsorbed region is much more abrupt at higher

superheats. This makes the applied slope perturbation much more difficult to define when obtaining a far field solution.



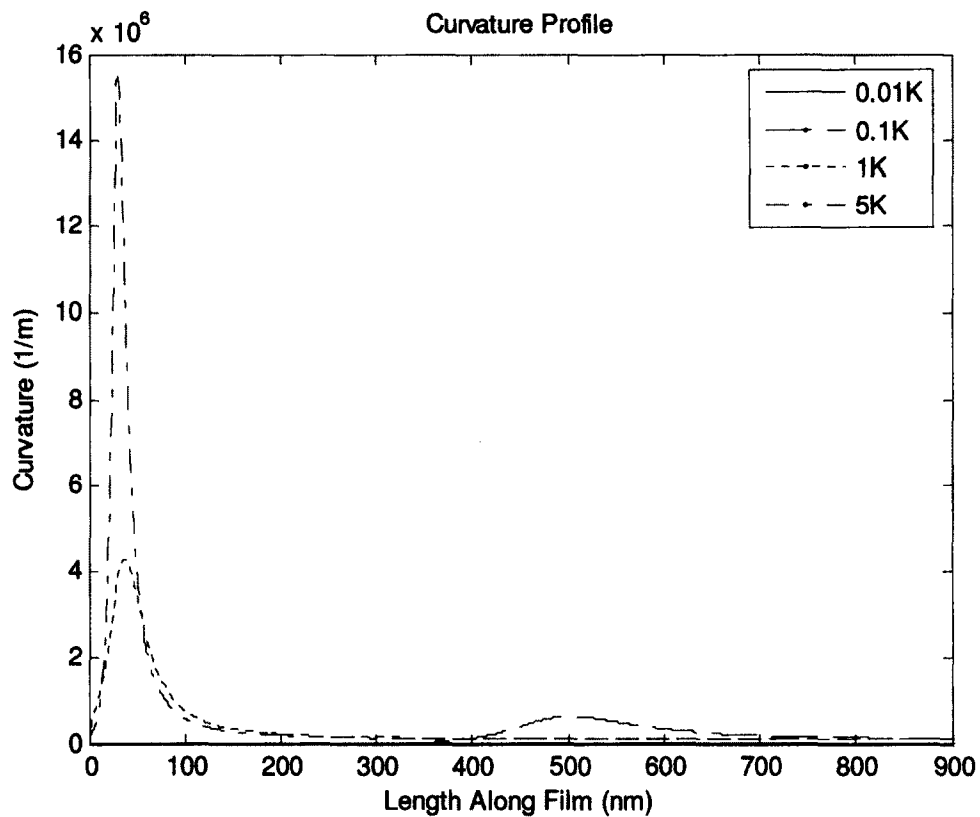
**Figure 33: Enlarged view of thin-film thickness profiles**

Figure 33 provides a close-up view along the length of the thin-film from Figure 32. This is to demonstrate in further detail two of the key trends observed with an increasing superheat. As mentioned above, with an increased superheat, the transition from the adsorbed region is much less subtle. This is clearly evident in the 1 K and 5 K superheat profiles above.

Another trend to be observed is the decrease in adsorbed thickness of the thin-film with an increase in superheat. This is expected as it is the nature of the equation used in

calculating the initial adsorbed thickness of the adsorbed region. This can be seen in Equation 55. This provides insight as to the variance of the thickness perturbation used at the higher superheats. With a lower initial adsorbed thickness at higher superheats, an increased thickness perturbation must be applied in order to find a far field solution.

Other trends can be observed with varying superheat, however with such a drastic change in magnitudes it is difficult to provide a meaningful graphical comparison. For instance, below is a graph of the curvature profiles with varying superheat.



**Figure 34: Curvature profiles**

As seen in Figure 34, the magnitudes of the curvature overshoot increases significantly with an increasing superheat. The 0.01 K profile appears nearly linear, but observing

Figure 17, it is clear that overshoot is present. The location of the overshoot also varies with the applied superheat. With lower superheat values, this overshoot effect is retarded significantly. Similar trends have been found in both numerical and some experimental works [2,23,38]. In addition, observing how aggressive the change in thin-film thickness is from Figure 33, it is clear the curvature is greatly increased in that localised region and this overshoot becomes even more pronounced.

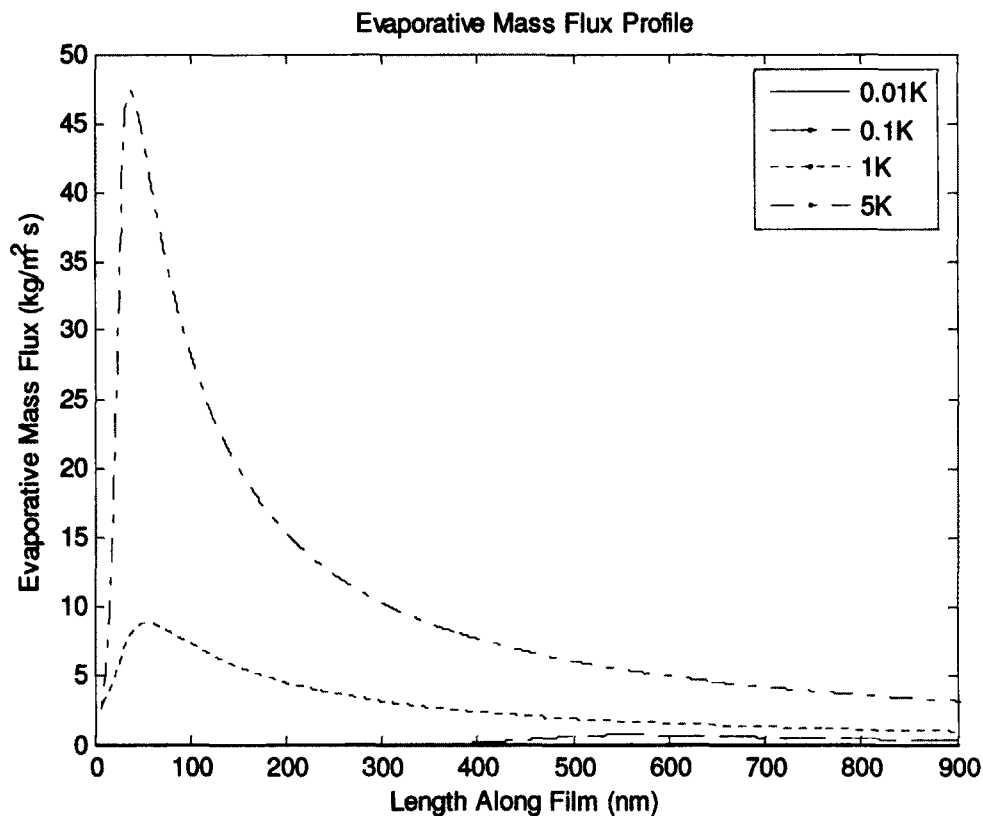


**Figure 35: Evaporative mass flux profiles**

Figure 35 displays the effect of the applied superheats on the evaporative mass flux profile. As anticipated, the evaporative mass flux increases with applied superheat. Dealing with such a range of superheats the 1 K and 5 K cases seem dominant as their magnitudes are much greater when compared to the smaller superheats; however the

qualitative trend is similar. With increasing superheat, the peak evaporative mass flux is seen nearer to the adsorbed region, but is still consistent with the point at which disjoining pressure and liquid pressure exchange dominance. This exchange happens almost immediately after leaving the adsorbed region as the curvature aggressively increases.

## 5.4 Unified Solution

In what literature exists on modelling thin-film menisci, little effort is applied in an attempt to model a unified solution to half channel width in which the variable curvature augmented Young-Laplace solution is appropriately joined with the constant curvature Young-Laplace solution. Theoretically, the point at which the models should be unified is when the thin-film model reaches its point of constant curvature thus signifying the beginning of the intrinsic/bulk meniscus.

Du et al. [20] attempted to provide a unified solution as mentioned above. Du claimed to further define the boundary condition describing the end of the transition region and the beginning of the bulk region. Du defines this boundary condition when the following equation is satisfied:

$$R_c = \frac{R_\infty}{(1 + \delta_\infty^2)^{0.5}} + \delta_\infty \quad (72)$$

Where  $R_c$  is the half-width of the channel,  $R_\infty$ ,  $\delta_\infty$ ,  $\delta'_\infty$  are the radius, thickness and first-order derivative of the asymptotic intrinsic meniscus, where the radius of the film can be treated as a constant [20].

In attempting to implement this boundary condition, a fundamental inaccuracy is recognized, which deals with the  $R_\infty$  variable. This inaccuracy is found in defining the radius of the asymptotic intrinsic meniscus, and subsequently the variables dependent on this value. Observing Figure 36 below a few comments can be made.

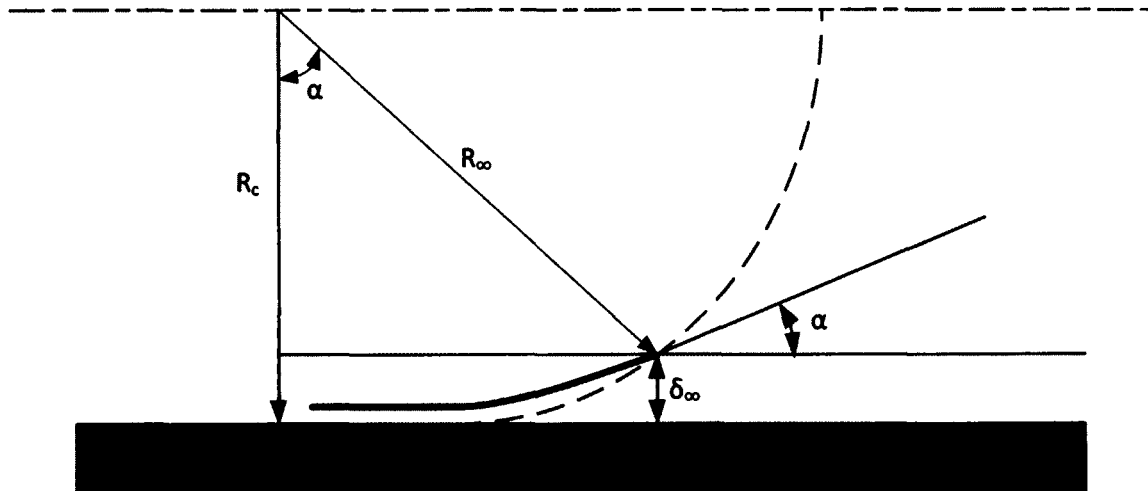


**Figure 36: Schematic geometry of boundary conditions [adapted from 20]**

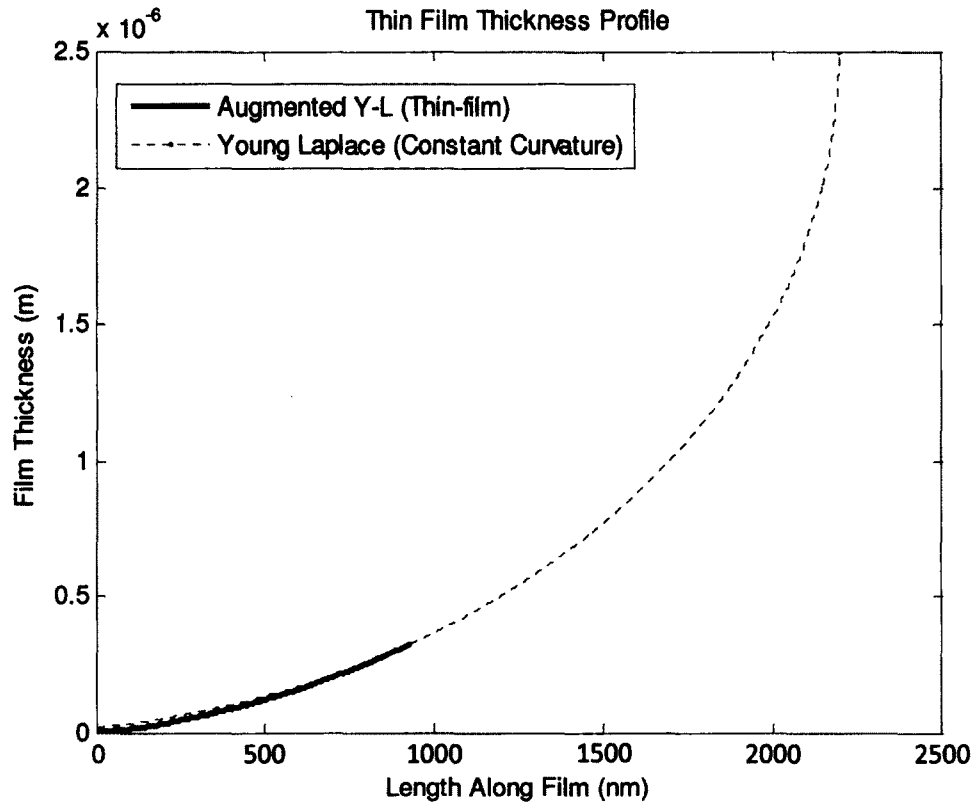
Using the method of asymptotically matching a radius,  $Du$  allows the meniscus radius to change while in the intrinsic region while ensuring that the center of the meniscus is on the axis of that change [20]. This disagrees with that of the Young-Laplace model which invokes a constant radius in the intrinsic region.

This can be avoided through the idea of having a Young-Laplace solution with constant curvature match up with the augmented Young-Laplace solution (or thin-film solution) at the point the constant curvature is achieved. However, when forcing the Young-Laplace solution through the point of constant curvature on the thin-film solution, the Young-Laplace solution must remain valid for the same channel width. This is done by shifting the Young-Laplace solution along the line of symmetry of the channel such that it will pass through the point of constant curvature of the thin-film solution. This ensures that at this transition point the curvatures are of equal value and a unified solution can be generated allowing the meniscus to be accurately modeled from the adsorbed region to the bulk region at half channel width.

Results for this will be shown below, with Table 7 providing the numerical input values. An octane solution is used to contrast Du et al. [20], which implements the new boundary condition model to Wang et al [5].

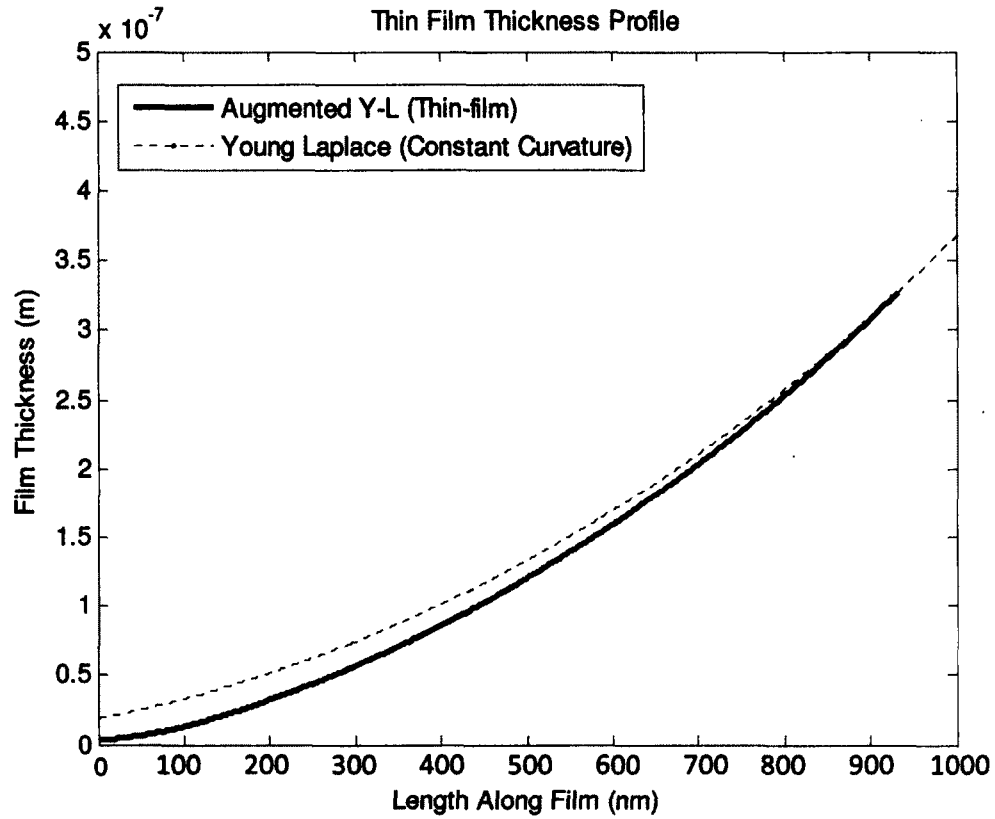
**Table 7: Numerical model input values – unified solution**

<b>Input</b>	<b>Value</b>
<b>Applied Superheat</b>	<b>1 K</b>
<b>Vapour Temperature</b>	<b>300 K</b>
<b><math>\epsilon_1</math> – Thickness Perturbation (<math>\delta_o</math>)</b>	<b>1.69e-009</b>
<b><math>\epsilon_3</math> – Perturbation applied to <math>\delta''</math></b>	<b>1e-003</b>



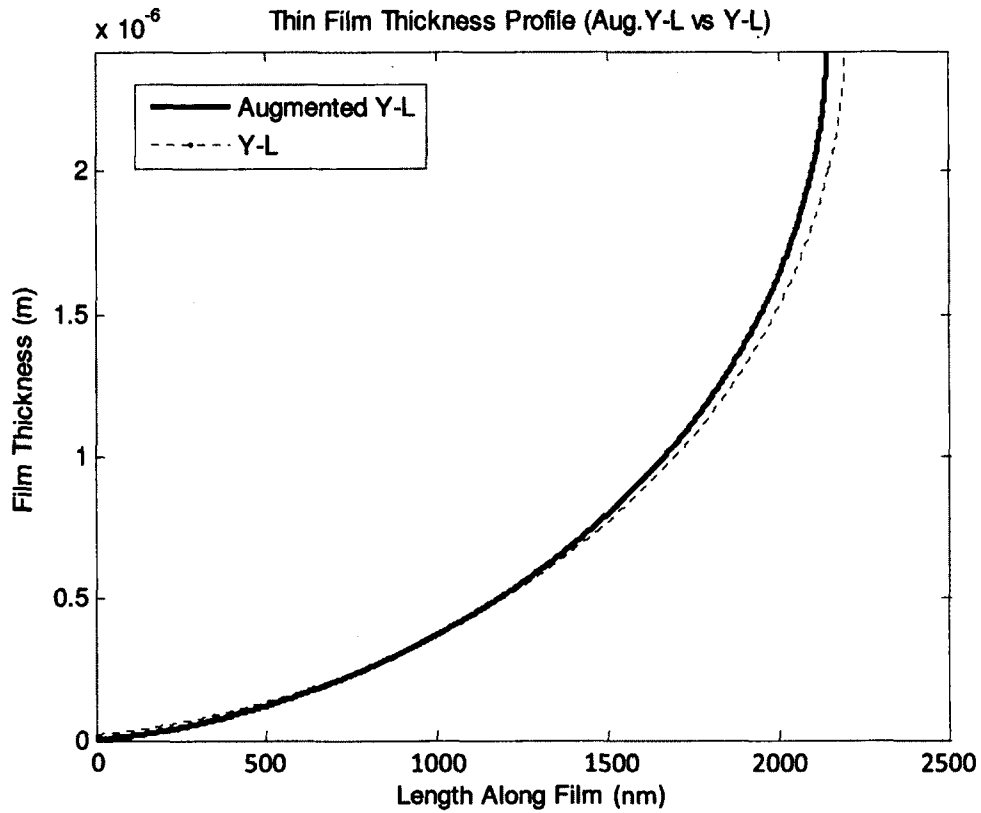
**Figure 37: Unified thin-film thickness profile**

Figure 37 provides a visual of a unified solution for Octane at 1 K applied superheat. The bold line models the augmented Young-Laplace thin-film solution, and is superimposed on the dashed Young-Laplace solution. The Young-Laplace solution is modelled such that it passes through the point at which constant curvature is reached from the thin-film solution. As seen, at all points to the left of this constant curvature condition, there is a slight deviation between the two solutions as expected.



**Figure 38: Enlarged thin-film thickness profile**

Figure 38 provides an enlarged view as to more clearly see the deviation and overlap at the point of constant curvature. It is important to note that the Young-Laplace solution is not valid in the transition region, and is shown only for qualitative comparison.



**Figure 39: Thin-film thickness to channel radius - augmented Y-L solution vs Y-L solution**

Figure 39 plots the film thickness to half channel width of both the Young-Laplace solution as well as the augmented Young-Laplace solution. Although it is clear that the augmented Young-Laplace equation is to be used only in the thin-film region and the Young-Laplace equation be used only in the bulk/intrinsic region, this comparison allows for a qualitative inspection of how the augmented Young-Laplace equation nearly tends to the Young-Laplace equation after achieving constant curvature.

# Chapter 6

## Conclusions and Recommendations

### 6.1 Conclusions

Understanding the characteristics of an evaporating thin-film meniscus is essential to the study of high performance phase-change heat transfer devices. The objective of this research was to build upon an existing model and extend the capabilities to gain further insight into the physical characteristics of a thin-film and its evaporative properties. In this research a non-polar fluid is analysed and the associated meniscus generated in a narrow channel.

The mathematical model developed employs the use of kinetic theory of gases and continuum mechanics. Continuity, momentum, energy equations and the Kelvin-Clapeyron model are used in developing a third order ODE which governs the evaporating thin-film meniscus. The model is designed to take into account varying thermophysical properties such as to accurately model cases of high superheats.

The ODE is solved numerically using a Runge-Kutta technique which is coded in MATLAB. The problem is an initial value problem and as such requires input of the film thickness and the associated derivatives. Associated parameters and boundary conditions can be altered by the user such as channel width, working fluid, applied superheat, liquid and vapour temperatures and accommodation coefficient.

A summary of the fundamental findings are as follows:

- The numerical solution is very sensitive to the initial conditions and the applied perturbations. In particular extreme sensitivity is found with the applied value of  $\delta$  and its associated perturbation  $\varepsilon_2$ . In addition, applied perturbations must be small enough such as to not shift the origin of the coordinate system too far into the thin-film region. Using too large of perturbations can result in omission of key attributes near the adsorbed region.
- Solution sets were generated to ensure the values obtained were within reasonable accuracy to published values. The numerical simulation proved to provide reasonable quantitative comparison to both third and fourth order models from literature.
- Traversing the thin-film from adsorbed region to bulk region, almost immediately after leaving the adsorbed region there is a complete and rapid decay of disjoining pressure effects. As such there is a corresponding rise in liquid pressure. These large pressure differences correspond with the length at which evaporative mass flux is at its peak value. This confirms that evaporative effects are more pronounced in the thin-film region, as well as disjoining pressure is dominant near the adsorbed region and liquid pressure dominant towards the bulk region.
- Accommodation coefficient has a pronounced effect on thin-film geometry and associated characteristics. Decreasing accommodation coefficient shallows the thin-film profile. This shallowing resulted in retardation of the decline in disjoining pressure. This corresponded in delaying the increase in liquid pressure and shifting the peak evaporative mass flux along the length of the film. The

magnitude in evaporative mass flux also decreased with decreasing accommodation coefficient. Curvature overshoot was also observed to diminish with decreasing accommodation coefficient.

- The effect of applied superheats varying from 0.01 K – 5 K steepened the thin-film profile and decreased the length as superheat increased. This led to a large curvature overshoot and increased evaporative mass flux as superheat increased. As a result of the thin-film geometry at larger superheats, the perturbation sensitivity increases. As a result  $\varepsilon_1$  had to be increased in order to seek an appropriate  $\varepsilon_2$ .
- The thin-film profile can be continued to model up to half channel width. As such a unified solution could be modelled matching the Young-Laplace solution with that of the augmented Young-Laplace solution at the point when curvature becomes constant. It is shown that after this point there is a slight deviation in profiles between the augmented Young-Laplace and the Young-Laplace solution in the bulk region. This difference in profile is due to a small residual evaporative mass flux found in the augmented Young-Laplace solution.

## 6.2 Recommendations

With the results presented, there is future work and further adjustments, which can be made to the model. Firstly and perhaps the most daunting of recommendations is the development of experimental procedure such that validation of results obtained numerically is possible. This would allow for significant advancement in the research on many levels, as one could confirm the value of accommodation coefficient which most

accurately models a physical solution in addition to further verifying values for slip or applied perturbations. Considering the minute size scale of the analysis, this is an extremely difficult and sensitive task. With ever improving technology an optimistic outlook that meaningful experimental values will be able to be recorded in the relative future.

The current model could be expanded upon with the addition of polar liquids. This changes the definition of disjoining pressure and would allow for a variety of fluids to be modelled such as ammonia or water. However without first providing some sort of experimental validation this is not a priority.

Finally, the mathematical model can be extrapolated upon. Currently the physics of the problem is simplified such as to only capture 1-D flow characteristics. A more in-depth model can be generated to analyze the problem as either two or three dimensional. Although mathematically taxing, this would provide greater insight into the flow characteristics within the thin-film and provide a more accurate representation. Coupled with experimental data, one could confidently predict the behaviour of an evaporating thin-film and ultimately realise the inherent instabilities within phase change heat transfer devices.

## References

- [1] S. DasGupta, I. Y. Kim, and P. C. Wayner Jr., "Use of the Kelvin-Clapeyron equation to model an evaporating curved micro-film," *Journal of Heat Transfer*, vol. 116, pp. 1007-1015, 1994.
- [2] Jun-Jie Zhao, Yuan-Yuan Duan, Xiao-Dong Wang Bu-Xuan Wang, "Effects of superheat and temperature-dependent thermophysical properties on evaporating thin liquid films in microchannels" *International Journal of Heat and Mass Transfer*, vol. 54, pp. 1259-1267, 2011.
- [3] P. Cheng, J. Dong, S.M. Thompson, H.B. Ma, "Heat transfer in bulk and thin-film fluid regions of rectangular microgroove," *Journal of Thermophysics and Heat Transfer*, vol. 26, no.1, pp. 108-114, 2012.
- [4] J. Polansky, *Numerical Model of an Evaporating Thin Film Meniscus*, Carleton University Press, Ottawa, Ontario, Canada, 2011.
- [5] H. Wang, S. V. Garimella, and J. Y. Murthy, "Characteristics of an evaporating thin film in a microchannel," *International Journal of Heat and Mass Transfer*, vol. 50, pp. 3933 - 3942, 2007.
- [6] P. C. Wayner Jr., "Intermolecular forces in phase-change heat transfer: 1998 Kern award review," *AIChE Journal*, vol. 45, pp. 2055-2068, 1999.
- [7] C. Buffone, K. Sefiane, and J. R. E. Christy, "Experimental investigation of the hydrodynamics and stability of an evaporating wetting film placed in a temperature gradient," *Applied Thermal Engineering*, vol. 24, pp. 1157-1170, 2004.
- [8] S. K. Wee, K. D. Kihm, and K. P. Hallinan, "Effects of the liquid polarity and the wall slip on the heat and mass transport characteristics of the micro-scale evaporating transition film" *International Journal of Heat and Mass Transfer*, vol. 48, pp. 265-278, 2005.
- [9] K. Park, K. J. Noh, and K. S. Lee, "Transport phenomena in the thin-film region of a micro-channel," *International Journal of Heat and Mass Transfer*, vol. 46, pp. 2381-2388, 2003.
- [10] K. Stephan, "Influence of dispersion forces on phase equilibria between thin liquid films and their vapour," *International Journal of Heat and Mass Transfer*, vol. 45, pp. 4715 - 4725, 2002.

- [11] S. DasGupta, J. A. Schonberg, I. Y. Kim, and P. C. Wayner Jr., "Use of the augmented Young-Laplace equation to model equilibrium and evaporating extended meniscus," *Journal of Colloid and Interface Science*, vol. 157, pp. 332-342, 1993.
- [12] L.W. Swanson, G.C. Herdt, "Model of the evaporating meniscus in a capillary tube," *ASME Journal of Heat Transfer*, vol. 114, pp. 434-441, 1992.
- [13] K.H. Do, S.J. Kim, S.V. Garimella, "A mathematical model for analyzing the thermal characteristics of a flat micro heat pipe with a grooved wick," *International Journal of Heat and Mass Transfer*, vol. 51, pp. 4637-4650, 2008.
- [14] H.Wang, S. V. Garimella, and J. Y. Murthy, "An analytical solution for the total heat transfer in the thin-film region of an evaporating meniscus," *International Journal of Heat and Mass Transfer*, vol. 51, pp. 6317- 6322, 2008.
- [15] B. Derjaguin, N. Churaev, and V. Muller, *Surface Forces*. New York: Consultants Bureau, 1987.
- [16] W. Qu, T. Ma, J. Miao, and J. Wang, "Effects of radius and heat transfer on the profile of evaporating thin liquid film and meniscus in capillary tubes," *International Journal of Heat and Mass Transfer*, vol. 45, pp. 1879-1887, 2002.
- [17] K. Park, K.S. Lee, "Flow and heat transfer characteristics of the evaporating extended meniscus in a micro-capillary channel," *International Journal of Heat and Mass Transfer*, vol. 46, pp. 4587-4594, 2003.
- [18] L. Lin, A. Faghri, "Heat transfer in micro region of a rotating miniature heat pipe," *International Journal of Heat and Mass Transfer*, vol. 42, pp. 1363-1369, 1999.
- [19] V.P. Carey, *Liquid-Vapour Phase-Change Phenomena*, Taylor & Francis, 2<sup>nd</sup> ed., 2007.
- [20] S-Y. Du and Y-H. Zhao, "New boundary conditions for the evaporating thin-film model in a rectangular micro channel," *International Journal of Heat and Mass Transfer*, vol. 54, pp. 3694 - 3701, 2011.
- [21] P. C. Wayner Jr., Y. Kao, and L. LaCroix, "The interline heat-transfer coefficient of an evaporating wetting film," *International Journal of Heat and Mass Transfer*, vol. 19, pp. 487- 492, 1976.
- [22] R.W. Schrage, *A Theoretical Study of Interphase Mass Transfer*, Columbia University Press, 1953.

- [23] S.S. Panchamgam, A. Chatterjee, J. L. Plawsky, and P. C. Wayner Jr., "Comprehensive experimental and theoretical study of fluid flow and heat transfer in a microscopic evaporating meniscus in a miniature heat exchanger," *International Journal of Heat and Mass Transfer*, vol. 51, pp. 5368-5379, 2008.
- [24] J. A. Schonberg, S. DasGupta, and P. C. Wayner Jr., "An augmented Young-Laplace model of an evaporating meniscus in a microchannel with high heat flux," *Experimental Thermal and Fluid Science*, vol. 10, pp. 163-170, 2011.
- [25] P. C. Wayner Jr., "The effect of interfacial mass transport on flow in thin liquid films," *Colloids and Surfaces*, vol. 52, pp. 71-84, 1991.
- [26] R. Marek, J. Straub, "Analysis of the evaporation coefficient and the condensation coefficient of water," *International Journal of Heat and Mass Transfer*, vol.44, pp. 39-53, 2001.
- [27] A. F. Mills, "The condensation of steam at low pressures", Technical Report on NSF GP-2250, series no. 6, issue no. 39, Space Sciences Laboratory, University of California at Berkeley, 1965.
- [28] S. C. Maroo and J. N. Chung, "Heat transfer characteristics and pressure variation in a nanoscale evaporating meniscus," *International Journal of Heat and Mass Transfer*, vol. 53, pp. 3335- 3345, 2010.
- [29] R. Ranjan, J.Y. Murthy, and S. V. Garimella, "A microscale model for thin-film evaporating in capillary wick structures," *International Journal of Heat and Mass Transfer*, vol. 54, pp. 169-179, 2011.
- [30] R. Ranjan, J. Y. Murthy, S. V. Garimella, and U. Vadakkan, "A numerical model for transport in at heat pipes considering wick microstructure effects," *International Journal of Heat and Mass Transfer*, vol. 54, pp. 153-168, 2011.
- [31] M. Potash Jr., P.C. Wayner Jr., "Evaporative from a two dimensional extended meniscus," *International Journal of Heat and Mass Transfer* vol.15, pp. 1851-1863, 1972.
- [32] S. Moosman, G.M. Homsy, "Evaporating meniscus of wetting fluids", *Journal of Colloid and Interface Science* vol. 73, pp.212-223, 1980.
- [33] S-Y. Du and Y-H. Zhao, "Numerical study of conjugated heat transfer in evaporating thin-films near the contact line," *International Journal of Heat and Mass Transfer*, vol.55, pp. 61-68, 2012.
- [34] Z.H. Kou and M.L. Bai, "Effects of wall slip and temperature jump on heat transfer characteristics of an evaporating thin film," *International Communications in Heat and Mass Transfer*, vol.38, pp. 874-878, 2011.

- [35] F.M. White, *Viscous Fluid Flow*, McGraw Hill, 3<sup>rd</sup> ed., 2006.
- [36] P.C. Stephan, C.A. Busse, "Analysis of the heat transfer coefficient of grooved heat pipe evaporator walls," *International Journal of Heat and Mass Transfer*, vol. 35, pp.383-391, 1992.
- [37] J.R. Dormand and P.J. Prince, "A family of embedded Runge-Kutta formulae," *Journal of Computational and Applied Mathematics*, vol.6, pp. 19-26, 1980.
- [38] S. S. Panchamgam, J. L. Plawsky, and P. C. Wayner Jr., "Microscale heat transfer in an evaporating moving extended meniscus," *Experimental Thermal and Fluid Science*, vol. 30, pp. 745-754, 2006.
- [39] V. Aitken and N. Holtz, "Numerical Integration Formulae," Carleton University, Ottawa, Ontario. November 5, 2007.
- [40] R. Argade, S. Ghosh, S. De, S. DasGupta, "Experimental investigation of evaporation and condensation in the contact line region of a thin liquid film experiencing small thermal perturbations," *Langmuir* vol.23, pp. 1234–1241, 2007.
- [41] K.P. Hallinan, H.C. Chebaro, S.J. Kim, W.S. Chang, "Evaporation from an extended meniscus for nonisothermal interfacial conditions," *Journal of Thermophysics and Heat Transfer* vol.8, pp.709–716, 1994.

# Appendix A – Thin-film Model

Considering this research is an extension of the M.A.Sc. thesis produced by Polansky [4], the basis of the mathematical model has not been altered. As such, the reader is directed to [4] for a comprehensive outline of the mathematical details.

A slightly suppressed version is supplied here.

The below table identifies all of the terms used as grouping of terms within the ODE.

**Table 8: Variables used in ODE simplification**

Variable	Term
$C_1$	$\sigma' \frac{dx}{dP_1} - \delta$
$u_s$	$\frac{\beta}{\mu} \left( \frac{dP_1}{dx} \delta - \sigma' \right)$
$C_4$	$-\frac{\delta^3}{3} + \delta^2 \beta$

---

 $\chi$ 

$$\delta' \left[ k_l \delta^2 (T_w^{5/2} - T_w T_{lv}^{3/2}) - 3AV_l \eta \right]$$

  
 $\theta$ 

$$\frac{\alpha^{3/2}}{\sigma} \left( \frac{3A}{\delta^4} \delta' - \frac{\nu k_l}{C_4 h_{fb}} \int_0^x \frac{T_w - T_{lv}}{\delta} dx \right)$$

  
 $\lambda$ 

$$1 + \frac{2T_w \psi V_l \eta \sigma \delta}{\omega \alpha^{3/2}}$$

---

Beginning with the force balance on the thin-film:

$$P_v - P_l = P_c + P_d \quad (73)$$

Where,

$$P_d = \frac{A}{\delta^3} \quad (74)$$

$$P_c = \sigma \kappa \quad (75)$$

$$P_v = \text{constant} \quad (76)$$

Where the local curvature is defined as:

$$\kappa = \frac{\delta''}{(1 + (\delta')^2)^{3/2}} = \frac{\delta''}{(\alpha)^{3/2}} \quad (77)$$

And local interfacial tension as:

$$\sigma = a + bT_{lv} \quad (78)$$

Now differentiating Equation 73 with the definitions of Equations 74-76 substituted in:

$$\frac{dP_v}{dx} = \frac{dP_l}{dx} + \sigma' \kappa + \sigma \kappa' - \frac{3A}{\delta^4} \delta' \quad (79)$$

Now substituting in Equations 77-78 and their derivatives which are:

$$\sigma' = b \frac{dT_{lv}}{dx} \quad (80)$$

$$\kappa' = \frac{\delta'''}{\alpha^{3/2}} - \frac{3\delta' \delta''}{\alpha^{5/2}} \quad (81)$$

And keeping in mind with a constant vapor pressure, the gradient is zero we have:

$$\frac{dP_l}{dx} = - \left( \sigma' \left( \frac{\delta''}{\alpha^{3/2}} \right) + \sigma \left( \frac{\delta'''}{\alpha^{3/2}} - \frac{3(\delta'')^2 \delta'}{\alpha^{5/2}} \right) - \frac{3A}{\delta^4} \delta' \right) \quad (82)$$

Now, isolating for  $\delta'''$  we have:

$$\delta''' = \frac{\alpha^{3/2}}{\sigma} \left( -\frac{dP_l}{dx} + \frac{3A}{\delta^4} \delta' \right) - \frac{b}{\sigma} \left( \frac{dT_{lv}}{dx} \right) \delta'' + \frac{3(\delta'')^2 \delta'}{\alpha} \quad (83)$$

Equation 83 provides the foundation for the analysis of an evaporating thin-film meniscus. From continuity, momentum, energy and the Kelvin-Clapeyron model further relationships can be developed for the liquid pressure gradient and interfacial temperature

gradient  $\frac{dP_l}{dx}$  and  $\frac{dT_{lv}}{dx}$  respectively.

From the use of Navier-Stokes equations, and applying appropriate simplifying assumptions, a relationship for the liquid pressure gradient can be developed.

Considering assumption two, the flow is restricted to the x-direction. This simplifies the three principal equations of Navier-Stokes to the x-direction momentum equation:

$$\rho \left( \frac{du}{dt} + u \frac{du}{dx} + v \frac{du}{dy} + w \frac{du}{dz} \right) = -\frac{dP_l}{dx} + \mu \left( \frac{d^2u}{dx^2} + \frac{d^2u}{dy^2} + \frac{d^2u}{dz^2} \right) + \rho g_x \quad (84)$$

Considering the geometry of the problem, that is the thin-film height is much less than the length, it is appropriate to apply lubrication approximation [8,35] to Equation 84, allowing the equation to reduce to:

$$\frac{dP_l}{dx} = \mu \frac{d^2u}{dy^2} \quad (85)$$

Now integrating the above equation twice to obtain an equation for velocity profile we have:

$$\frac{1}{\mu} \frac{dP_l}{dx} \left( \frac{y^2}{2} + C_1 y + C_2 \right) = u \quad (86)$$

Using Equation 86 with appropriate boundary conditions, the integration constants can be solved.

These boundary conditions are as follows:

At the solid-liquid interface ( $y=0$ ) slip is permitted. This is represented as:

$$u = u_s = -\beta \frac{du}{dy} \quad (87)$$

At the liquid-vapour interface ( $y=\delta$ ) a shear stress condition is imposed. This shear stress condition equates the interfacial shear stress to the change in surface tension (caused by temperature gradients at the interface) [8]:

$$\tau = \sigma' = \mu \frac{du}{dy} \quad (88)$$

Implementing these boundary conditions, with some manipulation, one can arrive at:

$$u = \frac{1}{\mu} \frac{dP_l}{dx} \left( \frac{y^2}{2} - \delta(y-\beta) \right) + \frac{b}{\mu} \frac{dT_{lv}}{dx} (y-\beta) \quad (89)$$

Considering continuity within the thin-film region provides a means of representing the mass flow rate in terms of liquid pressure gradient and interfacial temperature gradient.

The mass flow rate is represented as:

$$\dot{m} = \rho \bar{A} u \quad (90)$$

Where the cross-sectional area of the thin-film is represented as  $\bar{A} = dzdy$ , where  $dz$  is assumed as unity.

Substituting Equation 89 into Equation 90 and integrating in the  $y$  direction from 0 to  $\delta$  mass flow rate is now represented in terms of liquid pressure gradient and interfacial temperature gradient.

$$\dot{m} = \int_0^{\delta} \rho u dy \quad (91)$$

$$\dot{m} = \int_0^{\delta} \rho \left[ \frac{1}{\mu} \frac{dP_l}{dx} \left( \frac{y^2}{2} - \delta(y - \beta) \right) + \frac{b}{\mu} \frac{dT_{lv}}{dx} (y - \beta) \right] dy \quad (92)$$

∴

$$\dot{m} = \frac{1}{\nu} \frac{dP_l}{dx} \left( -\frac{\delta^3}{3} + \delta^2 \beta \right) + \frac{b}{\nu} \frac{dT_{lv}}{dx} \left( \frac{\delta^2}{2} - \beta \delta \right) \quad (93)$$

The energy equation can now be incorporated into the mathematical model. As heat is applied through the channel wall, it is conducted through the thin-film. As such, the energy equation is represented as:

$$\frac{\partial}{\partial x} \left( k_l \frac{\partial T}{\partial x} \right) + \frac{\partial}{\partial y} \left( k_l \frac{\partial T}{\partial y} \right) + \frac{\partial}{\partial z} \left( k_l \frac{\partial T}{\partial z} \right) + \dot{q} = \rho c_p \frac{\partial T}{\partial t} \quad (94)$$

Considering the thickness of the liquid film is very small, it can be assumed that the conduction heat transfer through the liquid is assumed to be present only in the direction perpendicular to the substrate ( $y$ -direction). In fact, Stephan and Busse [36] calculated normal temperature gradients to be several orders of magnitudes larger than the gradients parallel to the surface. Also considering that the thin-film receives heat from the substrate and does not generate its own heat. Equation 94 thus reduces to:

$$\frac{\partial}{\partial y} \left( k_l \frac{\partial T}{\partial y} \right) = 0 \quad (95)$$

Two boundary conditions are applied when using the energy equation.

The rigid & planar substrate has a specified temperature, thus at  $y = 0$

$$T = T_w \quad (96)$$

At the liquid-vapour interface ( $y = \delta$ ) the conduction heat transfer rate is set equal to the evaporative heat flux.

$$-k_l \frac{\partial T}{\partial y} = \dot{m}_{evap}^* h_{fg} \quad (97)$$

Now applying boundary conditions 96 and 97 and integrating Equation 95:

$$\int \frac{\partial}{\partial y} \left( k_l \frac{\partial T}{\partial y} \right) = 0 \quad (98)$$

$$k_l \frac{\partial T}{\partial y} + C_3 = 0 \quad (99)$$

Thus with manipulation and application of boundary condition 97,

$$k_l \frac{\partial T}{\partial y} = -C_3 = -\dot{m}_{evap}^* h_{fg} \quad (100)$$

Utilizing the integration constant and boundary condition 96 an equation for evaporative mass flux is generated:

$$\dot{m}_{evap}^* = \frac{k_l (T_w - T_{lv})}{\delta h_{fg}} \quad (101)$$

Considering there is a mass flow into the thin-film region (from the bulk region) and there is no mass flow out of the thin-film region (into the adsorbed region) one can create a mass flow balance relating mass flow in to the integral of the evaporative mass flux.

Due to the direction of the fluid flow into the thin-film region and the coordinate system used, the velocity profile is to be taken as negative. For evaporative mass flux, area is taken to be  $dx dz$  with  $dz$  assumed as unity.

$$(-\dot{m}_{in}) - (-\dot{m}_{out}) = \dot{m}_{evap}'' dx \quad (102)$$

$$\dot{m}_{evap}'' = \frac{-\dot{m}_{in} + \dot{m}_{out}}{x_2 - x_1} = -\frac{d\dot{m}}{dx} \quad (103)$$

Now equating Equation 101 and Equation 103, then integrating creates a relation for mass flow in the thin-film as a function of length.

$$-\frac{d\dot{m}}{dx} = \frac{k_l (T_w - T_{lv})}{\delta h_{fg}} \quad (104)$$

$$-\int d\dot{m} = \int_0^x \frac{k_l (T_w - T_{lv})}{\delta h_{fg}} dx \quad (105)$$

And thus yielding

$$\dot{m} = -\int_0^x \frac{k_l (T_w - T_{lv})}{\delta h_{fg}} dx \quad (106)$$

There are the appropriate equations available to now determine a relationship for the liquid pressure gradient in terms of the interfacial temperature gradient.

Equating the equations developed for mass flow rate (Equation 93 and Equation 106) and isolating for liquid pressure gradient as follows:

$$-\int_0^x \frac{k_l (T_w - T_{lv})}{\delta h_{fg}} dx = \frac{1}{v} \frac{dP_l}{dx} \left( -\frac{\delta^3}{3} + \delta^2 \beta \right) + \frac{b}{v} \frac{dT_{lv}}{dx} \left( \frac{\delta^2}{2} - \beta \delta \right) \quad (107)$$

⋮

$$\frac{dP_l}{dx} = -b \frac{C_5}{C_4} \frac{dT_{lv}}{dx} - \frac{v}{C_4} \int_0^x \frac{k_l (T_w - T_{lv})}{\delta h_{fg}} dx \quad (108)$$

In further assembling the mathematical model, a further relationship for interfacial temperature gradient is developed through use of the Kelvin-Clapeyron model.

As mentioned earlier, the Kelvin-Clapeyron model developed by Wayner [6] is used as a means of quantifying the local evaporative mass flux at the liquid-vapour interface associated with the interfacial temperature and pressure jump.

$$\dot{m}_{evap}'' = \frac{1}{h_{fg}} \left( h_{lv}^{cl} (T_{lv} - T_v) - h_{lv}^{kl} (P_d + P_c) \right) \quad (109)$$

Given,

$$h_{lv}^{cl} = \eta \left( \frac{1}{T_{lv}} \right)^{3/2} \left( \frac{M h_{fg}}{T_v} \right) \quad (110)$$

$$h_{lv}^{kl} = \eta \left( \frac{1}{T_{lv}} \right)^{3/2} V_l \quad (111)$$

and

$$\eta = \left( \frac{\left( \frac{2\gamma}{2-\gamma} \right)^2 \bar{M}}{2\pi\bar{R}} \right)^{1/2} \left( \frac{P_v h_{fg}}{\bar{R}} \right) \quad (112)$$

Applying Equations 110-112 into Equation 109, one arrives at:

$$\dot{m}_{evap}'' = \frac{\eta}{h_{fg}} \left( \frac{1}{T_{lv}} \right)^{3/2} \left( \frac{Mh_{fg}}{T_v} (T_{lv} - T_v) - V_l (P_d + P_c) \right) \quad (113)$$

Equating the two relations that describe the evaporative mass flux (Equation 101 and Equation 109), a relation for the interfacial temperature can be developed which has no dependency on liquid pressure.

$$\frac{\eta}{h_{fg}} \left( \frac{1}{T_{lv}} \right)^{3/2} \left( \frac{Mh_{fg}}{T_v} (T_{lv} - T_v) - V_l (P_d + P_c) \right) = \frac{k_l (T_w - T_{lv})}{\delta h_{fg}} \quad (114)$$

:

$$\frac{k_l}{\delta\eta} T_{lv}^{5/2} - \frac{k_l}{\delta\eta} T_w T_{lv}^{3/2} + \frac{Mh_{fg}}{T_v} T_{lv} - V_l b T_{lv} \kappa = Mh_{fg} + V_l \left( \frac{A}{\delta^3} + a\kappa \right) \quad (115)$$

From Equation 115, it is possible to develop a relation for interfacial temperature gradient. This is obtained by differentiating Equation 115 and isolating for  $\frac{dT_{lv}}{dx}$ .

$$\frac{dT_{lv}}{dx} = \left( \frac{2T_v}{\delta^3} \right) \left[ \frac{\delta' \left[ k_l \delta^2 (T_{lv}^{5/2} - T_w T_{lv}^{3/2}) - 3AV_l \eta \right] + V_l \eta \sigma \delta^4 \kappa'}{k_l T_v (5T_{lv}^{3/2} - 3T_w T_{lv}^{1/2}) + 2\delta\eta (Mh_{fg} - V_l T_v b \kappa)} \right] \quad (116)$$

$$\frac{dT_{lv}}{dx} = \left( \frac{2T_v}{\delta^3} \right) \left( \frac{\chi + V_i \eta \sigma \delta^4 \kappa'}{\omega} \right) \quad (117)$$

With representations for both liquid pressure gradient and interfacial temperature gradient, the complete model can be assembled. This is done through substitution of Equation 108 and Equation 117 into Equation 83.

Starting with Equation 108:

$$\delta^m = \frac{3\delta' \delta'^2}{\alpha} + \frac{\alpha^{3/2}}{\sigma} \left( \frac{3A}{\delta^4} \delta' - \frac{\nu k_l}{C_4 h_{fg}} \int_0^x \frac{T_w - T_{lv}}{\delta} dx \right) - \frac{dT_{lv}}{dx} \left( \frac{b}{\sigma} \right) \left( \frac{C_5}{C_4} \alpha^{3/2} + \delta^m \right) \quad (118)$$

$$\delta^m = \frac{3\delta' \delta'^2}{\alpha} + \theta - \psi \frac{dT_{lv}}{dx} \quad (119)$$

And now substituting Equation 117:

$$\delta^m = \frac{3\delta' \delta'^2}{\alpha} + \theta - \psi \left( \frac{2T_v}{\delta^3} \right) \left( \frac{\chi + V_i \eta \sigma \delta^4 \kappa'}{\omega} \right) \quad (120)$$

Now substituting in Equation 77:

$$\delta^m \left( 1 + \frac{2T_v \psi V_i \eta \sigma \delta}{\omega \alpha^{3/2}} \right) = \frac{3\delta' \delta'^2}{\alpha} \left( 1 + \frac{2T_v \psi V_i \eta \sigma \delta}{\omega \alpha^{3/2}} \right) + \theta - \left( \frac{2T_v \psi \chi}{\omega \delta^3} \right) \quad (121)$$

And finally we have:

$$\delta^m = \frac{3\delta' \delta'^2}{\alpha} - \frac{2T_v \psi \chi}{\omega \delta^3 \lambda} + \frac{\theta}{\lambda} \quad (122)$$

As above, in the interest of representing this equation in a reasonable manner, placeholder variables  $\chi$ ,  $\omega$ ,  $\psi$ ,  $\lambda$  and  $\theta$  are used which are collections of terms from the ODE, which are identified in Table 8 on the first page of this appendix.

## Appendix B – Adsorbed Film Thickness

Beginning with the Kelvin-Clapeyron model:

$$\dot{m}_{evap}'' = \frac{1}{h_{fg}} \left( h_{lv}^{cl} (T_{lv} - T_v) - h_{lv}^{kl} (P_d + P_c) \right) \quad (123)$$

Neglecting conductive losses in the thin-film region based on the size scale, and thus equating  $T_{lv} = T_w$ . In addition, taking the adsorbed layer as constant thickness, thus inferring zero curvature, the capillary pressure within this region to be zero. Furthermore, within the adsorbed region due to the strong presence of van der Waals forces, evaporative mass flux is zero.

$$\dot{m}_{evap}'' = 0 = \frac{1}{h_{fg}} \left( h_{lv}^{cl} (T_w - T_v) - h_{lv}^{kl} (P_d + \cancel{P_c}) \right) \quad (124)$$

Substituting in values for the Clapeyron and Kelvin coefficients and isolating for adsorbed film thickness:

$$0 = \frac{\eta}{h_{fg}} \left( \frac{1}{T_{lv}} \right)^{3/2} \left( \frac{Mh_{fg}}{T_v} (T_w - T_v) - V_l P_d \right)$$

$$V_l P_d = \frac{Mh_{fg}}{T_v} (T_w - T_v)$$

$$\frac{A}{\delta^3} = \frac{Mh_{fg}}{V_l T_v} (T_w - T_v)$$

$$\delta = \left[ \frac{AV_l}{Mh_{fg}} \left( \frac{T_v}{T_w - T_v} \right) \right]^{1/3} \quad (125)$$

## Appendix C – Bond Number Calculation

The bond number is presented here for the highest and lowest case found in this literature. It is found that in both cases it is sufficiently small. This suggests that surface forces far outweigh the effect of the gravitational forces.

In general Bond Number is defined as:

$$Bo = \frac{\rho_l g_x \left(\frac{H}{2}\right)^2}{\sigma} \quad (126)$$

For the case of pentane at 300 K and a channel height of 20  $\mu\text{m}$  we have:

$$Bo = \frac{\left(619.6 \frac{\text{kg}}{\text{m}^3}\right) \left(9.81 \frac{\text{m}}{\text{s}^2}\right) (10 \mu\text{m})^2}{0.08141 \frac{\text{N}}{\text{m}}}$$

$$Bo = 7.5 \times 10^{-6}$$

For the case of pentane with a larger channel height of 1 mm we have:

$$Bo = \frac{\left(619.6 \frac{\text{kg}}{\text{m}^3}\right) \left(9.81 \frac{\text{m}}{\text{s}^2}\right) (0.5 \text{mm})^2}{0.08141 \frac{\text{N}}{\text{m}}}$$

$$Bo = 1.9 \times 10^{-2}$$